The Radio Science Bulletin

ISSN 1024-4530

INTERNATIONAL
UNION OF
RADIO SCIENCE

UNION
RADIO-SCIENTIFIQUE
INTERNATIONALE

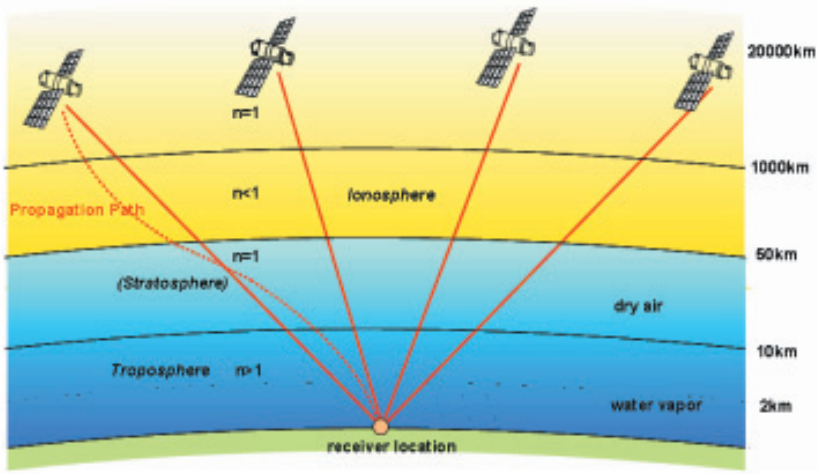

No 329
June 2009

URSI, c/o Ghent University (INTEC)
St.-Pietersnieuwstraat 41, B-9000 Gent (Belgium)

Contents

Front cover: The structure of the atmosphere and its influence on the propagation path. See paper by A. Hornbostel pp. 21-30.

For information, please contact :
The URSI Secretariat
c/o Ghent University (INTEC)
Sint-Pietersnieuwstraat 41, B-9000 Gent, Belgium
Tel.: (32) 9-264 33 20, Fax: (32) 9-264 42 88
E-mail: info@ursi.org
http://www.ursi.org

Editorial

I am extremely pleased to announce that Paul S. Cannon has been named the new Editor of the journal *Radio Science*. Paul will take over from Tarek Habashy, who has done an outstanding job as Editor. Congratulations to Paul, and a very large thank you to Tarek! *Radio Science* is published by the American Geophysical Union. It carries the URSI logo, and has long had a close association with URSI.

In this issue you will find a call for papers for a special issue of the *Radio Science Bulletin* on "High-Altitude Platforms." Please read it, and contribute if you can.

The *Bulletin* welcomes ideas for special issues. Please send me any suggestions.

Our Papers

It was 81 years ago that reports were first made of strange echoes in radio soundings of the ionosphere. These were later identified as returns from the ionization associated with the passage of meteors through the ionosphere. Jack Baggaley provides a very interesting review of the history and current status of the interpretation of such echoes. He begins with a brief overview of the observation of such echoes, the difficulties of their interpretation, and the importance they have played as an observation tool. He then provides a very detailed and most fascinating chronology of the early observations of and experiments with meteor-tail echoes from the 1920s to 1940. As he points out, many of the early attempts at interpretation were little more than speculation. Significant progress was made during the years surrounding the second World War. The author explains how the radars and related equipment developed for military use enabled substantial improvements in the observations and experiments. He traces the development of experimental work on meteor-trail echoes through 1952, and then explains the development of the theory of meteor scattering. This includes a discussion of the scattering cross section and how it behaves in limiting cases; reflection from an instantaneously formed plasma column, and the effects of time variations; under- and over-dense echoes; reflection from the plasma as it develops; and the effects of viewing geometry. All of this leads to an understanding of the parameters that can be measured using radar returns from meteor tails. This paper is of interest both because of its historical detail, and because of its scientific content.

The efforts of Michael Rietveld and Phil Wilkinson in bringing us this *Review of Radio Science* are gratefully acknowledged.

The use of satellites to determine precise position on the Earth's surface has become ubiquitous, critical for many everyday functions, and such that it is almost taken for granted. Satellite navigation systems depend on comparisons of measurements at the receiver of the times of arrival of signals from multiple satellites. Propagation issues play a key – and, in many cases, the dominant – role in determining the accuracy of such measurements, and thus the accuracy of the position obtained. A. Hornbostel provides an insightful look at propagation problems in such measurements, and the methods used to mitigate them. The paper begins with a description and analysis of the propagation path through the atmosphere. The various components contributing to ionospheric propagation issues are then examined, including total electron content, and regional and temporal variations. The use of two frequencies to correct for ionospheric variations is analyzed. Many low-cost commercial systems using satellite navigation use only single-frequency receivers, and methods of correction for such systems are described. Advanced satellite navigation systems, such as the American Wide-Area Augmentation System (WAAS) and the European Global-Navigation Overlay System (EGNOS), are briefly discussed. The paper then considers errors introduced due to tropospheric propagation. This includes the effects of refractivity and delay, and their regional and temporal variations. A comparison is provided for various correction models. It is also shown that local events, such as severe weather, can have significant effects. The paper concludes with discussions of the effects of ionospheric scintillations, shadowing, and multipath. This paper provides a very comprehensive and quite readable review of the factors affecting the accuracy of systems using satellite navigation. Given the degree to which such systems have affected everyday life, I think you'll find this paper fascinating even if you don't deal with the design or precision use of such systems.

The efforts of Madhu Chandra and Phil Wilkinson in bringing us this *Review of Radio Science* are gratefully acknowledged.

With the direct support of the URSI Board, Gert Brussaard conceived and organized a Forum on Radio Science and Telecommunications at the XXIX URSI General Assembly in Chicago. One of the invited papers from that

forum, by Andreas Molisch, is included in this issue. It provides an overview of ultra-wideband (UWB) communications, a topic on which a tremendous amount of research and development work is currently being done. The paper begins with a discussion of what constitutes a UWB system, and a thoughtful look at the potential advantages associated with such systems. The various frequency regulations and interference aspects that play such a significant role in shaping UWB communications around the world are then reviewed. The propagation channels for UWB communications are analyzed in detail. The differences between the channels used by common narrowband communications and by UWB communications are explained, along with why these differences are significant. Two situations are considered: systems with large relative bandwidth, and systems with large absolute bandwidth. The fundamental form of the impulse response is considered, along with issues related to the frequency dependence of path loss, the arrival of multipath components in clusters, and small-scale fading statistics. The two available standardized channel models are discussed. This is followed by an analysis of various methods of allowing multiple users to simultaneously access UWB systems. Methods described include impulse radio, direct-sequence CMDA, OFDM, frequency hopping, and receiver design for several of these methods. Several applications and associated standards for UWB communications are then summarized. This paper is an excellent introduction to and an overview of a very important topic.

The efforts of Gert Brussaard and Phil Wilkinson in bringing us this paper are gratefully acknowledged.

Our Other Contributions

In his "Radio-Frequency Radiation Safety and Health" column, Jim Lin describes and discusses four recent studies on the development of cancer in normal mice exposed to various types of cell-phone radiation. The results are quite interesting, as are the similarities and differences in the way the experiments were conducted.

Peter Watson has another doctoral abstract to share in his column. I know that there are many doctoral dissertations in radio science for which Peter is not receiving abstracts. If you or one of your students has recently completed a dissertation in our field, please send the abstract to Peter. This is an excellent opportunity for the community to learn of the work, and for the student to become better known in the community.

We also have announcements of two books by URSI radio scientists in this issue.

Welcome to Kristian Schlegel!

It is with great pleasure that I announce that Kristian Schlegel, former President of URSI, is joining the Editorial Board of the *Radio Science Bulletin* as Associate Editor for Book Reviews. He will be actively soliciting reviews of books in the field of radio science for the *Bulletin*. If you have recently authored or edited a book in our field, please contact Kristian (e-mail: schlegel@linmpi.mpg.de) regarding getting the book reviewed. If you are aware of a book that should be reviewed, or if you are interested in writing a review of a book, please let him know. With the advent of this column, we hope to be able to replace simple announcements of books in our field with valuable reviews of them.

Message from the Secretary General

It is with deep regret that Prof. Gert Brussaard offered his resignation as URSI President at the annual Board meeting in April since he felt that due to health problems he was no longer able to fulfill his duties as President the way he had hoped to do. He proposed to the Board that Prof. François Lefeuvre, current Past-President, should replace him as President for the remainder of the triennium. The Board unanimously accepted this proposal, thanking Prof. Gert Brussaard for his dedication to URSI and asked him to remain on the Board as Past President.

In line with the URSI Statutes, all member Committees have been informed and consulted about this proposal and support this change in responsibilities which ensures a continuous operation within the Board of Officers.

Call For Papers

RADIO SCIENCE BULLETIN

Special Issue on High-Altitude Platforms

Submission deadline: August 31, 2009

The *Radio Science Bulletin* is soliciting papers for a special issue on "High-Altitude Platforms," tentatively scheduled for publication in December 2009 (depending on the number of papers accepted for publication, two issues may be involved).

High-altitude platforms (HAPs) are stratospheric quasi-stationary platforms that will operate at altitudes of from 17 to 24 km for significant periods of time. HAPs will be useful new complements – and in several cases, even alternatives to – actual geostationary (GEO) and low-Earth-orbit (LEO) satellites systems. The most important applications of HAPs are for military and commercial radio communication; remote sensing; intelligence, surveillance, reconnaissance (ISR); differential GPS, and other wireless applications. HAPs may also be advantageous alternatives for numerous high-quality and broadband terrestrial radio systems.

HAP activities concern numerous experts, and especially URSI members of Commissions B, C, E, F, H, J, and K. The scope of this special issue is to provide an overview of ongoing HAPs research and development activities worldwide, and to examine future perspectives.

The major topics related to HAPs are as follows:

- Concepts and thorough comparisons with GEO, LEO, and terrestrial radio systems*
- Frequency standards, regulation, and management
- Antenna design
- Radio propagation issues and link budgets
- Coexistence and EMC issues
- Modulation, multiplexing, and coding techniques
- Networks, diversity, and cluster operations
- Home security and military issues status and forecasting
- Status of commercial issues and forecasting, especially for mobile communication
- Communication and control for remote sensing and wireless sensor networks
- Laser concepts and applications in comparison with microwave systems
- Microwave energy transmission to platforms using rectennas
- Status of energy sources and forecasting, including terrestrial microwave power
- Platform meteorology, positioning, thermal control, and safety
- Status of UAV, manned, and balloon airships and forecasting

(*The first topic will be presented as an introduction prior to the *RSB* special issue.)

Potential authors are invited to submit draft papers in PDF format to one of the Guest Editors below. The submission deadline is **August 31, 2009**. Acceptance notification is planned by October 30, 2009. The final manuscript is due by November 30, 2009.

Guest Editors for the HAPs special issue:

Dr. David Grace (e-mail: dg@ohm.york.ac.uk) is from the University of York, UK, which is leading the European COST 297 HAPCOS research and technological discussion forum on HAPs. He is working group chair for WG1: Radio Communications, and the former technical lead of the EU FP7 project CAMPANINA.

Prof. Ryszard Struzak (e-mail: r.struzak@ieee.org), of the National Institute of Telecommunications (PL) and Wroclaw University of Technology, is former Vice Chair of URSI Commission E, co-Chair of its Working Group on Spectrum Management/Utilization and Wireless Telecommunications, and Head of the CCIR department dealing with the frequency-spectrum management, radio propagation, and science applications Study Groups.

Prof. Jacob Gavan (e-mail: jacobg@sce.ac.il) is co-Chair of URSI Working Group E8 on Electromagnetic Compatibility in Wired and Wireless Communication Systems, and a Distinguished Lecturer of the IEEE Communications Society. He was the former Dean of the Faculty of Engineering of Holon Institute of Technology. He is now a consultant and Head of the Communication Engineering Section at the Sami Shamoon College of Engineering in Beer-Sheva, Israel.

Meteoric Ionization : The Interpretation of Radar Trail Echoes

J. Baggaley

Abstract

An overview is presented of the developments during the key stages in the recognition of the mechanisms governing the behavior of meteoric ionization and an understanding of the radio-reflection processes. Meteors were the source that provided the enigmatic echoes: the fleeting radio returns seen in early ionospheric soundings, or as interference on communication links. The paper covers the key observations, probing techniques, and theoretical developments that enabled progress to be achieved in our understanding of the scattering processes from meteoric plasma, for the case of a reflection geometry giving rise to trail echoes. The development of meteor-echo theory enabled the realization of the value of radar meteors as valuable atmospheric and astronomical probes.

1. Introduction

The year 2008 marked the 80th anniversary of the first radio reports of strange fleeting echoes, which later became understood as plasma produced by the ablation of meteoroids. An originally enigmatic radio phenomenon, viewed on occasions as an interfering signal, became a valuable probing tool for the atmosphere. It enabled measurements of temperatures, scale heights, and wind-field, especially on micro-scales in a region difficult to access by other techniques. Radar meteors also became a tool for astronomy to gain a whole new perspective of monitoring Earth-impacting bodies. They advanced our understanding of the solar-system dust cloud. Radio techniques enabled us to measure the speed of meteoroids through the atmosphere and, using multiple sites, to determine their trajectories and orbits in space. For such programs, a foundation of the meteoric environment is required: the behavior of the created plasma, and a formulation of the mechanism of radiowave reflection. In the present work, the focus is on the class of meteor reflections now known as meteor-trail echoes, as distinct from the head echoes. Attempts to formulate radio scattering from the plasma produced by an ablating meteoroid could not be attempted until several controlling factors were known, such as a realistic appreciation of the geometry of and physical conditions in the created plasma. Experimentally, this was complicated in the 1930s by the confusion of what is now termed sporadic-E (E_s), with discrete reflections from the individual ionization trails of meteors in the height regime of 90-110 km. It is now recognized that an important agent in creating E_s is indeed the ionization deposited by meteors that is redistributed via charge exchange, and by the effects of wind-shear and geomagnetic field forces.

There were interpretation difficulties, because some early ionospheric-probing techniques employed swept-frequency modulation of CW or square pulses, with phase comparisons provided by reception from a distant transmitter and by measuring the interference between the direct ground signal and that reflected from the ionosphere. The frequency gradient provided the phase path and virtual sky-signal path. The technique made discrete targets difficult to identify, with multiple targets a problem in this method, resulting in interpretation difficulties in terms of identification of specific scattering entities. Reports described periods when a reflecting layer suddenly changed its virtual height, as seen on a (assumed) vertical sounding system (e.g., 1-6 MHz). Compared to early ionospheric studies, the very short durations of meteor returns were of quite a different time scale, making their recognition and study difficult.

In the early literature, the terms used for non-standard echoes from near 100 km included "abnormal E" and "intense E." Early soundings showed that sampling simultaneously from stations separated by ~100 km yielded largely unrelated echo structure. The horizontal and vertical structure of E_s clouds was only slowly understood.

By their very nature, meteors were detected as largely a byproduct of either propagation studies for early radio links, or by vertical radio probing of the ionosphere.

Jack Baggaley is with the Department of Physics and Astronomy, University of Canterbury, Private Bag 4800, Christchurch, New Zealand; Tel: +64 3 364-2558; e-mail: jack.baggaley@canterbury.ac.nz.

This is one of the invited *Reviews of Radio Science* from Commission G.

The advance of the ideas of meteor ionization and experimental methods provided an interesting development. In Section 2, it is useful to follow chronologically the events, noting some of the experimental arrangements.

2. The Period from 1920s to 1940: Observations and Speculations

In 1928, Heising [1], probing the *E* region with frequencies from 2.7 to 5.2 MHz, found sudden increases in nighttime ionization levels in place of the normal decrease that was known to occur after sunset. He included a rather picturesque description: "It would appear as though great masses of electrons are tossed into the atmosphere rather quickly...." He proposed a solar source of impacting electrons during the night as responsible. In 1929, Eckersley [2] studied propagation conditions monitoring arrival directions from stations transmitting in the range of 6 to 20 MHz, where penetration of the *E* region occurred, allowing reflection from the *F* layer. "Anomalous scattering into the skip zone" caused by ionized clouds below the normal *E* layer was noted. In 1930, Appleton [3] noted the variability of virtual height measured at 0.75 MHz, and remarked

> On such occasions, it seems as if there were some agency or agencies which either maintained the process of ionization....It appears as if on these occasions...there is some ionising agent present which can influence the dark side of the Earth.

In 1931, Skellett [4] made estimates of the ionization densities produced from individual meteoroid ablation, though with much over estimation because of the use of an unrealistic fraction of the meteoroid kinetic energy that is channeled into ionization, and also the exaggerated lateral extent of the plasma. Pickard [5] reported on studies of propagation conditions, carrying out several years of commercial forward scatter, which included correlations of increased nighttime signal strength with known meteor-shower activity.

In 1932, Appleton and Naismith [6] noted abnormal nighttime effects. Such studies took advantage of the spectacular meteor displays that deposit energy into the ionosphere. In the same year, Schafer and Goodall [7, 8] used pulse sounding, employing four spot frequencies between 1.6 and 6.4 MHz during known showers, especially the Leonids shower of 1931. They noted short-term nighttime signal changes. They suggested as candidates for such a source of ionization meteors producing what became termed "blanketing E_S" (although simultaneous magnetic activity related to a possible aurora complicated interpretation). Skellett [9], in pointing out that the inferred heights of radio features were similar to the heights of visible meteors, presented estimates of energetics to provide deposited ionization (the ionization probability used was too high by orders of magnitude, and the plasma train too large). The effect of the bulk influx of many meteors was also considered.

In 1933, Appleton and Naismith [10], operating a system in ionosonde mode and monitoring diurnally in a long series, "...recorded on a number of nights the ionisation in the lower region actually may increase....there is some agency which produces nocturnal ionization beyond the ordinary amount...." In 1934, Ratcliffe and White [11], using night-time probing on frequencies of 2 MHz and 4 MHz, noted "...nocturnal *E*-region...have a likely source of thunderstorms and magnetic activity...." Mitra et al. [12] used a swept-frequency technique to determine the

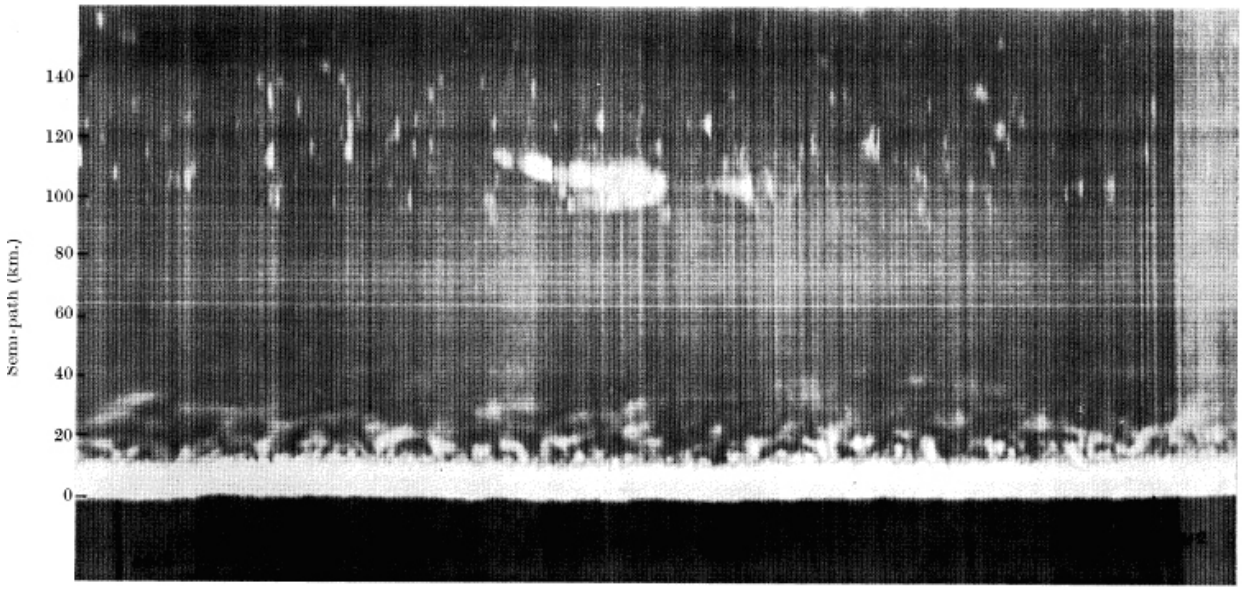

Figure 1. An echo-range time record at 6 MHz over a period of one hour [15]. The ordinate is range from 10 to 140 km. The 10 minute duration echo near the middle of the image is probably an E_s layer near the zenith. The other echoes from 100 to 140 km are meteors ([15] used with permission of the Royal Society of London).

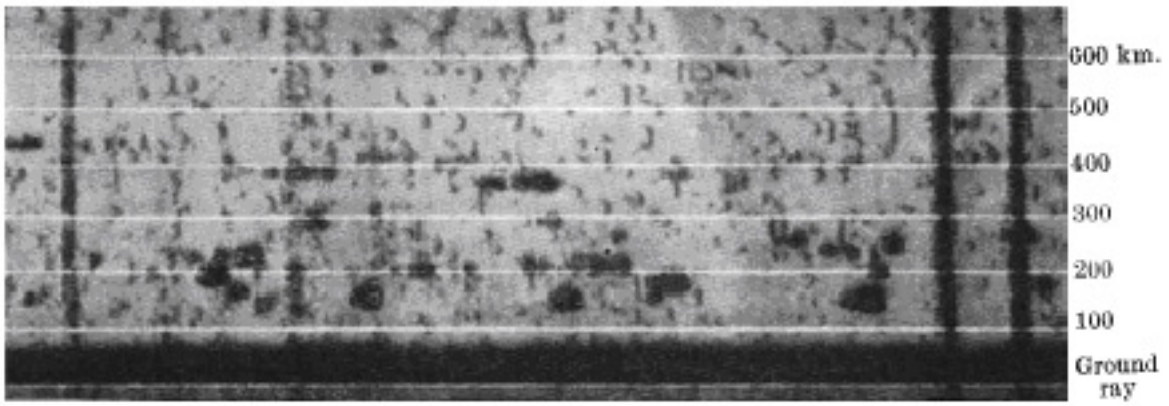

Figure 2. An echo-range time record for a period of 40 s [17]. The ordinate range is from 0 to 600 km. All echoes are probably meteors, those with ranges out to ~380 km are at large zenith angles (reprinted by permission from Macmillan Publishers Ltd: Nature, [17], copyright 1937).

penetration frequency of the *E* layer, and measured high ionization densities coincident with the 1933 Leonids shower influx.

In 1935, Skellett [13] modeled likely meteor effects on the atmosphere, noting the self-luminous energy storage associated with enduring visible trains. He monitored transatlantic radiotelephone service over three years at shower times, measuring effects on propagation-fading disruption, with disruptions lasting seconds. He reported that effects were marked during the Leonid 1931 apparition. A separate 2.398 MHz sounding experiment was directed specifically for the Eta Aquarid shower period in July 1931, and also the Leonids in November 1931, using 2.398, 7.6, and 8.5 MHz sounding. Increases in ionization were attributed to individual overhead bright meteors, there being few such events during non-shower days. Attempts were made to estimate ionization densities and the effective electron-ion recombination coefficient.

In 1937, Appleton et al. [14], sampling at 6 MHz, noted "...*E*-layer bursts causes of abnormal *E* ionization ....we have also observed a peculiar type of reflexion at a height of 100 km which only lasts a few seconds....nocturnal abnormal *E* region reflexions is caused by the entry of ionizing particles into the atmosphere either in the form of bursts or in the form of a steady stream…charged solar particles or meteorites...."

The first time-sequence records seem to be those of Watson Watt et al. in 1937 [15], who, reporting vertical sounding at 6 MHz, presented filmstrip range-time displays clearly depicting meteor echoes lasting a few seconds (Figure 1 shows a one-hour record: their Figure 10). They stated that "...bursts of ionization at 105 km giving densities sufficient to return television waves at vertical incidence...persist for a fraction of a second."

Operating a swept-frequency 1-15 MHz sounder, in 1937 Bhar [16] reported on measuring the critical penetration frequency of the *E* region during the 1936 Leonid meteor shower. A close association was found, but no effect on the *F* region.

Also in 1937, Eckersley [17], monitoring a commercial station with a 9.127 MHz 40 kW 200 ms pulse with a 50 Hz pulse-repetition frequency (PRF), situated 19 km away from the receiver, used spaced-frame antennas and phase comparisons to deduce echo directions. This allowed the measurement of ground distance as well as virtual height. The author noted discrete "ionic clouds" present day and night, strongly suggesting meteors. A film range-time display of a 40-second time period is reproduced in Figure 2. In 1938, Skellett [18] supported the suggestion by Eckersly of a meteor origin, commenting on "...short-lived isolated clouds in which momentarily the ionization reaches a value much higher than normal."

In a 1938 scattering study, Pierce [19] monitored the signal strength from a 9.57 MHz 30 km-ground-distance station, noting signal bursts. Pierce appears to have been the first to be specific about the cylindrical geometry of the plasma (though he considered that critical reflection conditions operated, and that the plasma diameter was large compared with the probing wavelength, with the ionization density decreasing as the train expanded (under diffusion, although that mechanism was not stated). Scattering from such a "...long cylinder of ionization...under these conditions it is seen that no energy will be reflected to its source unless a perpendicular may be passed from the source to the path of the meteor." Interestingly, the author pleaded for simultaneous observations of visual meteors and the arrival angle of signal bursts.

In 1938, Appleton and Piddington [20] used a 8.8 MHz 3 kW 30 ms pulsed transmitter (Tx), radiating via a half-wave dipole $\lambda/4$ above ground, giving a broad vertical beam. They deduced the effective reflection coefficients on the basis of small ionization clouds and the virtual heights of transient echoes day and night, near 100 km. They noted, "There can be little doubt that these observations indicate the temporary existence of marked scattering centres in the

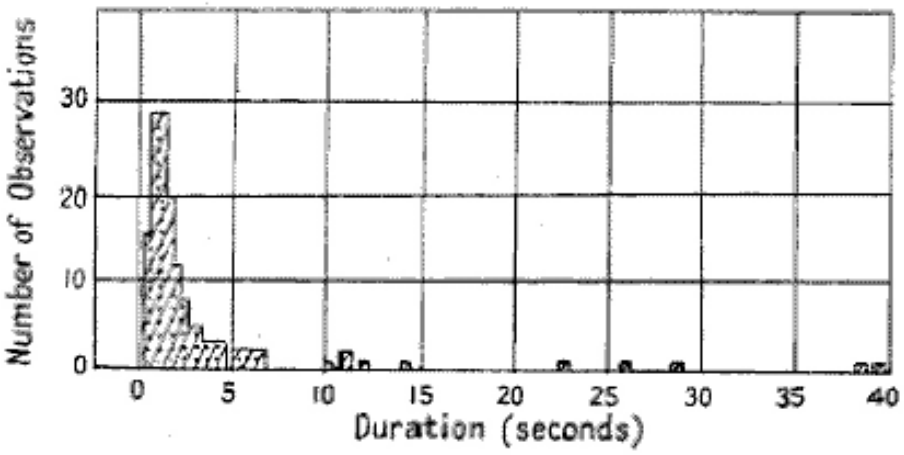

Figure 3. The duration distribution of meteor echoes at a frequency of 7.59 MHz [22].

ionosphere which form and disappear throughout the whole of the twenty four hours...due to some cosmic agency." Later, in 1939, Appleton et al. [21] described "intense-*E* being clouds of more intense ionization immersed in a simple region." They further stated that they "...noted a transient type of reflection lasting only a few seconds and caused by scattering from temporary ionic cloudlets, which is found by day and night round the 100 km level." They commented on the difficulties of recording such "fleeting echoes."

Concerned with effects on propagation, in 1940 Eckersley [22] studied scattering that occurred away from off-great-circle propagation paths using a 19.5 MHz transmitter with direction-finding antennas at a receiver (Rx) of 19 km separation. Recognizing the common occurrence of scattering processes, the author provided definitive short-term scattering characteristics of E_s and ion clouds (meteors). The first measurement of the duration distribution was provided with experimental evidence for many short durations (Figure 3, from Figure 11 of their paper), the form being instructive in providing clues about the reflection mechanisms.

The prevailing view expressed in work of the period speaks of "ionic clouds," "scatter clouds" – depicting a spherical assembly of electrons – consistent with the discrete echo of limited range spread that was commensurate with that expected from the radar pulse length. It is interesting that the idea of a column of ionization – analogous to the visible excitation trail of a meteor – only came later. It was not appreciated that a narrow column of electrons of length similar to visible trails would in fact produce an echo of discrete range (see Section 4.3). In addition, the geometry of the reflection process results in reduced sensitivity to meteors near the zenith, so that vertical probing was in fact the most disadvantageous antenna-pointing direction (see Section 4.3).

In 1941, Blackett and Lovell [23] examined the possible production of an ionization column resulting from proton impact produced by primary cosmic rays. The origin of the "scatter echoes" was confirmed later as not being from cosmic rays. However, the geometry and radar scattering mechanism was established by this paper: "A cosmic ray shower of high energy produces a long narrow cylinder of ionization traversing the whole atmosphere." They established the essential geometry of the reflection process: the shape of the target means they employed a scattering length of one Fresnel zone (see Section 4.3). It is of interest to note that the paper was composed (August 1940) at a radar station that was often under attack from aircraft [24].

The association of visual meteors with reflections at 3 MHz and 6.4 MHz was studied by Pierce in 1941 [25], to confirm the governing geometry: "...energy of impact sufficient to ionize any particle with which it comes in contact. Thus a line of ionized atoms or molecules is established along which the density of free electrons is very great. The charged particles immediately begin to diffuse radially...." The author made an estimate of the electron density from the echo duration. However, an incorrect reflection coefficient was employed: an extended ionization column was recognized, but the column diameter was incorrectly assessed as being much greater than the operating wavelength (implying diameters >100 m).

3. The Period 1940 to ~1952: Interpretations

The period of 1939-45 provided an impetus for three reasons:

1. Equipment: a large number of radar tracking stations employing high pulse power with narrow-beam steerable antennas directed to low elevation (rather than sampling towards the zenith), to provide aircraft detection and tracking, became available;

2. Personnel with defense experience and subsequent availability of equipment (and in some cases military personnel to assist). Similar equipment served to advance the early work in radio astronomy.

3. The parallel development of theoretical work to understand the types of observed echoes.

3.1 Radar Equipment and Techniques

Many of the radars that were produced during WWII formed an interesting subject in themselves. Some were ideal for the task of providing foundation observations for theoretical formulations of reflection coefficients, echo behavior, and tools for both atmospheric and astronomical studies. Especially suitable for the purpose were the mobile gun-laying (GL) radars, developed in the UK circa 1940, operating at 72 MHz and attached to antiaircraft units. The GL2 unit was capable of a power output of 150 kW of 3 ms pulses at 1 to 2.2 kHz pulse-repetition frequency with a 25 kV dc supply. This was achieved from a pair of cathode-driven VT98 triode (also labeled type CV1098) power tubes using forced-air cooling. The tube (Figure 4) was developed from the previous VT58 in order to secure greater emission under pulse conditions by incorporating filaments using thoriated tungsten. The GL2 employed a system of dipole antennas at differing heights and horizontal separations for elevation and azimuth fixing. With minor modifications, this equipment proved ideally suited as a meteor-research tool. Other systems, such as the Chain Home (CH) system, used a frequency (20-30 MHz) that was actually more sensitive for meteors (see Section 4.4).

Figure 4. The transmitting tube, type VT98.

They used water-cooled transmitter tubes, required large metal antenna supporting masts in operational service, and required a team of personnel to operate.

There were associated advances in techniques that enabled efficient operations and that proved valuable for meteor use. These included the provision of a common antenna for both transmitting and receiving (the transmitting/receiving switch employed $\lambda/4$ stubs and spark gaps), and the development of polythene as improved insulating material for coaxial cables used in transmission lines and impedance-matching sections. The introduction of the Chain Home Low (CHL), Ground Controlled Interception (GCI), and similar radars operating at 200 MHz and the later magnetron-powered radars at 10 cm (for improved image resolution), were not as useful. Meteor scattering is a long-wavelength phenomenon (see Section 4.4): during the 1960s, the author built and operated a radar system for meteor research operating at 17 MHz, which was constructed in part of surplus military components.

Many GL2 units were produced and some rendered meteor service around the world. One unit was used up to 1975 by the author at the University of Canterbury's station near Christchurch in New Zealand. The author also visited a unit used at the Englehart Observatory near Kazan, which operated until about 1985. It was the eventual lack of a supply of VT98 tubes that caused the end of the GL2's use for these two radar-meteor programs.

3.2 Experimental Work

During the operation of defense radars in the UK, echoes were commonly observed on Chain Home and gun-laying units (termed "scatter clouds" or "short duration

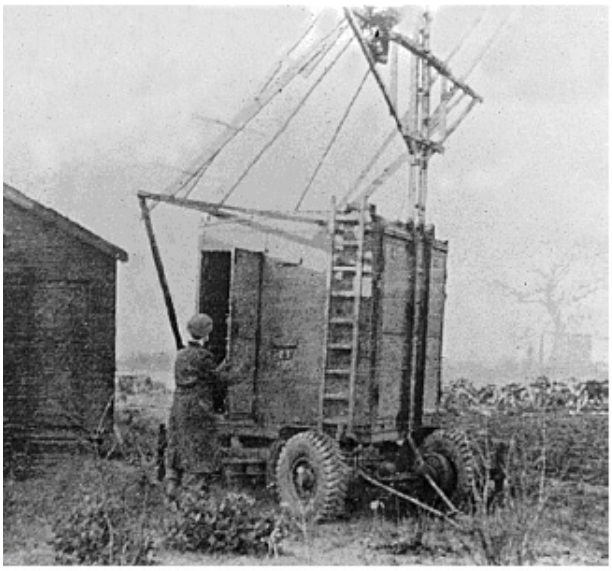

Figure 5. The first mobile ex-army GL2 radar used from 1945 for meteor studies at Jodrell Bank, near Manchester, UK (photo provided by the University of Manchester).

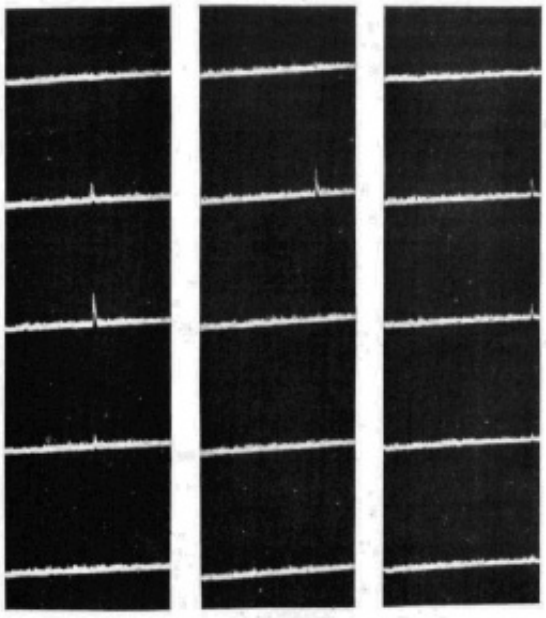

Figure 6. A sequence of echoes recorded on film at 16 frames per second. The range interval shown is 80 to 125 km ([30], IOP Publishing Ltd., used with permission).

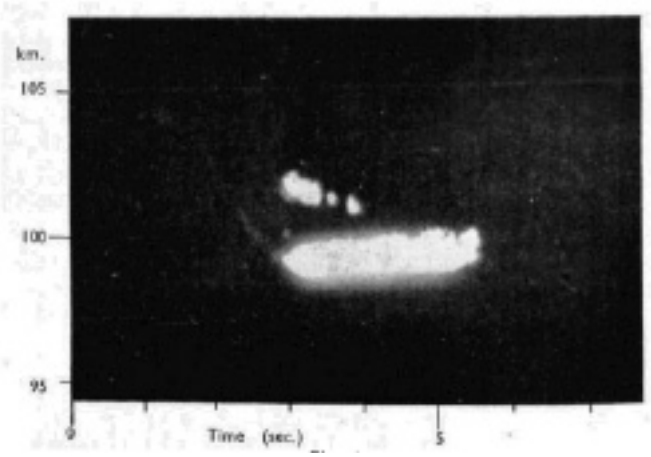

Figure 7. A range-time radar 55 MHz 8 s sequence [30]. The echo at range 102 km was composed of several features (probably) caused by atmospheric turbulence. The echo at range 100 km had a body (transverse geometry) echo, showing a drift in range caused by a radial wind and a faint head echo lasting 0.5 s with a hyperbolic range-time characteristic, from which the meteor speed can be derived. That speed would be a lower limit, since the aspect angle between the trajectory and the radar beam line of sight was not known ([30], IOP Publishing Ltd., used with permission).

scatter echoes") at frequencies well above the critical frequencies for either normal or abnormal (E_s) layers, where such echoes often interfered with aircraft detection and tracking. The availability of mobile radar units and photographic recording led to an intense period of observational work during 1945-48. This led to rapid progress where the need was recognized to modify the antenna-elevation response for optimum meteor detection. For example, the work at Jodrell Bank, near Manchester UK, starting in late 1945 employed a modified GL2 system (Figure 5), with the later addition of an army searchlight mounting for an array of fully steerable Yagi antennas, enabling full-sky surveillance.

In 1945, Eckersley and Farmer [26], using a frequency of 7.6 MHz, measured the direction of arrival and polarization state of echoes near 100 km for both E_s and individual meteors. They noted rapid polarization changes. They considered that such echoes were incompatible with a meteor source, because their phase behavior suggested rapid changes in arrival direction due to suggested multiple paths (but see Section 4.4 for theoretical phase behavior). It was noted that meteors reflected at frequencies well in excess of the critical frequency of the *F* region: 45 MHz TV (Appleton [27]) and at 105 MHz (Ferrell [28], using a US military SCR270B radar unit).

In 1946, Hey and Stewart [29] carried out a surveillance from October 1944. They recognized that "columns of ionized gas....present their echoing areas when viewed at right angles to their length." Operating ex-military 150 kW radars from 42 to 75 MHz, equipped with Yagis, they recorded the Lyrids meteor shower (April 20, 21, 22, 1946), while maintaining a visual watch for overhead meteors. They so confirmed the association of echo activity with showers. In addition, recognizing the importance of the reflection geometry, they were able to deduce the radiants (upstream meteoroid direction) of a stream (not for individual meteors: the technique requires several members) by employing the different radar-system responses governed by the meteor-reflection orthogonal geometry due to different antenna-pointing directions. They thus for the first time identified daytime meteor streams.

Extending their earlier work, in 1947 Hey and Stewart [30] presented a time sequence (cine film, 16 frames per second) aimed at quantifying the rapid decay times of echoes (Figure 6). From this, they made the significant finding that many echoes (at 73 MHz) had decay times of the order of 0.06 s. Using multiple radar stations, they measured echo-height distributions. With the important recognition of the controlling geometry, they deduced radiant coordinates for the Delta Aquarid meteor shower of July 29, 1946, and the Giacobinids (that spectacular event providing a focus of many observational projects and impetus to our understanding) on October 10, 1946. They also reported much reduced echo rates, using sampling at the higher frequency of 212 MHz. In a key observation, they were the first to report the head echo shown in Figure 7. This is the reflection from the plasma surrounding the meteoroid itself – weak compared with the broadside echo – with the range-time hyperbola function providing an estimate of the meteoroid's linear speed in the atmosphere. In 1947, Prentice et al. [31] mapped the Giacobinids and other streams. By orienting the directive Yagi array in a different direction with respect to the shower radiant, they were able to confirm the scattering geometry in a dramatic way during the Giacobinids display. The optimum reflection

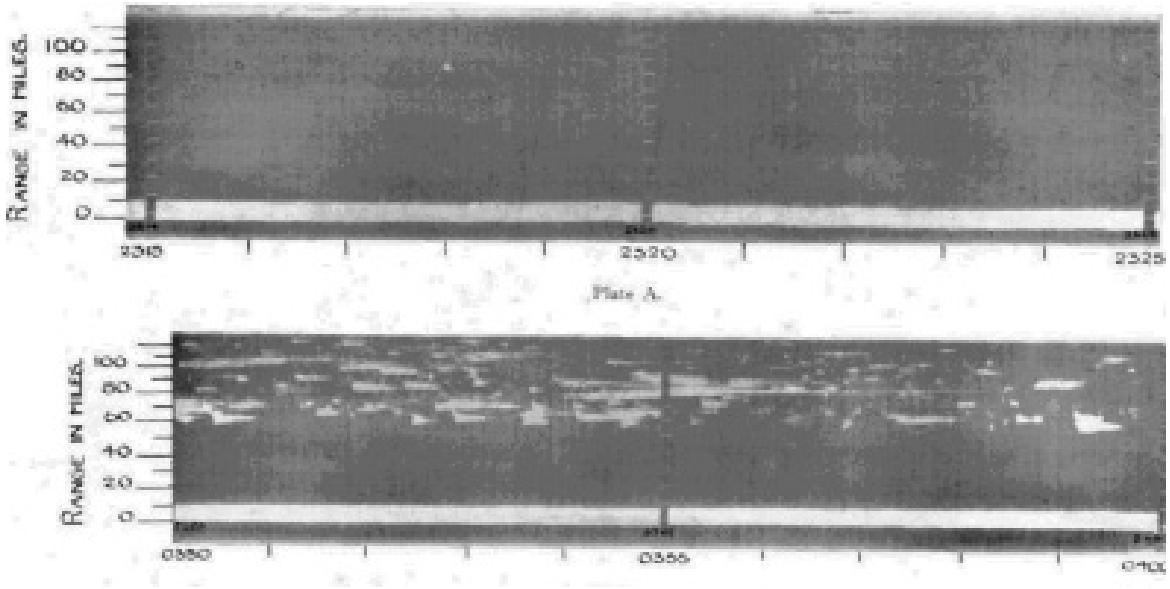

Figure 8. Echo range-time records at 27 MHz with 10 minute records: (upper) October 9, 1946, GMT 2315; (lower) October 10, 0350 at time of the Giacobinid shower influx (reprinted by permission from Macmillan Publishers Ltd: Nature, [33], copyright 1946).

geometry was also used to deduce shower radiants by McKinley and Millman in 1949 [32].

As reported in 1946 and 1947, Appleton and Naismith [33, 34] also used film recording of a CRT display. Operating at 27 MHz with 15 ms, 50 Hz pulse-repetition-frequency pulses directed vertically, they maintained a two-year survey daily from January 1944. This included the Giacobinid shower of October 10, 1946. Figure 8 shows their range-time plot, in which Plate B showed the very high influx rate from October 10, 0350 to 0400 GMT. The Giacobinids were also monitored using 3 MHz by Pierce, reported in 1947 [35], recording a meteoric *E* layer with substantial deposition sufficient to maintain ionization in the layer for four hours.

In 1947, Eckersley [36] proposed an analogy of meteor reflection with the case of alpha-particle scattering from heavy atoms. This comparison is not applicable, since the geometry is quite different because the model was of a small spherical-like cloud, but the meteor case is not spherically symmetrical. It was also mistakenly proposed that the ionization target should move with the meteoroid (as is actually the situation for the quite different case of the head-echo-producing plasma).

In 1948, Eastwood and Mercer [37] reported on a surveillance from January 1945 to July 1946 at 20-45 MHz, with a vertical stack of horizontal half-wave dipoles and cine-camera photographic CRT display. This was able to record echo amplitude as a function of time for individual echoes at a sampling rate of 25 Hz. Diurnal, seasonal, and solar-cycle rates were studied, as well as the dependence of the echo range distribution on elevation pattern, and its relation to antenna type and ground height. Examination was also made of the echo rate dependence on operating radar frequency, and a study of the influence of the July 9, 1945, solar eclipse.

In 1948, Allen [38] described forward scatter at 40 MHz (carried out during 1943), reporting chart recording of "bursts," and noting that longer scatter durations occurred at 10 MHz. Diurnal and seasonal forward-scatter bursts from several commercial stations were examined. The study noted simultaneous visual meteors and bursts via scatter to indicate that reflections were orthogonal to the trajectory. The forward-scatter configuration was analyzed by Geometrical Optics with modifications by Manning and Villard in 1948 [39].

The diurnal-seasonal rate characteristics mapped [37, 37, 38] can be interpreted in terms of astronomical effects. Although influenced by the orientation and width of the radar antenna's radiation pattern, the meteor influx at any latitude is dominated by the elevation of the Earth's apex (the upstream vector of the Earth's orbital motion) above the radar's local horizon.

A summary of the theoretical understanding of the meteor-scatter process to date was provided by Lovell and Clegg in 1948 [40]. They presented a model of the formation process of the plasma trail with correct geometry, and also measured the wavelength dependence of meteor-reflection coefficients. This work was later extended by Kaiser and Closs in 1952 [41].

4. Meteor-Scattering Theory

A firm theoretical foundation of radiowave scattering from meteoric ionization is necessary to provide sound linkages between the interaction of meteoroid bodies with the atmosphere and the relationship between the characteristics of returned signals and other parameters. These parameters include meteoroid mass, trajectory, speed, and conditions in the meteoric plasma and its complex meteor environment: atmospheric parameters, wind field, and geomagnetic field.

There are two particular radar-observing geometries for meteor scatter that have evolved (originally, from distinctly observed echo types). The first is reflection orthogonally from the linear column of ionization, so that scattering takes place from a long (~1km) cylinder of plasma, observed employing a transverse geometry producing a trail echo or *body echo*. The second is reflection from the spheroidal plasma immediately surrounding the ablating meteoroid, observed employing radial geometry: the *head echo*. In the former configuration, the radar's line-of-sight is strictly orthogonal to the meteor trajectory, and in the latter, the line-of-sight is broadly radial. Here, we follow the above early observational work of Sections 2 and 3, and focus on the transverse echo situation. Some aspects of the head echo (see Section 4.4) have been described [42], and some associated studies have been recently outlined in the *Radio Science Bulletin* [43] and by Mathews [53].

The formulation of a theory of radar scattering for the transverse reflection geometry, producing a broadside body echo, can be regarded in essentially two stages:

1. To treat the ionization column as an instantaneously formed long column, which expands by ambipolar diffusion, retaining a Gaussian cross section (ignoring any distortion from geomagnetic field forces), and remaining stationary (not moving with the neutral atmosphere). It is thus an assembly of electrons of time-increasing radius.

2. To superimpose a modulation produced by the finite creation time of the plasma.

4.1 The Scattering Cross Section

For an assembly of electrons in the meteor case with electrons at essentially the same range, the effective total scattering cross section depends on the summation of phase contributions from individual electrons, on the overall geometry, and on whether secondary radiative effects are present (depending therefore on electron number density). At meteoric altitudes (~100 km), electron-neutral collisions can be neglected in the radiowave scattering process. Coherent reflection from the meteor plasma provides the radar target. A single electron has a scattering cross section to an incident electric field of $\sigma_e = 4\pi r_e^2 \sin^2 \gamma$, where r_e is the classical scattering radius, and γ is the angle between the *E*-field vector of the incident wave and the scattering direction. For the radar backscatter case, with co-located transmitter and receiver, $\gamma = 90°$ and $\sigma_e \sim 10^{-28}$ m^2.

The signal power available to a receiving antenna, p_r, from a target of scattering cross section σ at range *R*, using transmitting and receiving antennas of gains G_T and G_r, with transmitting power P_T and operating wavelength λ, is of the standard form

$$p_r = \frac{P_T G_T G_r \lambda^2}{64\pi^3 R^4} \sigma \cdot$$

The problem reduces to determining an expression for the total scattering cross section, σ, for the particular equipment, geometry, and meteor train parameters.

4.2 Behavior in Limiting Cases

The large range of masses of meteoroids incident on the Earth's atmosphere means a substantial range in ionization densities is generated. The ionization distribution has the form of a tapered cylinder, with a larger radius at greater heights resulting from the larger atmospheric mean free path and the finite time to diffuse. For the limiting case of a weak plasma, the radio waves pass through the plasma unaffected. The scattering of the incident radio waves from electrons takes place independently without any secondary or interference effects. The total scattering is then the summation over all electrons in a cross section of the meteor train. Such a situation is described as an *under-dense* train. At the instant of formation of such a train, if the plasma radius at formation, r_0, is very small compared to the radar wavelength, λ, then for evaluating the reflection, all electrons can be considered to be situated on the train's axis and with the same scattering phase. For the opposite case of an extremely dense plasma, secondary scattering is an important feature, and the incident wave is grossly disturbed. The dielectric constant of the medium is sufficiently negative for total reflection to occur at some critical boundary. Thus, as diffusion increases the dimensions of the boundary, the reflection coefficient increases. Train expansion reduces the electron number density on the axis so the dielectric constant becomes less negative, the critical radius collapses to the train axis, and subsequently, individual electron scattering operates as the incident wave penetrates the plasma column. Such a dense expanding train can be regarded in its reflection behavior for the limiting high-electron-density case as a metallic cylinder the radius of which expands for a period before collapsing. This regime is termed an *over-dense* train.

The transition between the two regimes can be defined in terms of the attenuation of the incident wave. Since the dielectric constant of the plasma is negative for the over-

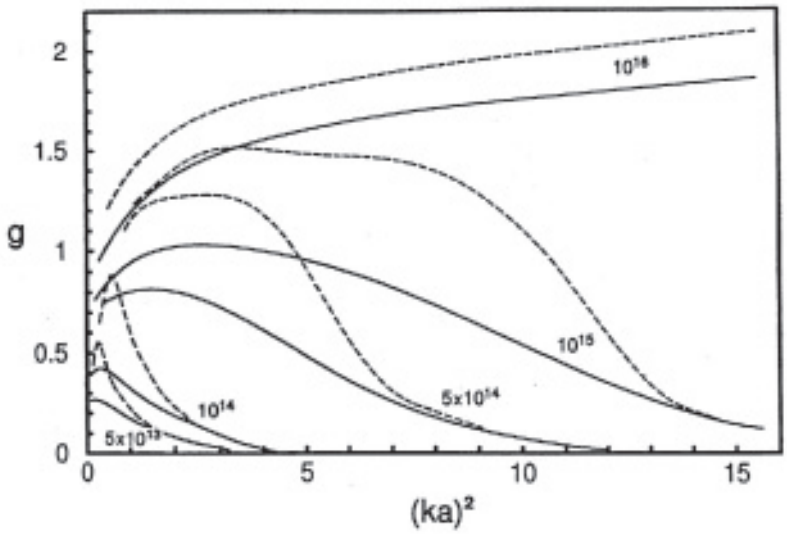

Figure 9. The reflection coefficient as a function of time: full line: parallel polarization; broken line: transverse polarization (reprinted from [44] with permission from Elsevier).

dense case, the incident wave is an evanescent wave. If the plasma is of such a critical density that the amplitude of the evanescent wave is reduced to e^{-1} on the axis (in analogy with the skin depth for a metal, although for a metal, the concept employs the ohmic conductivity), the train plasma is described as being transitional. This definition means that the attenuation distance, equal to the radius of the cylinder, a, is $\lambda/2\pi$. The corresponding critical electron density, $n_c = q/\pi a^2$, can be related to the radiowave frequency and plasma conditions by $n_c = \omega^2 m\varepsilon_0/e^2$ with m and e being the electron mass and charge, respectively, and ε_0 being the free-space permittivity. The corresponding critical electron line density is $q = 8.9\times10^{13}$ m^{-1} (a value that is independent of the probing radio frequency). This was derived assuming a cylinder of uniform cross section (a more-realistic Gaussian profile changes the value only slightly). Such a value corresponds to a meteor optical magnitude of approximately +5 (near the limit of unaided-eye visibility).

4.3 Reflection from an Instantaneously Formed Column

The time variation of the reflection coefficient cannot be derived in analytical form. A full-wave treatment, employing numerical solutions, is necessary [44]. To keep the problem tractable, it is assumed that (ambipolar) diffusion operates, retaining a Gaussian cross section with initial size established by thermal expansion to a few mean free paths. A more complete treatment shows that the distortion caused by the geomagnetic field can have a marked effect when at large heights the electron-neutral collision frequency becomes small compared with the electron gyro-frequency. Including fully the polarization field within the meteor plasma and the effects of ambient background ionization provide a more detailed analysis (e.g., [45]).

In the general case, the interaction of the EM wave is considered in terms of a reduced dielectric constant within the plasma. A plane wave incident at arbitrary angle to the column's axis can be resolved into components parallel to and transverse to the axis. Within the column, the E and B fields must satisfy Maxwell's equations, and we expand the field components in cylindrical harmonics. Outside the train, the field is the sum of the incident plane wave and the scattered (cylindrical) wave. The incident waves are expressed in terms of a series of Bessel functions. The cylindrical wave is expressed in terms of Hankel functions of the first kind, the order of which is dictated by the geometry and radial dependence for this case. To yield reflection coefficients, numerical solutions of the equations are matched onto asymptotic forms representing the incident and scattered waves: the field components at the matching radius. Numerical integration of the field equations [44] provides solutions (powerful computing techniques that have become available allowing such full-wave solutions were not available to aid early attempts [41]). These present reflection coefficients and map polarization changes in the scattered field early in the echo lifetime, and the resonance that can occur when the incident electric vector is transverse to the train's axis (so the electrons are being driven across a density gradient, producing charge separation).

Solutions are presented in terms of time from train formation at $t = 0$. q is the electron linear density, in electrons m^{-1}, under a diffusion coefficient, D, where the e^{-1} plasma-column radius, a, is given by $a^2 = r_0^2 + 4Dt$, with r_0 being the initial Gaussian radius. Some results of such a full-wave treatment, providing the complex reflection coefficient, are shown in Figures 9 and 10, where the orthogonal plane polarizations are shown. The reflection coefficient, g, is related to the scattering cross section by $g^2 = \sigma\pi/2R\lambda$. λ is the operating free-space wavelength, and the wavenumber is $k = \lambda/2\pi$. For $ka > 1$, the horizontal axis in Figure 9 is then approximately proportional to time. Figure 9 shows the reflection coefficient, g, for the parallel and transverse cases as a function of q over a range of line densities showing the echo-transition region, where the change from strictly exponential decay for small q can be

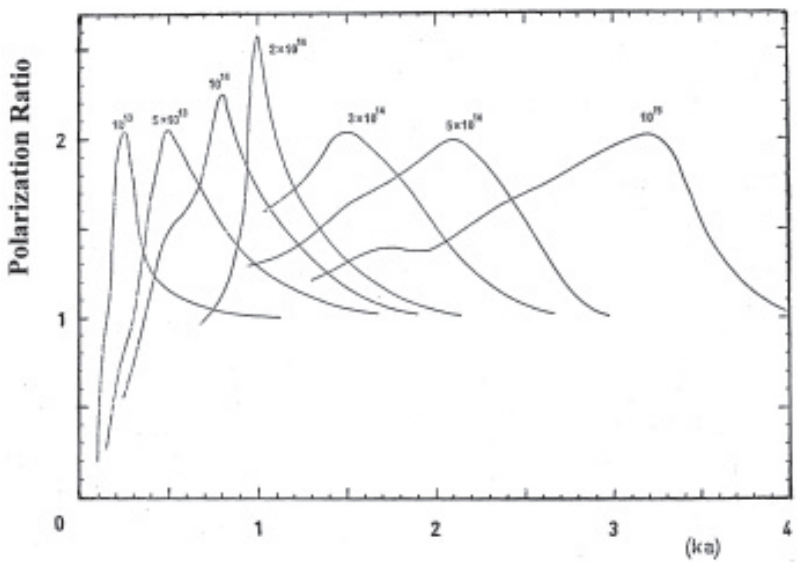

Figure 10. The time variation of the polarization ratio for various q electrons m^{-1} (reprinted from [44] with permission from Elsevier).

seen. It is clear that there is a range of a factor of $\sim 10^2$ in q in the bridging region between the two limiting cases. Figure 10 shows the polarization ratio and the resonance peak for the optimum value of *ka*. Two situations might be envisaged. If the train is created with a small r_0, then it has to diffuse to a critical radius for resonance to occur. If r_0 is too large, then no resonance condition will be possible.

The echo behavior can be summarized as follows.

4.3.1 Under-Dense Echoes

The later stages of an under-dense echo are dictated by diffusion. As the plasma expands, phase summation of the individual electron contributions in a train's cross section results in a reduction in the echo reflection coefficient, *g*. If a Gaussian train cross section is maintained during expansion, the change in *g* will be an exponential function of time. The echo decay is described by $\exp(-t/t_d)$, with $t_d = \lambda^2/32\pi^2 D$. The role of the geomagnetic field in producing anisotropic diffusion has been emphasized. The resulting distortion of the plasma column produces a look-angle dependency on the decay of the radar echo. For simplicity of treatment, assuming a Gaussian profile and circular symmetry at formation, the plasma column distorts into a generally elliptical cross section. With inhibited diffusion, the echo decay rate can be very much less, and enhanced echo lifetimes can result under certain geometries.

4.3.2 Over-Dense Echoes

A full treatment of the reflection from a Gaussian dense plasma is complex, because of the effects of the weaker ionization in the outer regions of the column on the wave. However, a simple picture enables an estimate to be made of the echo characteristics of an over-dense plasma.

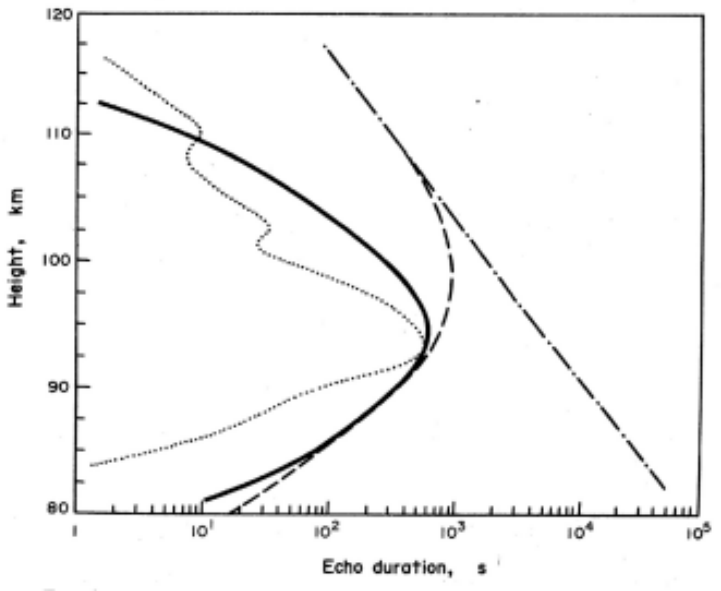

Figure 11. The height variation of over-dense meteor echo durations for a radar frequency of 30 MHz (reprinted from [47] with permission from Elsevier)
–●–●–● : the expression $T_{ov}q = 6\times10^{18}\,m^{-1}$ all heights.
- - - -: the expression T_{ov} and including ionic reactions, $q = 6\times10^{18}\,m^{-1}$ all heights; ——— : the expression T_{ov} including ionic reactions height profile of deposited ionization with $q_{max} = 6\times10^{18}\,m^{-1}$ at 88 km. : ●●●●●●● measured for enduring Perseid echo [46].

For a general over-dense plasma, there will be a critical radius, r_c, at which the plasma has a critical electron number density, n_c (for which the dielectric constant is negative). This will occur when

$$n_c(r_c,t)=\left(\frac{q}{\pi a^2}\right)\exp\left(-\frac{r_c^2}{a^2}\right).$$

Defining the duration of an over-dense echo as the time for the axial electron number density to fall to n_c, so that $n_c(0,t)=q/\pi a^2=\omega^2 m\varepsilon_0/e^2$, then the over-dense duration is

$$T_{ov}=\left(\frac{e^2}{4\pi\varepsilon_0}\right)\left(\frac{q}{\omega^2 D}\right)-\left(\frac{r_0^2}{4D}\right),$$

where the last term represents the "age" of the train at the start (the time to diffuse to a radius of r_0) under normal diffusion, and is only comparable with the first term in the upper meteoric region, >105 km. This diffusion-limited echo duration will be modified by the action of ionic processes removing electrons from the train plasma. Models can be made of how echo durations will be curtailed by the effective decrease in the value of the line density, q (chemistry influence is usually negligible for under-dense echoes). Ozone is expected to be the dominant gas initiating the chain of reactions responsible for the deionization of trains. Because of the solar control of lower thermosphere O_3 densities, the durations of echoes under daytime conditions will therefore be markedly reduced compared with nighttime. The modeled electron-loss characteristics can then be inserted in the echo durations to model the echo lifetimes as a function of altitude. Illustrations are given (for a radar frequency of 30 MHz) in Figure 11 of how T_{ov} values are expected to vary with altitude. The approximately exponential downwards increase in T_{ov} due to both an increase in q (for a given meteor) and an atmospheric-density increase are countered by the increasingly short chemical lifetime of electrons below ~95 km. This relates to the observation of occasional long-enduring echoes (for example, [20, 22]). A specific illustration of the effect is to be found in the altitude variations of long-enduring Perseid meteor echoes [46]. In that study, triple-station ranging fixed the echo altitude, so that the echo duration could be followed by the radar system as a function of altitude during the persisting ~ 9 min train. As predicted ([47]), the most enduring section of the diffusing plasma occurred at an altitude close to 93 km (Figure 11).

This sensitivity of echo behavior to ambient gases presents a method of monitoring the atmosphere. Measurements of the characteristics of radar-echo lifetimes can enable estimates to be made of the altitude profiles of the important atmospheric species O_3 ([48, 49]) in a altitude regime that is largely inaccessible by other techniques.

It is instructive to provide an example of echo-duration characteristics by reference to a historical case. The first reported echo-duration distribution measurements [22] can be interpreted in terms of the theoretical behavior. In Figure 3 of this work, there was a preponderance of short echoes, with 85% having a duration < 2.5 s and 6% > 10 s. The types of radar systems employed in the period, ~1940, using a transmitting power of a few kW and low antenna gains, would have had a limiting sensitivity of $q \sim 10^{12}\,\mathrm{m}^{-1}$ This corresponds to a meteoroid mass of $\sim 10^{-6}$ kg, and a visual magnitude of ~+10. The meteoroid population mass content follows a power law: there are many more small bodies than large bodies. As a consequence, the radars of this type detect many more under-dense short echoes than over-dense. The mode duration [22] was ~ 1.5 s, and from the expression for t_d above and an operating frequency of 7.59 MHz, the inferred diffusion coefficient, D, was 6.6 $\mathrm{m^2 s^{-1}}$, corresponding to a height of ~95 km [50]. This is a representative average ablation height for meteors.

More recent work has extended the treatment to recognize the role of plasma instabilities produced by ionization gradients and E fields created by the action of ambient neutral wind, or resulting from the action of diffusion across the geomagnetic field [51]. The growth of instabilities depends on the background general ionospheric ionization. Such plasma instabilities result in meter-scale irregularities, having a geometry controlled by the geomagnetic field, which may result in range-spread echoes and enhanced echo durations. The effect depends on the angle between the radar-echo direction and the meteor trail [52, 53, 54].

In the interaction of an ablating meteoroid with the atmosphere, the ionization along the trajectory is distributed so that the electrons and ions are deposited over the physical path length. This is governed by the mass-loss rate, which depends on the track's zenith angle, Z, so that $q \sim \cos Z$. An echo close to the zenith would be generated by a meteor with a near-horizontal trajectory and therefore a low q, and, in consequence, low detection rates. This bias would be responsible for the sparse meteors recorded for vertical ionospheric-sounding antennas in the 1930s, and for improved detection conditions using low-elevation aircraft-seeking radars in use from 1940 to 1945.

In the case where the transmitter and receiver have a substantial ground separation, the situation is that of forward scatter (γ not equal to 90°). The geometry becomes that of oblique reflection, being an extension [55] to the method outlined here.

4.4 Reflection from the Developing Plasma

In order to complete the modeling of the time variation of meteor scattering, it is necessary to modulate the instantaneously formed ionization train by taking into account the finite time interval to create the plasma column.

This formation process is modeled by assuming that the free electrons can be regarded as essentially confined to the axis (so $r_0 \sim \lambda$). This approach permits an analysis in terms of diffraction, where the relative phases of contributions of segments of the forming plasma sum to provide the scattered field. The time behavior of the body echo arises as the meteoroid deposits ionization over increments in length at a changing range, and therefore with changing phase. The concept of a Fresnel "zone" (rather than "interval"), often used in describing meteor diffraction, arises from its use in the two-dimensional case in optical diffraction on a plane surface, and derives from its use in describing the operation of the zone-plate optical device. Such a zone plate is described by annuli having successive (usually π) increments in phase. Such a geometry, employing a zone or area, is not strictly appropriate in the present meteor case, where the contributions are distributed in one dimension. The term "Fresnel interval" or "Fresnel length" is more realistic in the meteor case involving linear scatter, producing a cylindrical wavefront.

The time variation of the scattered electric field and its phase – the complex electric field – is the vector sum from elements along the meteoroid's trajectory, with contributions from adjacent Fresnel intervals being π out of phase. The oscillatory electric field provides the backscattered echo, with the received power at the antenna being

$$p_r = \frac{P_T G_T G_r \lambda^3 \sigma_e}{256\pi^3 R^3}\left(C^2 + S^2\right)q^2 ,$$

where *C* and *S* are the Fresnel integrals. These are defined by

$$C = \int_{-\infty}^{X} \cos\left(\frac{\pi x^2}{2}\right)dx$$

and

$$S = \int_{-\infty}^{X} \sin\left(\frac{\pi x^2}{2}\right)dx \cdot$$

X is the Fresnel parameter, proportional to the distance *Vt* (with *V* being the meteor velocity) of the scattering element from the origin ($X = 0$), measured in Fresnel intervals: $X = 2Vt/\left(R\lambda\right)^{1/2}$. The maximum value of the resultant electric field can be regarded as due to an effective train scattering length of about one Fresnel interval, $\sim\left(R_0\lambda/2\right)^{1/2}$, either side of the $X = 0$ condition (the t_0 point where the trajectory is orthogonal to the radar sight line). The resultant maximum scattering cross section depends on the square of the number of contributing electrons. The maximum echo power available at the radar antenna occurs when the Fresnel parameter $X = 1.217$. Thus,

$$p_r = 1.26\times10^{-32} P_T G_T G_r \left(\lambda/R\right)^3 \left(C^2 + S^2\right)q^2$$

watts, with *q* electrons m^{-1}.

The time behavior of the received signal has a close optical analogy with the angular changes in light intensity in the case of diffraction at a straightedge in classical optics, or the cylindrical-wavefront radio electric field in the radio shadow produced by an obstacle. The complex diffraction

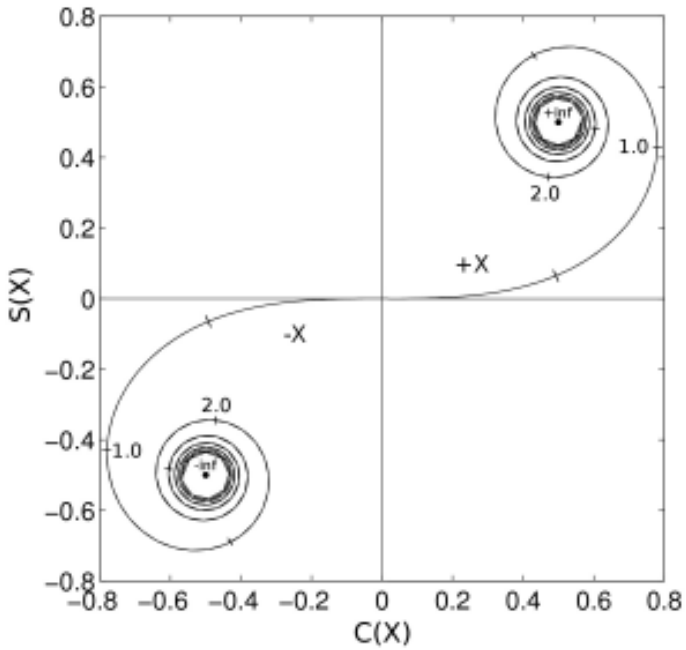

Figure 12. The Cornu Spiral: an orthogonal plot of $C(X)$ and $S(X)$. The distance along the meteor trajectory from the orthogonal point on the meteor trajectory is represented by the distance along the curve from the (0,0) point to the limits of ± 8.

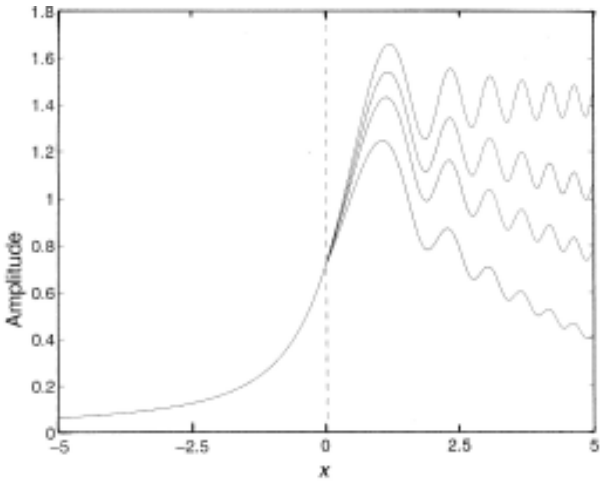

Figure 13. The time variation of the scattered electric field (echo amplitude in arbitrary units) with X as the Fresnel parameter proportional to time. The top trace is for no diffusion; the three other traces show the pattern of echo decay for cases of increasing diffusion.

behaves in these cases in a way described very usefully by the Cornu spiral (Figure 12). The relative echo amplitude at any time (and therefore the value of *X*) is given by the length of a vector from the point $C = -0.5$, $S = -0.5$, ($X = -\infty$), to a point having a particular value of *X* on the curve. The time variation of the echo-diffraction electric field is proportional to $\left(C^2 + S^2\right)^{1/2}$ (Figure 13). The variation of phase, ϕ, is described (Figure 14) by $\tan\phi = -(0.5+S)/(0.5+C)$. As the meteor approaches the orthogonal position t_0, there is a rapid rise of the signal as an increasing number of half-period Fresnel intervals contribute. The phase increases monotonically (as the meteoroid-generated plasma approaches the radar), reaching a maximum of $-\pi/6$ (strictly, $-29.4°$) when $X = 0.57$ (defining the phase as $-\pi/4$ when $X = 0$).

As the meteoroid moves through successive Fresnel intervals, both the signal and its phase oscillate. At the instant of maximum ($X = 1.22$), about 90% of the energy is contributed by the central Fresnel interval, extending over a distance along the meteor ionization train of about 2 km for an ~30 MHz radar. Both the post-t_0 oscillatory echo amplitude [56] and the pre-t_0 phase gradient [57, 58] provide techniques for measuring the meteor's scalar speed. The early life of a meteor echo formed with orthogonal geometry is dictated by diffraction, independent of the *q* value and of whether an under- or over-dense plasma. Indeed, the rise time of an echo can yield an estimate of the meteoroid's speed [59]. After the t_0 point, the phase, while undergoing small ($< \pi/20$) oscillations, may show gross phase changes caused by the motion of the plasma in the ambient neutral wind. This provides a technique used to monitor the atmospheric wind field in studies over a wide range of scales, from gravity waves to planetary waves. All of these phase effects would have contributed to the rapid phase behavior noted in early [26] reports.

For the case of the head echo (for example, Figure 7) produced in the radial-reflection geometry, a similar analysis can be applied to make an estimate of the scattering. We will not discuss that geometry further here, except to note the expected difference in scattering cross sections. Since when viewing the head plasma with radial geometry the Fresnel size is $\sim \lambda/4$, the ratio of the radial to transverse scattering cross sections is $\sim \lambda/8\pi^2 R$, or approximately 10^{-6} for an HF radar.

4.5 Critical Viewing Geometry

Some echoes may not be fully formed because of the antenna's angular response. Wave diffraction and the associated phase behavior are responsible for the restrictive orthogonal geometry governing the radar's transverse reflection mode. There are two conditions necessary for a given meteor train to provide an echo: for the particular radar line-of-sight, the central Fresnel interval should be within the antenna's radiation pattern; and the scattered power should be above the detection threshold of the radar system. As discussed above, complete echoes can be expected in cases where a substantial fraction of the central Fresnel zone lies within the radiation pattern. This constraint is very strict, so that many meteors producing ionization trails above the observer's horizon within the antenna's beam but that are not formed with critically favorable geometry are undetectable. If the t_0 point is formed near the high elevation edge of the radar's beam, then contributions from pre-t_0 zones ($X < 0$) are attenuated, and the resulting echo is due dominantly to ionization situated with $X > 0$, and the large phase growth is absent. Conversely, meteor trains formed near the low elevation edge of the antenna's beam can only produce contributions from the $X < 0$ region. Radars employing very narrow (pencil-beam) antenna radiation patterns – so that the size of the Fresnel interval is comparable with the physical distance intercepted by the antenna at the echoing altitude – will sample a large proportion of such truncated echoes.

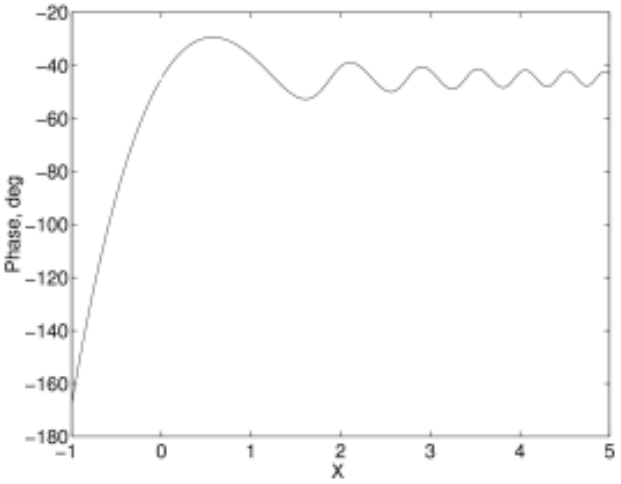

Figure 14. The phase (in degrees) of the scattered electric field for longitudinal polarization with X as the Fresnel parameter proportional to time. The phase was normalized to a value of $-45°$ at the t_0 point when $X = 0$.

4.6 Additional Factors

In order to complete the description of the interaction of radio waves with meteoric ionization trains and the characteristics of radar signatures, there are additional effects that need attention. Their impacts depend on sampling wavelength; the speed of the meteoroid; the state of the atmosphere; and the finite initial radius of the plasma, a value that depends on height and meteoroid velocity. The finite speed means that diffusion of the train results in a larger train radius at greater heights. The medium below the reflection height may impose Faraday rotation of the plane of polarization and absorption. These factors have been previously summarized [60].

5. Conclusions

It has been 80 years since the earliest radio reports of transient ionospheric echoes that were recognized in due course as meteors. Early investigators of the ionosphere sought to understand the fleeting phenomenon of nature that radio transmissions detected, while theoretical work was later able to formulate our understanding of the echo signatures. Radar meteors are now a valuable tool in many areas: atmospheric probing of density, temperature, and wind-field behavior (for example, [61]), in height regimes difficult to access by other means. They are a tool that opened up a whole new perspective of astronomical monitoring of objects impacting into the Earth's atmosphere and the solar system dust cloud. Radar techniques allowed us to measure the speed of meteoroids through the atmosphere and, using multiple sites, to determine their orbits in space [62, 63].

6. References

1. R. A. Heising, "Experiments and Observations Concerning the Ionized Regions of the Atmosphere," *Proc. Inst. Radio Engn*., **16**, 1928, pp. 75-99.

2. T. L. Eckersley, "An Investigation of Short Waves," *J. Instn. Elec. Engrs*., **67**, 1929, pp. 992-1028.

3. E. V. Appleton, "On Some Measurements of the Equivalent Height of the Atmospheric Ionized Layer," *Proc. Roy. Soc*., **A126**, 1930, pp. 542-569.

4. A. M. Skellett, "The Effect of Meteors on Radio Transmission Through the Kennelly-Heavyside Layer," *Phys. Rev*., **37**, 1931, p. 1668.

5. G. W. Pickard, "A Note on the Relation of Meteor Showers and Radio Reception," *Proc. Inst. Radio Engn*., **19**, 1931, pp. 1166-1170.

6. E. V. Appleton and R. Naismith, "Some Measurements of Upper-Atmospheric Ionization," *Proc. Roy. Soc*., **A137**, 1932, pp. 36-54.

7. J. P. Schafer and W. M. Goodall, "Kennelly-Heaviside Layer Studies Employing a Rapid Method of Virtual-Height Determination," *Proc. Inst. Radio Engn*., **20**, 1932, pp. 1131-1148.

8. J. P. Schafer and W. M. Goodall, "Observations of Kennelly-Heaviside Layer Heights During the Leonid Meteor Shower of November 1931," *Proc. Inst. Radio Engn.*, **20**, 1932, pp. 1941-1945.

9. A. M. Skellett, "The Ionizing Effect of Meteors in Relation to Radio Propagation," *Proc. Inst. Radio Engn*., **20**, 1932, pp. 1933-1939.

10. E. V. Appleton and R. Naismith, "Weekly Measurements of Upper-Atmospheric Ionization," *Proc. Phys. Soc*., **45**, 1933, pp. 389-398.

11. J. A. Ratcliffe and E. L. C. White, "Some Automatic Records of Wireless Waves Reflected from the Ionosphere," *Proc Phys. Soc*., **46**, 1934, pp. 107-115.

12. S. K. Mitra, P. Syam and B. N. Ghose, "Effect of a Meteoric Shower on the Ionosphere," *Nature*, **133**, 1934, pp. 533-534.

13. A. M. Skellett, "The Ionizing Effect of Meteors," *Proc. Inst. Radio Engn*., **23**, 1935, pp. 132-149.

14. E. V. Appleton, R. Naismith and L. J. Ingram, "British Radio Observations During the Second International Polar Year 1932-33," *Phil. Trans*., **A236**, 1937, pp. 191-259.

15. R. A. Watson Watt, A. F. Wilkins and E. G. Bowen, "The Return of Radio Waves from the Middle Atmosphere," *Proc. Roy. Soc*., **A161**, 1937, pp. 181-196.

16. J. N. Bhar, "Effect of Meteoric Shower on the Ionization of the Upper Atmosphere," *Nature*, **139**, 1937, pp. 470-471.

17. T. L. Eckersley, "Irregular Ionic Clouds in the E-Layer of the Ionosphere," *Nature*, **140**, 1937, pp. 846-847.

18. A. M. Skellett, "Meteoric Ionization in the E Region of the Ionosphere," *Nature*, **141**, 1938, p. 472.

19. J. A. Pierce, "Abnormal Ionization in the E Region of the Ionosphere," *Proc. Inst. Radio Engn*., **26**, 1938, pp. 892-908.

20. E. V. Appleton and J. H. Piddington, "The Reflexion Coefficients of Ionospheric Regions," *Proc. Roy. Soc*., **A164**, 1938, pp. 467-476.

21. E. V. Appleton, R. Naismith, and L. T. Ingram, "The Critical-Frequency Method of Measuring Upper-Atmospheric Ionization," *Proc. Phys. Soc*., **51**, 1939, pp. 81-92.

22. T. L. Eckersley, "Analysis of the effect of Scattering in Radio Transmission," *J. Instn. Elec. Engn*., **86**, 1940, pp. 548-567.

23. P. M. S. Blackett and A. C. B. Lovell, "Radio Echoes and Cosmic Ray Showers," *Proc. R. Soc. London*, **177**, 1941, pp. 183-186.

24. C. D. Ellyett, private communication

25. J. A. Pierce, "A Note on Ionization by Meteors," *Phys. Rev*., **59**, 1941, pp. 625-628.

26. T. L. Eckersley and F. T. Farmer, "Short Period Fluctuations in the Characteristics of Wireless Echoes from the Ionosphere," *Proc. Roy. Soc*., **A184**, 1945, pp. 196-214.

27.E. V. Appleton, "The Scientific Principles of Radiolocation," *Instn. Elec. Engn*., **92**, 1945, p. 340.

28.O. P. Ferrell, "Meteoric Impact Ionization Observed on Radar Oscilloscopes," *Phys. Rev*., **69**, 1946, pp. 32-33.

29. J. S. Hey and G. S. Stewart, "Derivation of Meteor Stream Radiants by Radio Reflexion Methods," *Nature*, **158**, 1946, pp. 481-482.

30. J. S. Hey and G. S. Stewart, "Radar Observations of Meteors," *Proc. Phys. Soc., London*, **59**, 1947, pp. 858-883.

31.J. P. M. Prentice, A. C. B Lovell and C. J. Banwell, "Radio Observations of Meteors," *Mon. Not. Roy. Astr. Soc.*, **107**, 1947, pp. 155-163.

32.D. W. R. McKinley and P. M. Millman, "A Phenomenological Theory of Radar Echoes from Meteors," *Proc. Inst, Radio Engn.*, **37**, 1949, pp. 364-375.

33.E. V. Appleton and R. Naismith, "Radar Detection of Meteor Trails," *Nature*, **158**, 1946, pp. 936-938.

34.E. V. Appleton and R. Naismith, "The Radio Detection of Meteor Trails and Allied Phenomena," *Proc. Phys. Soc*., **59**, 1947, pp. 461-473.

35.J. A. Pierce, "Ionization by Meteoric Bombardment," *Phys. Rev*., **71**, 1947, pp. 88-92.

36.T. L. Eckersley, "Evaporation of Meteors," *Nature*, **160**, 1947, p. 91.

37.E. Eastwood and K. A. Mercer, "A Study of Transient Radar Echoes from the Ionosphere," *Proc. Phys., Soc*., **61**, 1948, pp. 122-134.

38.E. W. Allen, "Reflections of Very-High-Frequency Radio Waves from Meteoric Ionization," *Proc. IRE*, **36**, 1948, pp. 346-353.

39.L. A. Manning and O. G. Villard, "VHF Reflections from Meteors," *Proc. IRE*, **36**, 1948, pp. 1255-1257.

40.A. C. B. Lovell and J. A. Clegg, "Characteristics of Radio Echoes from Meteor Trails: I. Intensity of the Radio Reflections and Electron Density in the Trails," *Proc. Phys. Soc. London*, **60**, 1948, pp. 491-498.

41.T. R. Kaiser and R. L. Closs, "Theory of Radio Reflections from Meteor Trails I," *Phil. Mag*., **43**, 1952, pp. 1-32.

42. J. D. Mathews, D. D. Meisel, K. P. Hunter, V. S. Getman, Q. Zhou, "Very High Resolution Studies of Micrometeors Using the Arecibo 430 MHz Radar," *Icarus*, **126**, 1997, pp. 157-169.

43.A. Pellinen-Wannberg, G. Wannberg, J. Kero, C. Szasz and A. Westman. "The Impact of High-Resolution Radar on Meteor Studies: The EISCAT Perspective," *The Radio Science Bulletin*, No. 324, 2008, pp. 17-28.

44.E. M. Poulter and W. J. Baggaley, "Radiowave Scattering from Meteoric Ionization," *J. Atmos. Terr. Phys*., **39**, 1977, pp. 757-764.

45. Y. Dimant and M. Oppenheim, "Meteor Trail Diffusion: 1. Simulations," *J. Geophys. Res.*, **111**, 2006, DOI:10.1029/2006JA011797.

46.D. W. R, McKinley, "Radar Echo Durations and Height of a Perseid Meteor," *J. Atmos. Terr. Phys.*, **8**, 1956, pp. 76-82.

47.W. J. Baggaley, "The De-Ionization of Dense Meteor Trains," *Planet. Space Sci.*, **26**, 1978, pp. 979-981.

48.W. J. Baggaley, "The Interpretation of Overdense Radio Meteor Echo Duration Characteristics," *Bull. Astr. Instit. Czech.*, **30**, 1979, p. 184.

49.J. Jones, B. A. McIntosh, and M. Simek, "Ozone and the Duration of Overdense Radio Meteors," *J. Atmos. Terr. Phys*., **52**, 1990, pp. 253-258.

50.CIRA-86, in D. Rees (ed.), "COSPAR International Reference Atmosphere: 1986, Part I: Thermosphere Models," *Adv. Space Res.*, **8**, 5-6, 1988.

51.Y. Dimant and M. Oppenheim, "Meteor Trail Diffusion: 2. Analytical Theory," *J. Geophys. Res.*, **111**, 2006, DOI:10.1029/2006JA011798.

52.Q.-H. Zhou, J. D. Mathews and T. Nakamura, "Implications of Meteor Observations by the MU Radar," *Geophys. Res. Lett*., **28**, 2001, pp. 1399-1402.

53.J. D. Mathews, "Radio Science Issues Surrounding HF/VHF/UHF Radar Meteor Studies," *J. Atmos. Sol. Terr. Phys.*, **66**, 2004, pp. 285-299.

54.A. Malhotra, J. D. Mathews and J. Urbina, "A Radio Science Perspective on Long-Duration Meteor Trails," *J. Geophys. Res.*, **112**, A12303, 2007, doi:10.1029/2007JA012576.

55.J. Jones and W. Jones, "Oblique Scattering of Radio Waves from Meteor Trains – Long Wavelength Approximation," *Planet. Space Sci.*, **38**, 1990, pp. 925-932.

56.C. D. Ellyett and J. G. Davies, "Velocity of Meteors Measured by Diffraction of Radio Waves from Trails During Formation," *Nature*, **161**, 1948, pp. 596-597.

57.W. J. Baggaley and J. Grant, "Techniques for Measuring Radar Meteor Speeds," *Earth Moon and Planets*, **95**, 2005, pp. 601-615.

58.W. K. Hocking, "Real-Time Meteor Entrance Speed Determinations Made with Interferometric Meteor Radars," *Radio Sci.*, **35**, 2000, pp. 1205-1220.

59.W. J. Baggaley, R. G. T. Bennett and A. D. Taylor, "Radar Meteor Atmospheric Speeds Determined from Echo Profile Measurements," *Planet. Space Sci*., **45**, 1997, pp. 577-583.

60.Z. Ceplecha, J. Borovicka, W. G. Elford, D. O. ReVelle, R. L. Hawkes, V. Porubcan, and M. Šimek, "Meteor Phenomena and Bodies," *Space Sci. Rev.*, **84**, 1998, pp. 327-471.

61.Ch. Jacobi, K. Fröhlich, C. Viehweg, G. Stober, and D. Kürschner, "Midlatitude Mesosphere/Lower Thermosphere Meridional Winds and Temperatures Measured with Meteor Radar," *Advances in Space Research*, **39**, 8, 2007, pp. 1278-1283.

62.W. J. Baggaley, R. G. T. Bennett, D. I. Steel and A. D. Taylor, "The Advanced Meteor Orbit Radar: AMOR," *Q. J. Roy. Astron. Soc.*, **35**, 1994, pp. 293-320.

63.J. Jones, P. Brown, K. J. Ellis, A. R. Webster, M. Campbell-Brown, Z. Krzemenski and R. J. Weryk, "The Canadian Meteor Orbit Radar: System Overview and Preliminary Results," *Planet. Space Sci.*, **53**, 2005, pp. 413-421.

Propagation Problems in Satellite Navigation

A. Hornbostel

Abstract

Satellite navigation is based on measuring the signal delay between transmission at the satellite and reception by the user's receiver. The modeling and correction of the additional delay due to the propagation through the atmosphere, and mitigation of signal disturbances in the user environment, therefore play an important role in the accuracy of the derived position solution. This paper provides an overview about the mechanisms of the main propagation phenomena that are relevant for satellite navigation, their magnitude, temporal and regional variations, and standard methods to correct and mitigate these phenomena.

1. Introduction

Positioning with satellite navigation systems, such as GPS or Galileo, is based on time-of-arrival measurements at the receiver of the signals transmitted from the satellite. The measured signal delays are converted to pseudo-ranges by multiplication by the speed of light. The prefix "pseudo" signifies the fact that these ranges do not correspond to the real geometrical distances to the satellites. This is because the receiver's clock is not synchronized to the satellite's system time, and the measured delays include additional contributions from system and propagation errors for which corrections must be made. For synchronization of the receiver clock to the system time, measurement data from at least four satellites must be available. The receiver's clock bias can then be solved for as a fourth unknown, together with the three unknown coordinates of the position, x, y, z, by triangulation. While system errors normally cannot be corrected in real time, propagation errors can be reduced by models or advanced signal processing. The remaining error depends on the type of measurements, e.g., single-frequency or dual-frequency measurements; signal characteristics, e.g., the carrier frequency and bandwidth; and the quality of the models used.

Satellite navigation signals are extremely weak when they arrive at the user's antenna: the nominal GPS power received at the ground is −157 dBW, which is below the noise level. Therefore, the signals are sensitive to shadowing by buildings or vegetation. Navigation signal are spread-spectrum signals. These are recovered from noise by de-spreading in the receiver, i.e., by correlation with a replica of the satellite's code. The time of arrival, i.e., the delay of the received satellite code, is also determined by this correlation process. If the direct signal is superposed with signals reflected from the user's environment due to multipath propagation, the peak of the correlation function becomes less unique, and the accuracy of the delay measurement is reduced.

Table 1 shows an error budget for the GPS standard positioning services with the L1 C/A code. The user equivalent range error (UERE) is shown, which is the rms range error that the user must expect on average, worldwide. Note that these are the residual errors after applying corrections.

Component	Error
Ephemeris	2.1 m
Satellite clock	2.1 m
Ionosphere	4.0 m
Multipath	1.4 m
Troposphere	0.7 m
Receiver noise	0.5 m
Total (rms)	5.3 m

Table 1. The GPS L_1 C/A error budget (UERE) [1].

A. Hornbostel is with the Institute of Communications and Navigation at the German Aerospace Center (DLR e.V.), Oberpfaffenhofen, D-82230 Weßling, PO Box 1116, Germany; Tel: +49 8153 282318; Fax: +49 8153 282328; E-mail: achim.hornbostel@dlr.de.

This is an invited *Review of Radio Science* from Commission F. A version of this paper appeared in the Proceedings of Wave Propagation in Communication, Microwave Systems, and Navigation (WFMN07), July 4-5, 2007, Chemnitz, Germany.

In the table, the main error contributions – besides orbit and satellite-clock errors – are due to propagation effects in the atmosphere, and multipath propagation in the user's environment. For single-frequency measurements in the L band, the ionospheric error is the dominant contributor to the whole error budget. The UERE budget demonstrates the importance of propagation modeling and the improvement of correction models for high-accuracy navigation. This is particularly true when orbit and clock errors will be reduced by the technological progress of future systems, such as Galileo and modernized GPS. The objective of this paper is therefore to provide an overview of the characteristics of the main propagation effects, and common correction and mitigation methods.

2. Propagation Path through the Atmosphere

Figure 1 shows the propagation path of the signals through the different layers of the atmosphere. Within these layers, the signal path and the propagation speed are influenced by the variation and gradient of the refractive index. Starting from the top, the signals first reach the ionosphere, where, due the existence of free electrons, the refractive index is smaller than one. The effect is that the group velocity of the signals is lowered compared to vacuum, but the phase velocity is enhanced. The concentration of free electrons increases with lower altitudes, where the highest concentration is around 300 km above the Earth's surface, and then again decreases. The corresponding gradient of the refractive index causes a curvature of the propagation path, as shown in the figure with a dotted line.

Between 50 and 100 km above the ground, the free electrons disappear. The signals start to propagate through the neutral atmosphere, which is composed of different atmospheric gases. With lower altitudes, the air pressure and density of the atmospheric gases increase, and the refractive index grows accordingly to values larger than one. The gradient of the refractive index again causes a curvature of the propagation path. However, this curvature is in the opposite direction to the curvature in the ionosphere. Here, both the group velocity and the carrier velocity are slowed down compared to the vacuum speed of light.

In lower part of the neutral atmosphere, the troposphere extends from 0 to about 8 km at the poles, from 0 to about 13 km in mid-latitudes, and from 0 up to 18 km at the equator. This makes the main contribution to the signal's delay, because it is the densest layer. It contains most of the air mass, and practically the total amount of water vapor of the atmosphere. In the navigation community, the delay in the neutral atmosphere is therefore usually just called the tropospheric delay. The contribution to the signal's delay by the water vapor – the so-called wet delay – makes up only about 10% of the total tropospheric (i.e., neutral-atmosphere) delay. However, due to the high temporal and local variability of the water vapor, this is the most crucial component for modeling and error correction. The troposphere is also the region where daily weather phenomena take place. In addition, in the lower troposphere clouds, rain, and fog exist. However, their influence on the amplitude and propagation velocity of the signals is negligible in the L band, where current and planned satellite navigation systems operate.

The sum of propagation delay and the path curvature results in an excess path measured by the receiver, compared to the true geometrical range. The excess path can be computed by integration of the refractive index along the curved path, s, through the atmosphere:

$$\Delta L = \int_S \left[n(s) - 1 \right] ds \cdot \qquad (1)$$

The excess path is often just called the delay, in meters. If not corrected, the excess path is equivalent to an error of the same amount in the range measurements. However, for the normal navigation user, the profile of the refractive index along the path, or even with height, is not known. Correction models are required, which do not require this information.

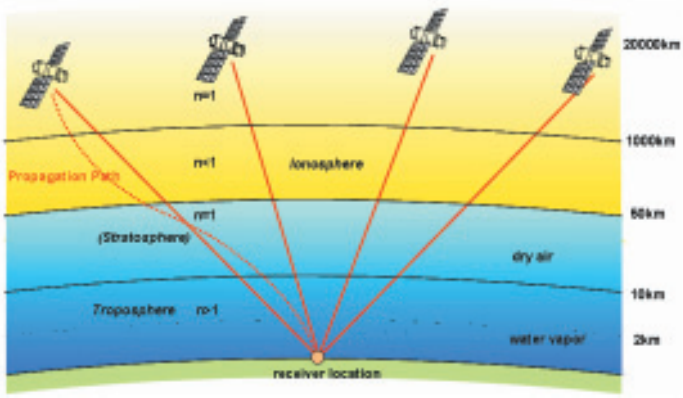

Figure 1. The structure of the atmosphere and its influence on the propagation path.

Frequency	$TEC = 10^{16}$ el/m^2	$TEC = 10^{18}$ el/m^2
100 MHz	40 m	4030 m
400 MHz	2.5 m	250 m
1200 MHz	0.28 m	28 m
1600 MHz	0.16 m	16 m
5000 MHz	0.016 m	1.6 m

Table 2. The ionospheric excess path.

3. Ionospheric Error

3.1 Total Electron Content and Ionospheric Delay

The ionosphere is characterized by ions and free electrons, which are created by UV and X-ray radiation from the sun. The ionosphere's state is therefore coupled to the 11-year cycle of solar activity, to day and night times, and to the season. The relevant layer that contains most of these particles extends between 80 and 1000 km above the Earth's surface. The key parameter for navigation is the total electron content (TEC), which is the integral of the total electron content in a column of 1 m^2 from the observation point to the satellite:

$$TEC = \int_{path} N_e dl \quad [\text{el/m}^2] \cdot \tag{2}$$

The ionospheric excess path is directly proportional to the TEC, and is inversely proportional to the square of the carrier frequency [2-4]:

$$\Delta L = \pm \frac{40.3}{f^2} \int_{path} N_e dl = \pm \frac{40.3}{f^2} TEC \cdot \tag{3}$$

The plus sign applies for the group delay, which is relevant for the code-phase measurements of the navigation signals. The minus sign applies for the phase delay, which is relevant for the carrier-phase measurements. The opposite sign of the code and carrier delays means that code and carrier diverge in the ionosphere. This is because the code is delayed, but the carrier phase is advanced.

Table 2 shows typical values of the ionospheric excess path, dependent on the carrier frequency for low and high TEC values. The vertical excess path normally lies between these values. The GPS, GLONASS, and Galileo frequencies are between 1200 and 1600 MHz.

3.2 Temporal and Regional Behavior

The TEC and, correspondingly, the ionospheric delay, depend on the 11-year cycle of solar activity; they reach maximum values every 11 years. The last solar maximum was in the year 2000. The amplitude of the ionospheric delay also depends on the season, where the highest values occur in winter (the winter anomaly).

The ionospheric delay is highest in the so-called crest region, which covers the latitudes between ±20° around the geomagnetic equator, and in polar regions [4].

3.3 Dual-Frequency Correction

If signals on two measurement frequencies are available, the TEC value or, directly, the ionospheric error at each of these frequencies, can be determined by measurement of their differential group delay: $\delta(\Delta t) = \Delta t_2(f_2) - \Delta t_1(f_1)$. By division by the speed of light, c, it follows from Equation (3) that

$$\delta(\Delta t) = \frac{40.3}{c} TEC \left(\frac{1}{f_2^2} - \frac{1}{f_1^2} \right)$$

$$= \Delta t_1 \frac{f_1^2 - f_2^2}{f_2^2}, \tag{4}$$

$$\Delta t_1 = \frac{f_2^2}{f_1^2 - f_2^2} \delta(\Delta t), \tag{5}$$

$$\Delta t_2 = \frac{f_1^2}{f_1^2 - f_2^2} \delta(\Delta t) \cdot \tag{6}$$

The dual-frequency measurements are affected by all other errors on the measurement path. As long as they do not cancel out in the difference, these errors are multiplied by the frequency ratio, $f_i^2 / \left(f_1^2 - f_2^2 \right)$ with $i = 1, 2$. Therefore, the two measurement frequencies should not be too close to each other. For instance, for dual-frequency corrections on GPS, $L_1 = 1.575$ GHz; with the help of the second frequency, $L_2 = 1.227$ GHz, the ratio is 1.54. The accuracy of the dual-frequency correction is limited by the receiver noise, and is of the order of 1 ns.

3.4 Single-Frequency Correction Model

Single-frequency users require a correction model that predicts the ionospheric error without measurement data. The most common model is the Klobuchar model [5, 6]. It models the daily behavior depending on the user's location, the year, day of the year, and hour of the day, t, with the help of eight coefficients that are transmitted in the GPS navigation message. The daily behavior of the ionospheric group delay, t_g, is modeled by a half-cosine function, with maximum amplitude at 14:00 o'clock local time:

$$t_g = F\left\{5 + A\cos\left[2\pi\left(t-14\right)/P\right]\right\}\,[\text{ns}]$$

$$\text{for } \left(t-14\right)/P < 1/4 \qquad (7)$$

At nighttime, with $\left(t-14\right)/P > 1/4$, the ionospheric group delay is set to a constant value of 5 ns. The amplitude, A, and period, P, of the cosine function depend on the user's location and date. F is the mapping function, which maps the vertical delay to the slant-path delay. P is the period of the day. The amplitude and period, P, are both approximated by polynomials of third degree, with the ionospheric sub-point as an input variable. This is the geomagnetic latitude, where the slant path from the user to the satellite crosses the ionospheric layer with the highest electron density at 350 km height. The coefficients of the polynomials are transmitted to the user in the GPS navigation message. The mapping function, F, is [6]

$$F = 1 + 2\left(\frac{96-E}{90}\right)^3, \qquad (8)$$

where E is the elevation angle of the satellite in degrees from the user's point of view.

The advantage of the Klobuchar model is that it is easy to implement, and requires only a few input parameters. However, the drawback is that its accuracy is only about 50%. The ionospheric error is therefore the dominant contribution in the error budget for single-frequency GPS users.

3.5 EGNOS and WAAS

One reason for the introduction of the American Wide-Area Augmentation System (WAAS) and the European Global-Navigation Overlay System (EGNOS) was the reduction of the ionospheric error for single-frequency GPS users. These systems derive the ionospheric error in a grid, from dual-frequency measurements in a regional ground-station network, and transmit differential corrections and integrity data via geostationary satellites. Because the information is distributed via satellites, these augmentation systems are also called satellite-based augmentation systems (SBAS). This is in contrast to local-area augmentation systems (LAAS), where local corrections and integrity data are transmitted from ground stations (GBAS), e.g., in the vicinity of an airport.

3.6 Doppler Shift

Temporal gradients of the TEC cause an additional Doppler shift, measured by the receiver:

$$\Delta f = \frac{dn}{dt} = \frac{40.3}{cf}\frac{dTEC}{dt}. \qquad (9)$$

An upper limit to the TEC rate for stationary users is 10^{15} el/m^2 per second. The corresponding frequency change is 0.085 Hz, and the velocity error (range-rate error) is 1.6 cm/s [4].

4. Tropospheric Error

4.1 Refractivity and Delay

Introducing the refractivity, $N = 10^6\left(n-1\right)$, where n is the refractive index, Equation (1) can be rewritten as

$$\Delta L = 10^{-6}\int_{S_{tropo}} N\left(s\right)ds\,, \qquad (10)$$

In this section, only the curved path, S_{tropo}, through the neutral atmosphere is considered, and ΔL is the tropospheric excess path.

The refractive index of the neutral atmosphere is [7]

$$N = 77.6\frac{P_d}{T} + 64.8\frac{P_w}{T} + 3.776\times10^5\frac{P_w}{T^2}$$

$$= N_d + N_w, \qquad (11)$$

where P_d is the partial pressure of dry air in hPa,, P_w is the partial pressure of water vapor in hPa, and T is the temperature in K. N can be separated into a dry part, N_d, depending on P_d and T, and a wet part, depending on P_w and T. Assuming that the air behaves as an ideal gas, N can alternatively be split into a hydrostatic component, depending only on the total air pressure, $P = P_d + P_w$, and a wet component, depending again on water vapor and temperature [8, 9]. Note that in both cases, the wet components are slightly different, because the hydrostatic component also contains a small fraction depending on water vapor.

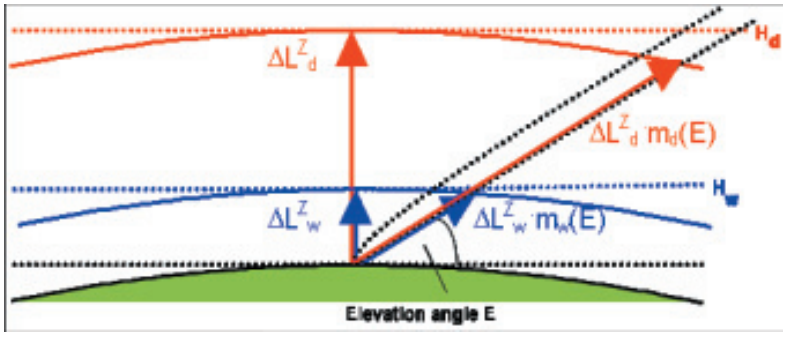

Figure 2. The calculation of the zenith delay and slant-path delay.

Common correction models do not apply Equation (10) directly, but calculate the tropospheric delay from measured or predicted values of the refractive index at the ground. For instance, the well-known Hopfield model [10] computes the dry and wet components of the zenith delay, L^Z, from the surface values of the dry and wet refractivity components, N_{ds} and N_{ws}, and two different scale heights, H_d and H_w. It then maps both components to the slant-path delay by multiplication with two mapping functions, $m_d(E)$ and $m_w(E)$, where E is the elevation angle of the path to the satellite (compare Figure 2):

$$\Delta L^Z = \Delta L_d^Z + \Delta L_w^Z$$

$$= \frac{10^{-6}}{5}\left(N_{ds}H_d + N_{ws}H_w\right), \qquad (12)$$

$$\Delta L(E) = \Delta L_d^Z m_d(E) + \Delta L_w^Z m_w(E). \qquad (13)$$

The wet-scale height is set to a constant value around 13000 m, and the dry scale height is computed from the temperature in K at the ground:

$$h_d = 148.98(T - 4.11). \qquad (14)$$

Most other models work in a similar manner. Models in a special class, made up of the so-called blind models, do not require estimated or measured meteorological input data. They compute the surface refractivity and the corresponding zenith delay depending on the user's location and the day of the year, using regression formulas derived from global statistics of surface refractivity based on pressure, water vapor, and temperature.

4.2 Regional and Temporal Behavior of Tropospheric Delay

Typical values of the total zenith tropospheric delay (ZTD) for a ground-based user at heights near mean sea level are about 2.3 to 2.5 m. Although the wet delay normally contributes only 5% to 15% to the total delay, the high temporal and spatial variability of the water vapor in the troposphere makes the wet delay the most crucial component, if accuracies in the decimeter or centimeter range are required.

Figures 3 and 4 show the variations of the total zenith delay for Milan and Hong Kong as a function of the day of the year, averaged over 10 years. These were derived from measured daily radiosonde profiles of temperature, pressure, and water-vapor content with Equations (10) and (11). For details of the radiosonde databank and data processing, see [11]. The curves show that there is a seasonal variation with

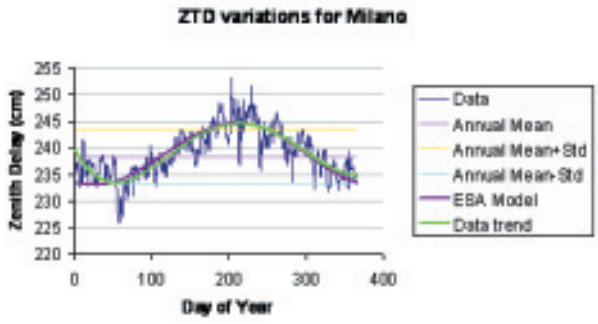

Figure 3. The 10-year average of total tropospheric zenith path delay as a function of the day of the year for Milan (Italy).

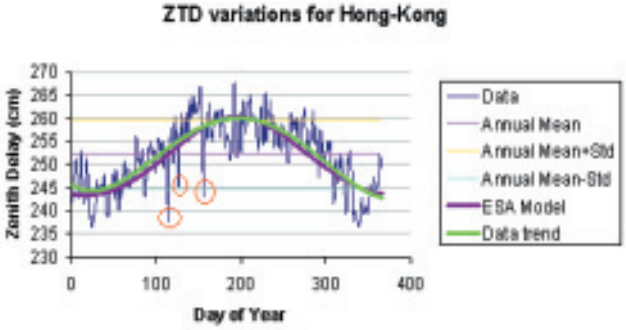

Figure 4. The 10-year average of total tropospheric zenith path delay as a function of the day of the year for Hong Kong. The red circles mark some exceptional spikes, which appear even in the 10-year average.

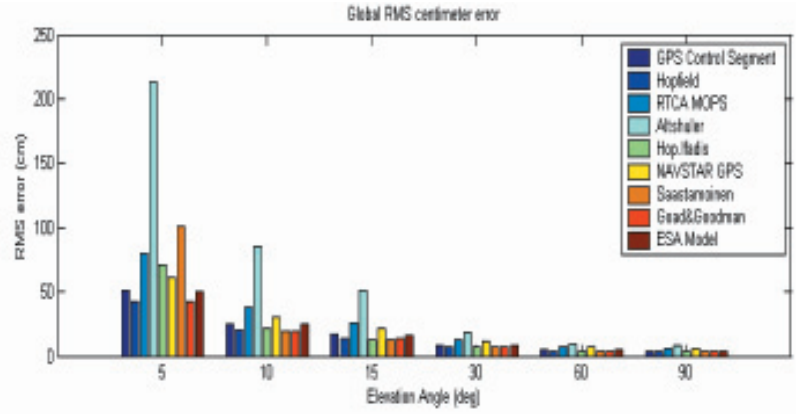

Figure 5. The rms error as a function of the elevation for different correction models: an average of 11 globally distributed stations, and 10 years of radiosonde data [23].

maximum in the summer and a minimum in the winter, but there is also a daily variation of about 5-10 cm around the mean trend. The seasonal dependence and the short time variations are both due mainly to the variation of the water-vapor content. Due to the high atmospheric water-vapor content in tropical areas, the zenith delay in these areas is highest. The figures also show the data trend by curve fitting with a polynomial, and a comparison with a model presented by ESA in [12].

4.3 Comparison of Correction Models

Figure 6 shows a comparison of the one-sigma residual error of the zenith path delay, calculated with different tropospheric correction models [10, 13-22]. The one-sigma error represents the error that is not exceeded for 68% of the time; in most cases, it is close to the rms error [23]. Again, reference data were the 10 years of radiosonde measurements from 11 globally distributed stations. The accuracy of the reference zenith path delay was of the order of 1 cm [11]. The figure provides results for non-blind models, where the measured surface values of temperature, air pressure, and water-vapor pressure have been used as input. It also provides results for blind models, which do not require such input data (see Section 4.1). In the global mean, the error for most models was about 3.5-4 cm, but there are locations were it exceeded 5 cm. It should be remembered here that the non-blind models provide this accuracy only if accurately measured meteorological input data are available: this is often not the case. Therefore, it is interesting to note that the ESA blind model [21, 22] performed nearly as well as the non-blind models. The RTCA-MOPS model [20] also was not significantly worse for most locations. For the NAVSTAR-GPS model [17] and the Altshuler model [18, 19], it could be observed that they failed for high altitudes such as Mexico City, which is approximately 2200 m above mean sea level.

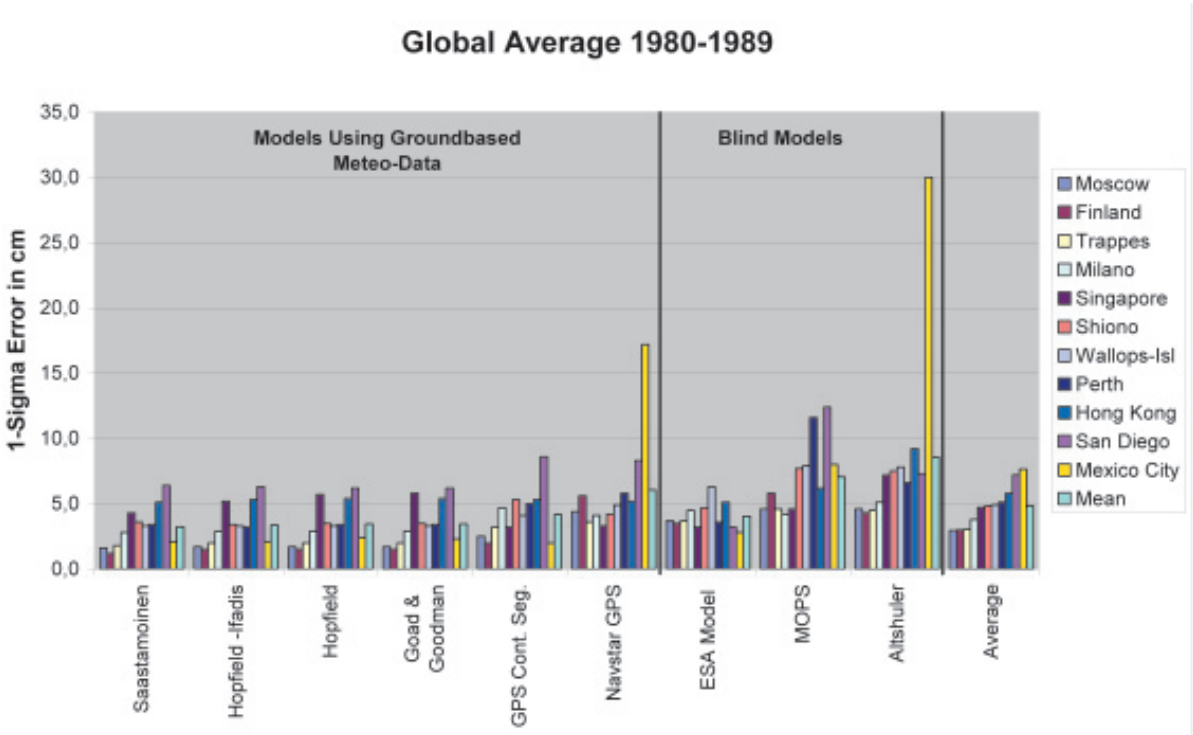

Figure 5. A comparison of one-sigma (68% confidence level) model performance for 11 globally distributed stations [23]

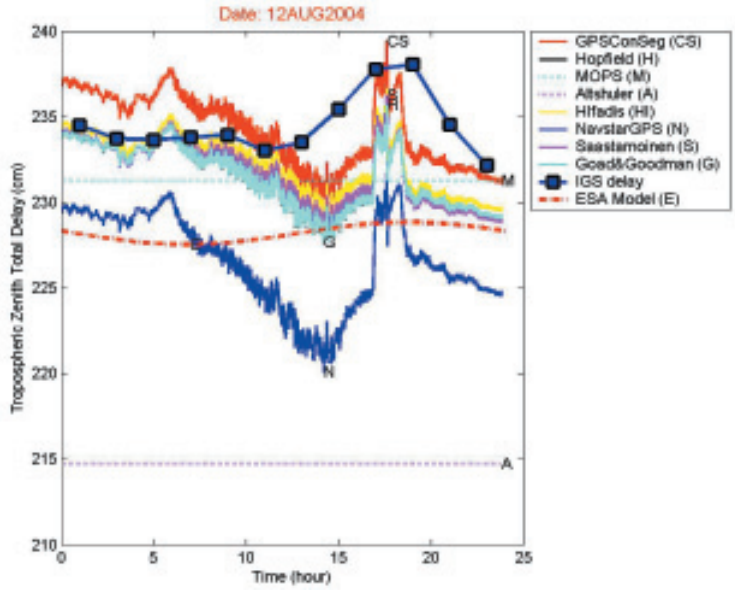

Figure 7. A comparison of the zenith delay computed with different tropospheric models during a thunderstorm's passage in Oberpfaffenhofen, Germany.

The error of the zenith path delay may appear to not be significant. However, it is multiplied with the mapping function for other elevation angles, and the mapping functions themselves can introduce an additional error for low elevation angles [24, 23]. Figure 5 provides the rms error of the different models as a function of the elevation angle. With the exception of one model, the different mapping functions showed more or less the same performance for elevation angles $>10°$, and the resulting error could be kept below 30 to 40 cm. However, for lower elevation angles, there were significant differences.

4.4 Local Events

In the previous sections, the long-time average error of the correction models has been considered. However, for real-time applications, the instantaneous error and the rate of change of the error count. In particular, the blind models cannot follow the actual weather behavior at the user's location, due to their pure statistical nature. Figure 7 shows an example of a local event recorded in Oberpfaffenhofen, Germany. For this event, rapid changes of temperature, humidity, and air pressure occurred during a thunderstorm front that passed the measurement site, e.g., the temperature dropped down from 32° to 14°, and the air pressure fell by 9 hPa, during the hours before the event, and reached their original values after the event had passed. Accordingly, the tropospheric zenith delay predicted by the models using recorded data from ground-based meteorological sensors changed by about 10 cm within some hours, and was raised by about 5 cm within less than an hour. When compared with reference zenith delays from the IGS network – which were computed by the post-processing of GPS measurements, which were also recorded in Oberpfaffenhofen, close to the site of the meteorological sensors – it was obvious that there were significant differences, even for the non-blind real-time models. The IGS results were considered to be accurate to of the order of 0.5 cm [25]. It seems that the change of delay was over-predicted by the non-blind models. In [11, 23], a number of such events in Oberpfaffenhofen were analyzed. It was found that maximum model errors of eight to 10 cm occurred for both blind and non-blind models. Also, during event periods, the non-blind models performed only slightly better than the blind models.

5. Scintillations

Scintillations are fast fluctuations of signal amplitude and phase due to atmospheric turbulence. They occur irregularly and are difficult to predict in advance. The main part of the frequency spectrum of these fluctuations lies between 1 Hz to 10 Hz. Scintillations occur both due to ionospheric sources, i.e., fast TEC variations, or due to tropospheric sources, here mainly due to water-vapor fluctuations or clouds. Tropospheric scintillations are only significant for low elevation angles, where the amplitude scintillations are mainly of concern. For instance, they can reach 2.5 dB for 0.01% of the time in tropical areas for an elevation angle of 5°, according to the model in [26]. The rms ranging error due to tropospheric phase fluctuations is below 1 cm for elevation angles above 5° [27].

Ionospheric scintillations are more critical: both amplitude and phase scintillation can reach significant values. In tropical areas, amplitude scintillation can cause signal fades of more than 20 dB so that the signals are completely lost by the receiver. In polar and auroral regions, amplitude scintillations due to geomagnetic storms can reach amplitudes around 10 dB, but scintillation events there can last several hours or even days. Phase scintillations occur mainly in tropical areas, but can also appear in mid-latitudes during major magnetic storms. They lead to cycle slips, which are critical for carrier-phase navigation. They can also lead to random phase fluctuations that exceed the narrow bandwidth (typically around 1 Hz) of the receiver's phase-locked loop (PLL), so that the receiver loses phase lock [4]. Similarly to the regular ionospheric delay error,

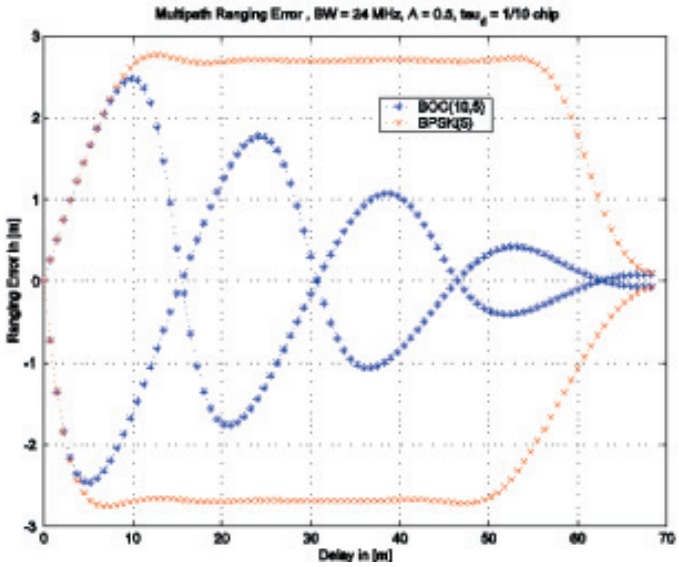

Figure 8. The multipath error envelope. The figure shows the envelope of the resulting ranging error derived from receiver simulations for one multipath signal with half the amplitude of the line-of-sight signal as a function of the delay of the echo. The receiver bandwidth was 24 MHz, and the correlator spacing was 0.1 code chip. Red: BPSK signal with 5 MHz chip rate; blue: BOC-signal with 5×1.023 chip rate and 10×1.023 MHz subcarrier modulation [31].

ionospheric scintillations depend on the solar activity, and are strongest in tropical and polar regions.

6. Shadowing

Signal attenuations due to atmospheric gases, clouds, and rain are negligible in the L band. However, navigation signals can easily be attenuated by vegetation and walls, or can be completely shadowed by buildings and other obstacles. The specific attenuation for woodlands at 1.6 GHz (circa GPS L_1) is about 0.3 dB/m [28]. Some values for attenuation by walls are given in Table 3. Attenuation by walls is a particular problem for indoor navigation. However, methods have been developed to enhance the sensitivity of receivers by advanced signal processing. Indoor navigation can also be assisted by other means, e.g., by the sending of a priori information via mobile communication links to the navigation receivers, or by aiding with other sensors.

7. Multipath

Signals that are reflected by the ground, buildings, or other obstacles, and superimpose with the direct signal at the user's antenna, disturb the correlation function and reduce the ranging accuracy. The error depends on the amplitude, phase, and the delay of the echo relative to the line-of-sight signal.

Figure 8 shows the error envelopes for a BPSK and a binary offset carrier signal (BOC), when one multipath signal with half the amplitude of the line-of-sight signal is superimposed with the line-of-sight signal. The envelopes represent the maximum error that occurs when the multipath signal is in phase or in opposite phase (180°) with respect to the line-of-sight signal. For all other phases, the error lies between the envelopes. The figure also illustrates that binary offset carrier signals are more robust against multipath propagation than are BPSK signals.

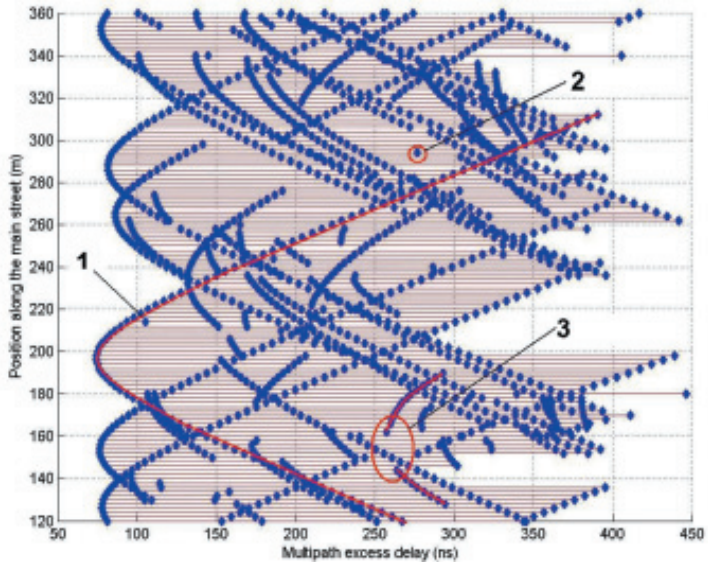

Figure 9. Simulated multipath echoes for a car driving through an urban environment. The y axis shows the position of the car in the main street of Figure 10, while the x axis shows the delay of the echoes relative to the line-of-sight signal. The echoes are represented by blue symbols. The red marks highlight echoes with long (1), very short (2), and short (3) lifetimes [32].

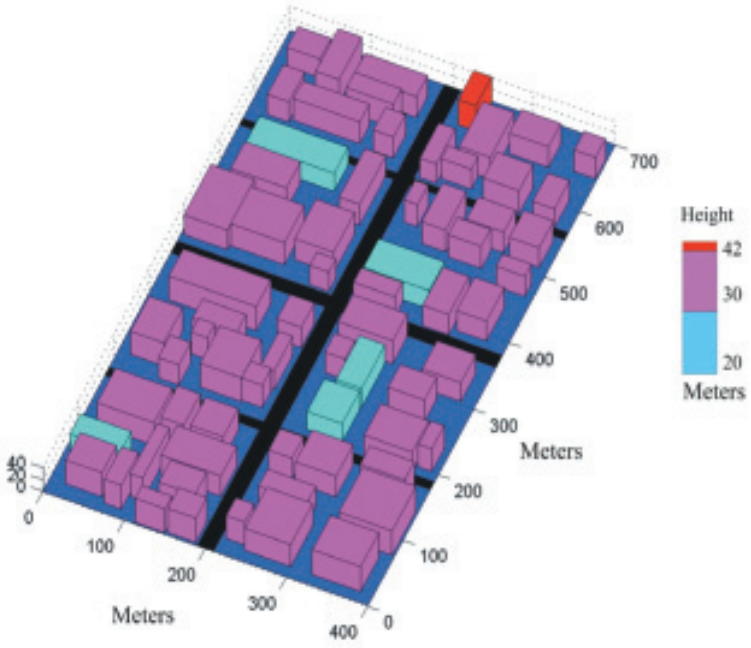

Figure 10. The synthetic urban environment used in Figure 8. The heights and distribution of buildings were simulated based on probability density functions. The car drove along the main street [32].

In real environments, several multipath signals are normally simultaneously present. Figure 9 shows a simulation of the development of multipath signals for a car that drives through the synthetic urban environment illustrated in Figure 10. Some echoes exist for a relatively long time, whereas others have only a short or very short lifetime.

8. Conclusion

In satellite navigation, the modeling and correction of the additional delay due to the propagation through the atmosphere, and errors due to further propagation phenomena, play an important role for the accuracy of the derived position solution. The largest additional signal delay occurs within the ionosphere. Because the ionospheric delay depends on frequency, it can be precisely determined and nearly completed eliminated by dual-frequency measurements. However, for single-frequency receivers – such as most commercially available mass-market GPS receivers – the ionospheric delay must be corrected by modeling, and a significant error can remain.

The tropospheric delay can be separated into a wet component, due to water vapor, and a dry component, due to other atmospheric gases. While the dry delay can be modeled with high accuracy, the wet delay is a crucial component if accuracies in the decimeter or centimeter range are required. This is because of the high temporal and spatial variability of the water-vapor content in the troposphere, although it normally contributes only 5% to 15% of the total delay.

Since current global navigation satellite systems, such as GPS, GLONASS, and the coming Galileo, operate in the L band, attenuation by the atmosphere is negligible. This may change for next-generation systems if additional higher-frequency bands are utilized, e.g., C band, which is already allocated for Galileo. However, in L-band fast amplitude and phase scintillations can also occasionally occur, due to fast variations of the total electron content in the ionospheric or tropospheric turbulence. Strong scintillations occur only rarely, but then they are critical, and can even lead to complete loss of the navigation signals by the receiver.

Due to the extremely low signal power of the satellite navigation signals when arriving at the Earth, the signals can be easily attenuated and shadowed by buildings or vegetation, e.g., in urban or rural environments or in indoor applications. Additionally, in these environments multipath propagation due to reflections of the signals from the ground, buildings, and other obstacles before they arrive at the user antenna can significantly degrade the ranging and positioning accuracy. Multipath propagation is difficult to correct with models, because it depends strongly on the local user's environment. Different techniques exist to mitigate the effect of multipath signals as far as possible, either by advanced signal processing in the receiver, or by specially designed antennas. However, multipath mitigation is still a hot topic for research.

9. References

1. B. W. Parkinson, "GPS Error Analysis," in B. W. Parkinson and J. J. Spilker, Jr. (eds.), *Global Positioning System, Theory and Applications, Volume I*, Washington, DC, American Institute of Astronautics and Aeronautics, 1996.

2. B. Hoffman-Wellenhof, H. Lichtenberger, and J. Collins, *Global Positioning System, Theory and Practice, Fourth Edition*, New York, Springer, *1997.*

3. A. Leick, *GPS Satellite Surveying*, New York, John Wiley and Sons, 1989.

4. J. A. Klobuchar, "Ionospheric Effects on GPS," in B. W. Parkinson and J. J. Spilker, Jr. (eds.), *Global Positioning System, Theory and Applications, Volume I*, Washington, DC, American Institute of Astronautics and Aeronautics, 1996.

5. J. A. Klobuchar, "Ionospheric Time-Delay Algorithm for Single-Frequency GPS Users," *IEEE Transactions on Aerospace and Electronic Systems*, **AES-23**, 3, May 1987, pp. 325-331.

6. ICD-GPS 200c, NAVSTAR GPS Space Segment/ Navigation User Interfaces, ARINC Research Corporation.

7. G. D. Thayer, "An Improved Equation of Refractive Index of Air," *Radio Science*, **9**, 1994, pp. 803-807.

8. V. B. Mendes and R. B. Langley, "Tropospheric Zenith Delay Prediction Accuracy for High-Precision GPS Positioning and Navigation," *Journal of the Institute of Navigation*, **46**, 1, 1999, pp. 25-34.

9. J. J. Spilker, Jr., "Tropospheric Effects on GPS," in B. W. Parkinson and J. J. Spilker, Jr. (eds.), *Global Positioning System, Theory and Applications, Volume I*, Washington, DC, American Institute of Astronautics and Aeronautics, 1996, pp. 517-546.

10. H. S. Hopfield, "Two Quadratic Tropospheric Refractivity Profile for Correcting Satellite Data," *Journal of Geophysical Research*, **74**, 18, August 20, 1969, pp. 4487-4499.

11. A. Hornbostel and M. M. Hoque, "Tropospheric Correction Models for Local Events," Proceedings of the European Navigation Conf. GNSS 2004, Rotterdam, May 16-19, 2004.

12. *Galileo Reference Troposphere Description of Models*, Issue 1, Rev. 0, March 25, 2002, ESA-APPNG_SPEC/00165-AM.

13. J. Saastamoinen, "Contributions to the Theory of Atmospheric Refraction," *Bulletin Geodesique*, 1973, **105**, pp. 279-298; **106**, pp. 383-397; **107**, pp. 13-14.

14. H. D. Black, "An Easily Implemented Algorithm for the Tropospheric Range Correction," *Journal of Geophysical Research*, **83**, B4, April 10, 1978, pp. 1825-1828.

15. I. Ifadis, "The Atmospheric Delay of Radio Waves, Modeling the Elevation Dependence on a Global Scale," Technical Report No. 38L, School of Electrical and Computer Engineering, Chalmers University of Technology, Göteborg, Sweden 1986.

16. C. C. Goad and L. Goodman, "A Modified Hopfield Tropospheric Refraction Correction Model," AGU Annual Fall Meeting, San Francisco, 1974.

17. "Technical Characteristics of the NAVSTAR GPS," NATO + NAVSTAR Technical Support Group, 1991.

18. E. E. Altshuler and P. M. Kalaghan, "Tropospheric Range Error Corrections for the NAVSTAR System," AFCRL-TR-74-0198, April 1974.

19. E. E. Altshuler, "Tropospheric Range-Error Correction for the Global Positioning System," *IEEE Transactions on Antennas and Propagation*, **AP-46**, 5, May 1998, pp. 643-649.

20. "Minimum Operational Standard for Global Positioning/Wide Area Augmentation System Airborne Equipment," RTCA/DO-229A, June 8, 1998.

21. *GALILEO Reference Troposphere Model for the User Receiver*, Issue 2, ESA, July 10, 2003.

22. ESA Blind Model 2.3 issued on 28/01/2004 (*MATLAB* Code).

23. A. Hornbostel and M. M. Hoque, "Analysis of Tropospheric Correction Models for Local Events within the GSTB Test Case APAF," Proceedings of ION-GNSS 2004, Institute of Navigation, September 2004.

24. A. Hornbostel, "Simulation of Tropospheric Effects for Satellite Navigation," Proceedings of the European Telemetry Conference, Garmisch, May 2000.

25. http://igscb.jpl.nasa.gov/components/prods.html

26. "Propagation Data and Prediction Methods Required for the Design of Earth-Space Telecommunication Systems," ITU-R Rec. 618-4, 1994.

27. G. H. Millman, "Tropospheric Effects on Space Communications," Proceedings of the Conference on Tropospheric Radio Wave Propagation, Part 1, AGARD Conference Proc. No. 70, pp. 4-1 - 4-29, 1970.

28. "Attenuation in Vegetation," ITU-R Rec. 833-2.

29. W.C. Stone, "Electromagnetic Signal Attenuation in Construction Materials," NIST Report 605, National Institute of Standards, Gaithersburg, Maryland, 1997.

30. B. Eissfeller, A. Teuber, and P. Zucker, "Untersuchungen zum Satellitenempfang in Gebäuden," *Allgemeine Vermessungsnachrichten*, 4/2005, pp. 137-145. Herbert Wichmann Verlag, Heidelberg, 2005.

31. H. Denks, "Übersicht über die geplanten Signale bei Galileo mit Schwerpunkt BOC-Signale," Technical Note, GalileoNAV-3100-1, Revision 1.2, DLR Institute of Communications and Navigation, 2003.

32. O. Esbri-Rodriguez, A. Konovaltsev, and A. Hornbostel, "Modeling of the GNSS Directional Radio Channel in Urban Areas Based on Synthetic Environments," Proceedings ION National Technical Meeting, San Diego, January 26-28, 2004.

Ultra-Wideband Communications : An Overview

A. F. Molisch

Abstract

This paper presents an overview of ultra-wideband (UWB) communications systems, i.e., systems with very large relative and/or absolute bandwidth. The large bandwidth and low power spectral density mandated for UWB systems allows their use as overlays over existing (legacy) systems, i.e., they can be used in the same frequency range as existing systems without causing undue interference. We also describe the most common types of UWB systems, including time-hopping impulse radio, frequency hopping, and multi-band OFDM. We furthermore discuss interference aspects and the peculiarities of UWB propagation channels.

1. Introduction

Ultra-wideband (UWB) communications systems are commonly defined as systems with large absolute and/or large relative bandwidth. Such a large bandwidth offers specific advantages with respect to signal robustness, information transfer speed, and/or implementation simplicity. However, it also leads to fundamental differences from conventional, narrowband, systems. The past years have seen a confluence of technological and political/economic circumstances that enabled the practical use of UWB systems. Consequently, interest in UWB has grown dramatically. The current paper gives a very brief synopsis of the state of the art. More details and additional references can be found in [1-4].

UWB is a technology that dates back to the 19th century. At that time, the easiest way of generating an electromagnetic signal was to generate a short pulse. The spark-gap generators used by Hertz and Marconi can thus be considered to be the first practical UWB systems. Around the same time, theoretical research into the propagation of UWB radiation started when Sommerfeld analyzed the diffraction of a short pulse by a half-plane. However, in subsequent years the general interest turned to narrowband communications. Part of the reason was the fact that the spectral efficiency of the signals generated by the spark-gap transmitters was low: the signals that were generated had a low bit rate, but occupied a large bandwidth. In other words, they had a large spreading factor (the ratio between the used bandwidth and the data rate). At that time, it was not know how to provide multiple-access capability with such widely-spread signals. This problem was solved by the introduction of time-hopping impulse radio (TH-IR) in the early 1990s, where the pioneering work of Win and Scholtz [5-7] showed that impulse radio could sustain a large number of users by assigning pseudorandom transmission times to the pulses from the different users. This insight, coupled with advances in electronics-device design, spawned the interest of commercial wireless companies in UWB.

The attractiveness of UWB systems stems mainly from the fact that they can be used as an overlay to existing systems. In other words, they do not require new spectrum, but can be operated in parallel with existing, legacy systems. This can be understood from the following simple picture (Figure 1): the transmitted power of any system can be

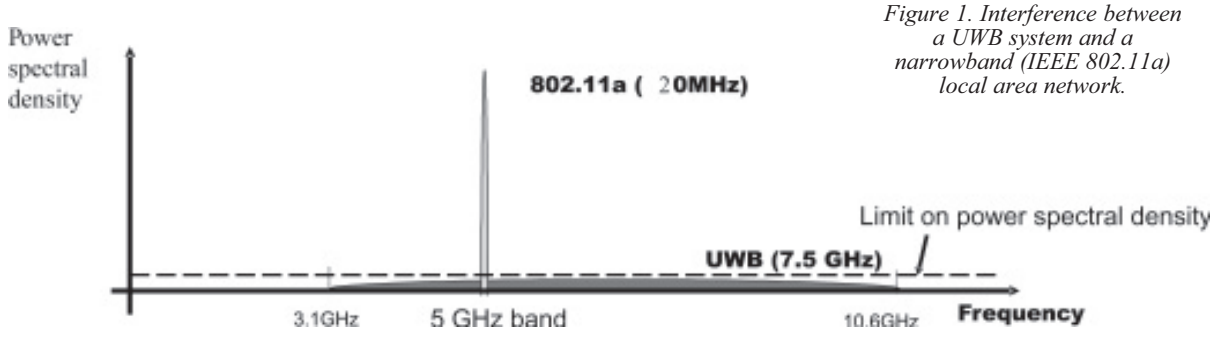

Figure 1. Interference between a UWB system and a narrowband (IEEE 802.11a) local area network.

Andreas F. Molisch is with the Department of Electrical Engineering, University of Southern California, Los Angeles, CA, USA; E-mail: Andreas.Molisch@ieee.org.

This is one of the invited papers from the Forum on Radio Science and Telecommunications, held at the XXIX General Assembly of URSI, August 15, 2008, Chicago, Illinois.

(approximately) expressed as the product of the power spectral density (PSD) and the bandwidth. A large (absolute) bandwidth thus enables a system with reasonable transmitted power to exhibit an extremely low power spectral density. A victim (narrowband) receiver will see only the noise power within its own system bandwidth, which is only a fraction of the UWB bandwidth. Due to this small interference, frequency regulators all over the world have allowed intentional UWB emissions in the microwave regime, subject to certain restrictions for the emission power spectrum, as discussed in Section 2.

The large absolute bandwidth allows transmission of extremely high data rates (> 100 Mbit/s), although the transmission can be achieved only over relatively short distances (< 10 m) because only very low power is available for each bit. Alternatively, low-data-rate communication (e.g., < 1 Mbit/s) is possible over much larger distances by exploiting the large spreading factor. Besides enabling large data rates or spreading factors, a large absolute bandwidth also has a number of other important benefits:

- It enables very fine resolution for ranging, which is useful for radar and geolocation applications [8]; and
- It introduces a high degree of frequency diversity [9] and decreases the fading depth of resolvable multipath components [10]. This results in a robustness to small-scale fading that is significantly better than that of conventional narrowband systems.

At the same time, a large absolute bandwidth makes it more difficult to build effective transceivers. Accurate timing, as well as a high sampling rate and a subsequently high computational effort for the processing of the samples, are usually required. As a consequence, many papers deal with the design of efficient and/or simplified transceiver structures that allow exploitation of the benefits of high absolute bandwidth at reduced computational cost (for details, see Section 4).

A large *relative* bandwidth also offers advantages for UWB systems, in particular a greater robustness of the

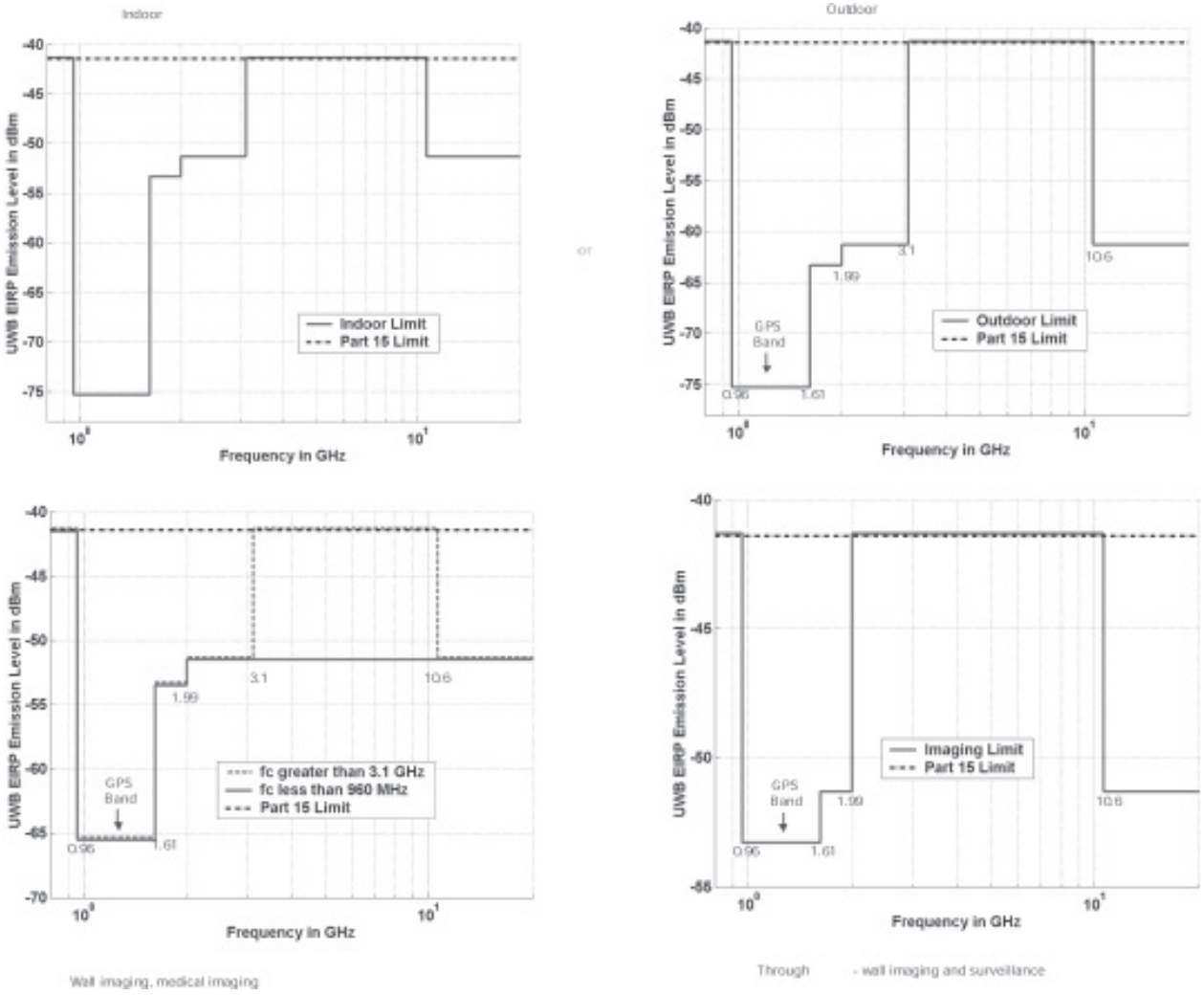

Figure 2. FCC masks for different environments [11].

signals to shadowing. Intuitively, the different frequency components of the signal "see" different propagation conditions. There thus is a high probability that at least some of them make their way from the transmitter to the receiver. The low-frequency components can more easily penetrate walls and ground, while the high-frequency components are effectively reflected, and can thus propagate on zigzag routes to the receiver. Consequently, the signal is more robust to shadowing effects. On the other hand, building UWB transceivers with a large relative bandwidth is especially difficult. In particular, building amplifiers and antennas with more than 10% relative bandwidth is difficult, both due to practical reasons and because of theoretical limitations (the Fano bound).

The remainder of this paper is organized in the following way: Section 2 discusses the frequency regulations for UWB, as well as interference to and from narrowband systems. Section 3 describes the aspects of electromagnetic propagation that are unique to UWB systems, and in particular channel models that are in use for UWB systems. Section 4 investigates various modulation and multiple-access methods that employ UWB signaling. Section 5 gives an overview of UWB applications and the international standards that enable those applications. A summary and conclusions wrap up the paper.

2. Frequency Regulations and Interference Aspects

As discussed in the Introduction, the interference to legacy systems is determined by the power spectral density of the UWB radiation as seen by the victim device. Assuming that propagation loss cannot be influenced by frequency regulators (it is determined by the distance between the UWB transmitter (TX) and victim receiver (RX), as well as the environment), frequency regulators can only impose limits on the power spectral density (PSD) emitted by a UWB transmitter. Those limits (also known as the frequency mask) can be frequency dependent, since some victim devices might be more worthy of special protection than others.

In the US, the frequency masks depend on the application, and the environment in which the devices are operated. For indoor communications, a power spectral density of −41.3 dBm/MHz is allowed in the frequency band between 3.1 and 10.6 GHz. Outside of that band, no intentional emissions are allowed, and the admissible power spectral density for spurious emissions provides special protection for GPS and cellular services (see Figure 2). For outdoor environments, only mobile, battery-operated transmitters are allowed. Again, intentional emissions are allowed in the 3.1-10.6 GHz range; the mask for spurious emissions is different from the indoor case. Further masks are defined for wall imaging systems and ground-penetrating radar. The frequency range from 24-29 GHz is allowed for vehicular radar systems.

The rules of European and Japanese frequency regulators are stricter. In the frequency range between 3.4 and 4.8 GHz, operation requires a "detect-and-avoid" mechanism, i.e., a UWB device must determine whether there are narrowband (victim) receivers in the surroundings, and avoid emissions in the frequency range of those victim devices. Additionally, Europe allows operation between 4.2 and 4.8 GHz without detect-and-avoid until the year 2010. In the higher frequency range (6-8.5 GHz in Europe, 7.25-10.25 GHz in Japan), operation is allowed without detect and avoid, with a power spectral density limit of −41.3 dBm/MHz.

There has been considerable concern whether the protection of legacy systems by the frequency masks is sufficient. The FCC (the US frequency regulator) established the mask by making the limits on *deliberate* UWB emissions identical to limits on *involuntary* (spurious) emissions from any electric device. There still is a concern that widespread use of UWB devices might lead to high aggregate interference, which could negatively impact operation of legacy systems. Recent work indicates that the interferer closest to the victim device dominates the overall performance [12]. However, any such analysis is critically influenced by assumptions about the path-loss exponent, as well as the spatial distribution of emitters. If the interferer and the victim device are in extremely close proximity, very strong interference is unavoidable. There is thus no general consensus about the practical importance of interference from UWB devices with victim (legacy) devices.

It is noteworthy that frequency regulations only consider the interference of UWB devices with narrowband devices. The reverse case, namely the narrowband interference with a UWB device, is not regulated. Rather, it is the task of UWB transceivers to withstand narrowband interference as well as possible.

3. Propagation Channels

Ultra-wideband propagation channels differ from narrowband propagation channels in several key respects (see [13-15] for more discussion and extensive references). Again, it is useful to distinguish between channels with large relative bandwidths and those with large absolute bandwidths. In channels with large relative bandwidth (BW), we find that

- Each multipath component (MPC) suffers from distortion, so that the channel impulse response can *not* be written as a sum of weighted and delayed delta pulses; as a consequence, the WSSUS (wide-sense stationary uncorrelated scattering) assumption is not valid, anymore.

- The path loss and shadowing become a function of the frequency at which they are considered.

- Similarly, angular spreading can become frequency dependent.

Challenges for the design of antennas are also related to these properties: building antennas with bandwidths larger than 10% is challenging [16]. Furthermore, the shape of the antenna pattern changes with frequency, which increases the peak EIRP (effective isotropic radiated power) and makes computation of antenna gains in beamforming designs more difficult.

Channels with large absolute bandwidth show the following key characteristics:

- The amplitude fading statistics of resolvable delay bins are not necessarily Rayleigh;
- Impulse responses can become "sparse," i.e., resolvable multipath components are separated (in the delay domain) by delay regions that do not contain any significant energy contribution.
- Impulse responses show a "soft onset," i.e., the main energy does not arrive (even on average) at the smallest delay.

In the following, we elaborate more on those aspects.

3.1 Large Relative Bandwidth

3.1.1 Fundamental Form of the Impulse Response

The impulse response of a UWB propagation channel can be written as a sum of *distorted* discrete multipath components (MPCs):

$$h(t,\tau)=\sum_{i=1}^{N} a_i(t)\chi_i(t,\tau)\otimes\delta(\tau-\tau_i), \qquad (1)$$

where N is the number of multipath components and the $a_i(t)$ are the (complex) amplitudes of the multipath components. The phases of the $a_i(t)$ vary quickly with time (or location of the MS), while $|a_i(t)|$ and τ_i vary slowly. The function $\chi_i(t,\tau)$ denotes the (time-varying) distortion of the ith multipath component due to the frequency selectivity of the interactions with the environment. Note that the presence of $\chi_i(t,\tau)$ is the distinguishing property of UWB channels: for $\chi_i(t,\tau)=const$, the conventional narrowband model is recovered [17].

3.1.2 Frequency Dependence of Path Loss

It follows from elementary Fourier theory that the pulse distortions in the time domain lead to a frequency dependence of the channel parameters in a transfer-function representation. In particular, the path loss becomes frequency dependent. In a narrowband channel, the path loss is defined as

$$PL=\frac{E\{P_{RX}\}}{P_{TX}}=E\left\{\left|H(f_c)\right|^2\right\}, \qquad (2)$$

where P_{TX} and P_{RX} are the transmitted and received power, respectively; f_c is the center frequency; and the expectation $E\{\ \}$ is taken over an area that is large enough to allow averaging out of the shadowing as well as the small-scale fading: $E\{\ \}=E_{lsf}\{E_{ssf}\}$. A wideband path loss has been proposed in references [18, 19] as

$$PL=E\left\{\int\left|H(f)\right|^2 df\right\}, \qquad (3)$$

where the integration is over the bandwidth of interest; it is assumed implicitly that this bandwidth is much smaller than the center frequency. In a conventional wireless system, any frequency selectivity of the transfer function stems from the multipath propagation, and is thus related to the small-scale fading. Integration over the frequency and expectation $E_{ssf}\{\ \}$ thus essentially have the same effect, namely averaging out the small-scale fading.

On the other hand, in a UWB channel we have to define a frequency-dependent path loss,

$$PL(f)=E\left\{\int_{f-\Delta f/2}^{f+\Delta f/2}\left|H(\tilde{f})\right|^2 d\tilde{f}\right\}, \qquad (4)$$

where Δf is chosen small enough so that diffraction coefficients, dielectric constants, etc., can be considered constant within that bandwidth. The *total* path loss is obtained by integrating over the whole bandwidth of interest.

The path gain dependence on the frequency is commonly modeled as being proportional to $f^{-2\kappa}$ [20], where $\kappa=1$ corresponds to the standard Friijs' law. Measured coefficients for κ range from negative values [21] to 1.4.

Naturally, the path loss also depends on the distance. Path loss modeling can be simplified by assuming that the frequency dependence and the distance dependence can be treated independently of each other:

$$PL(f,d)=PL(f)PL(d)\cdot \qquad (5)$$

The distance dependence is usually modeled as a power decay law:

$$PL(d)=PL(1\,\mathrm{m})\left(\frac{d}{1\,\mathrm{m}}\right)^{-n}, \qquad (6)$$

where n is the path-loss exponent. Note that this model is no different from the most common narrowband channel models. The many results available in the literature for this case can thus be reused. The path loss exponent does *not* show a frequency dependence, according to some recent measurements [22].

3.2 Large Absolute Bandwidth

For a large absolute bandwidth, the arrival times and the fading statistics of the multipath components are essential.

3.2.1 Clustering

It has been observed in many measurements that the multipath components arrive in clusters. The most popular model reflecting this structure is the Saleh-Valenzuela (SV) model [23]:

$$h_{SV}(t,\tau) = \sum_{l=0}^{L}\sum_{k=0}^{K} a_{k,l}(t)\,\delta\left(\tau - T_l - \tau_{k,l}\right), \qquad (7)$$

where $a_{k,l}$ is the tap weight of the kth component in the lth cluster, T_l is the delay of the lth cluster, and $\tau_{k,l}$ is the delay of the kth multipath component relative to the lth cluster arrival time T_l . K is the number of multipath components within a cluster, and L is the number of clusters. Within each cluster, the inter-arrival times of the paths is a Poisson process. Due to the high resolution in UWB systems, the random arrival time results in a "sparse" channel model, where there can be one or more resolvable delay bins, with little energy between two adjacent taps carrying significant multipath components.

The average power of the multipath components within a cluster is an exponentially decreasing function of delay:

$$E\left\{\left|a_{k,l}\right|^2\right\} \propto \Omega_l \exp\left(-\tau_{k,l}/\gamma_l\right) \text{ for } \tau_{k,l} \geq 0, \qquad (8)$$

where Ω_l is the integrated energy of the lth cluster, and γ_l is the intra-cluster-decay time constant. The cluster powers, averaged over the large-scale fading, in general follow an exponential decay

$$10\log(\Omega_l) = 10\log\left[\exp\left(-T_l/\Gamma\right)\right]. \qquad (9)$$

However, in a number of non-line-of-sight (NLOS) environments, a different delay dependence of the power (first increasing, and then decreasing) has been observed [21]. This is known as "soft onset," and has an important impact on ranging performance.

3.2.2 Small-Scale Fading

Since only few multipath components fall into one resolvable delay bin, the small-scale fading statistics are different from the narrowband case. The most frequently observed distribution for the small-scale fading is the *Nakagami distribution* (e.g., [24]),

$$pdf(x) = \frac{2}{\Gamma(m)}\left(\frac{m}{\Omega}\right)^m x^{2m-1}\exp\left(-\frac{m}{\Omega}x^2\right), \qquad (10)$$

where $m \geq 1/2$ is the Nakagami m-factor, $\Gamma(m)$ is the gamma function, and Ω is the mean-square value of the amplitude. Furthermore, the Rice distribution [25] and the lognormal distribution [26] have also been found to be good fits to experimental data.

3.3 Standardized Channel Models

Two channel models have been standardized for the evaluation of UWB communications systems. The earlier IEEE 802.15.3a model was developed to compare standardization proposals for high-data-rate wireless PANs (personal-area networks). Due to this purpose, the environments considered were office and residential indoor scenarios with a range of less than 10 m. The model is based on a relatively small number of measurements. It was described in [27].

The IEEE 802.15.4a channel model was developed for low-rate communications applications that have a larger range and are to be used in a multitude of different environments. Consequently, the model is parameterized for more environments. In addition, it was decided to take into account several effects that were neglected in the 15.3a models. A detailed description can be found in [21].

However, it must be stressed that the channel models are not restricted to particular data rates.

4. Modulation and Multiple Access

Signals with extremely large bandwidth can be created by a variety of methods. Most prominent among these is time-hopping impulse radio (TH-IR), a technique that was pioneered by Win and Scholtz [5-7]. By operating with short pulses, it enables very simple and cost-effective transmitter structures. Other notable techniques include frequency-hopping, OFDM (orthogonal frequency-division multiplexing), direct-sequence CDMA (code-division multiple access), and combinations of the above techniques. For all of these spreading methods, it is necessary to enable efficient multiple access, i.e., enabling multiple UWB

transmissions (and their reception by the intended receivers) simultaneously, within the same frequency band.

4.1 Impulse Radio

Communication by transmitting short pulses has many attractive properties, such as enabling extremely simple transmitters. However, a key question is how to ensure reasonable spectral efficiency. At first glance, it seems that with impulse radio, only a small number of users could be "on air" simultaneously. Consider the case where one pulse per symbol is transmitted. Since the UWB transceivers are unsynchronized, so-called "catastrophic collisions" can occur, where pulses from several transmitters arrive simultaneously at the receiver. The signal-to-interference ratio then becomes very bad, leading to a high bit-error probability (BER, or bit error rate).

Time-hopping impulse radio (TH-IR) [7] avoids catastrophic collisions by representing each data bit by *several* short pulses. The possible positions of the pulses within a symbol follow certain rules. The symbol duration is subdivided into N_f "frames" of equal length. Within each frame, the pulse can occupy an almost arbitrary position, which is determined by the time-hopping code. Typically, the frame is subdivided into "chips," the length of which is equal to a pulse duration. The (digital) time-hopping code now determines which of the possible chips the pulse actually occupies, and the time-hopping code is different for each user. Even if one pulse within a symbol collides with a signal component from another user, other pulses in the sequence will not (see Figure 3). In other words, collisions can still occur, but they are not catastrophic anymore.

In addition to using pseudorandom *delays* of the pulses, it is also advantageous to assign pseudorandom *polarities* for each pulse [28]. This process avoids the spectral lines that are normally contained in the spectrum of a signal where all the transmitted pulses have the same polarity (as shown in Figure 3). Such spectral smoothing is important, because most frequency regulators prescribe a maximum power spectral *density* that has to be satisfied. If spectral lines exist, the total transmitted power has to be backed off such that the spectral lines satisfy the spectral mask, resulting in a loss in SNR (signal-to-noise ratio).

The modulation of this sequence of pulses can be

- Pulse-position modulation (PPM), as suggested in [7]. This modulation enables simple detectors, which only need to determine whether there is more energy at time t_0 or at time $t_0 + \delta$. This allows the use of non-coherent receivers (energy detectors), as well as the use of coherent receivers. For non-coherent receivers, it is required that δ be larger than the delay spread of the channel.

- Pulse-amplitude modulation (PAM), such as BPSK (binary phase-shift keying) [17]. BPSK can only be used in conjunction with coherent receivers. However, it gives better performance than pulse-position modulation since it is an antipodal modulation format. The transmitted signal for BPSK is

$$s_{\mathrm{tr}}(t) = \sum_{j=-\infty}^{\infty} d_j b_{\lfloor j/N_f \rfloor} w_{tr}\left(t - jT_f - c_j T_c\right) \quad (11)$$

$$= \sum_{k=-\infty}^{\infty} b_k w_{seq}\left(t - kT_s\right),$$

where $w_{tr}(t)$ is the transmitted unit-energy pulse, T_f is the average pulse repetition time, N_f is the number of frames (and therefore also the number of pulses) representing one information symbol of length T_s, and b is the transmitted information symbol, i.e., ± 1. $w_{seq}(t)$ is the transmitted pulse sequence representing one symbol. The TH (time-hopping) sequence provides an additional time shift of $c_j T_c$ seconds to the jth pulse of the signal, where T_c is the chip interval and the c_j are the elements of a pseudorandom sequence, taking on integer values between 0 and $N_c - 1$. To prevent pulses from overlapping, the chip interval is selected to satisfy $T_c \le T_f / N_c$. The polarity randomization is achieved by having each pulse multiplied by a (pseudo) random variable, d_j, that can take on the values of $+1$ or

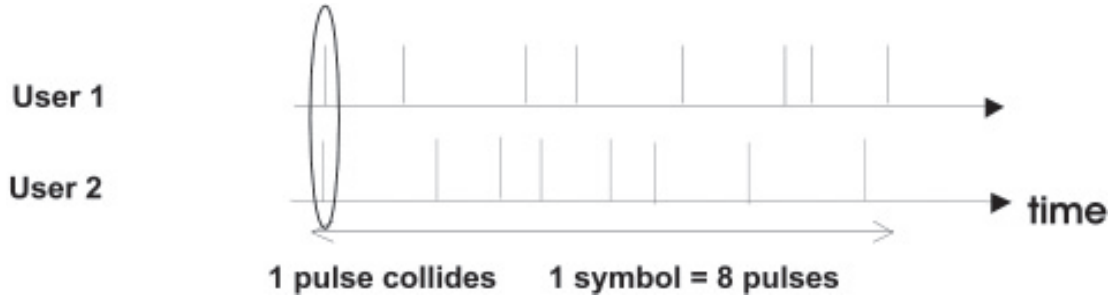

Figure 3. The principle of time-hopping impulse radio for the suppression of catastrophic collisions.

-1 with equal probability. The sequences d_j and c_j are assumed to be known at the transmitter and receiver.

4.2 DS-CDMA

Although UWB has long been associated with impulse radio, other spreading methods, like direct-sequence CDMA, can be used in a straightforward way to generate UWB signals. DS-CDMA spreads the signal by multiplying the transmitted signal with a second signal that has a very large bandwidth. The bandwidth of this total signal is approximately the same as the bandwidth of the wideband spreading signal. The most popular spreading sequences are binary *m*-sequences (maximum-length sequences), generated by shift-registers with feedback. The transmitted signal is thus

$$s_{tr}(t) = \sum_{j=-\infty}^{\infty} d_j b_{\lfloor j/N_f \rfloor} w_{tr}(t - jT_c) \qquad (12)$$

$$= \sum_{k=-\infty}^{\infty} b_k w_{seq}(t - kT_s),$$

where the symbols have the same meaning as in Equation (11).

The difference between a conventional (e.g., cellular) DS-CDMA system and a UWB signal is the chip rate, i.e., $1/T_c$. Consequently, both the theoretical underpinnings, and the implementation aspects of DS-CDMA, are well understood. This facilitates their use for UWB systems.

When comparing Equations (12) and (11), we find some important similarities. Both TH-IR and DS-CDMA transmit a bit by multiplying it with a spreading sequence $w_{seq}(t)$, and the bandwidth is essentially determined by the duration and shape of a basis pulse, $w_{tr}(t)$. The major difference lies in the nature of the spreading sequence. For the DS-CDMA case, it consists only of binary values, ± 1, while in the IR case, it consists of many zeroes, with several ± 1 s located at pseudorandom positions. As a consequence, DS-CDMA signals can be more difficult to generate: it is not just a matter of generating short pulses at large intervals, but rather it requires the continuous generation of those pulses. Furthermore, DS-CDMA as described above does not allow non-coherent (energy-detection) reception.

4.3 Receivers for Impulse Radio and DS-CDMA

As we discussed in Section 3, the multipath propagation leads to multiple echoes of the original signal arriving at the receiver. In a UWB system with large absolute bandwidth, a large number of multipath components can be resolved. Coherent reception of IR or DS-CDMA signals requires the use of receivers that collect the energy of the available resolvable multipath components: usually, this means rake receivers. The basic version of the rake receiver consists of multiple correlators (fingers), where each of the fingers can detect/extract the signal from one of the multipath components. The outputs of the fingers are appropriately weighted and combined to reap the benefits of rake diversity. The equivalent matched-filter version of the receiver involves a matched front-end processor (MFEP) (matched only to the transmitted waveform), followed by a tapped delay line and a combiner.

For systems with a large absolute bandwidth, the number of resolvable multipath components can become very large: an optimum receiver would thus need a large number of fingers. Complexity and performance issues have motivated studies on rake receiver with a limited number of fingers [29]. The SRake receiver, a reduced-complexity multipath-combining system, selects the L_b best paths and then combines the selected subset using maximal-ratio combining [32]. This receiver makes the best use of its L_b available fingers, but – in order to do a proper selection of which paths to use – needs to keep track of all multipath components. A further simplification is achieved with the PRake, which receives and combines the *first* L_b arriving paths, which are not necessarily the best. The complexity reduction with respect to the SRake is created by the absence of the selection mechanism.

An additional complication occurs in UWB systems with large relative bandwidth. As shown in Equation (1), each multipath component suffers from distortion, $\chi_i(t,\tau)$. For optimum reception, a rake receiver needs to know the functions $\chi_i(t,\tau)$. Alternatively, the receiver must sample at the Nyquist rate and process all the sample values, the number of which can be significantly higher than the number of multipath components. As a further important conclusion, we find that the matched filter has to take the distortions of the waveform, w_{tx}, by the antennas into account. If that is not possible, it is desirable that the antennas distort w_{tx} as little as possible.

Since coherent reception of impulse radio can be challenging, alternative demodulation schemes have been investigated. Non-coherent reception is the simplest approach, and works very well when the delay spread of the channel is small and the signal-to-noise ratio is high. For large delay spreads, the receiver has to integrate the received energy over a long period, which also means that it picks up a lot of noise in the process. Furthermore, the contribution of the noise-noise cross-terms in the squared signal leads to an additional deterioration of the performance. Finally, non-coherent detection is more sensitive to interference.

As a compromise between coherent and non-coherent schemes, transmitted-reference (TR) schemes are often used. In TR, we first transmit a reference pulse of known polarity (or position), followed by a data pulse the polarity

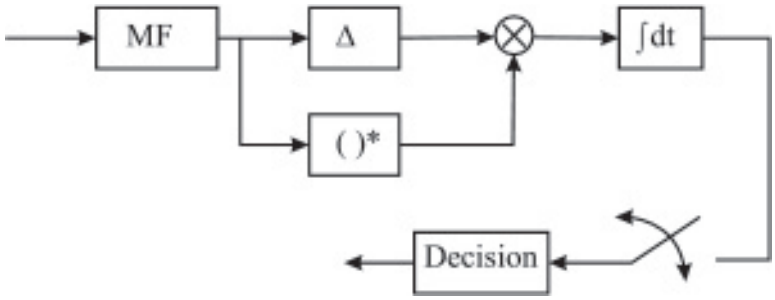

Figure 4. Building blocks for the basic hybrid receiver. Note that the sampling circuit performs symbol rate sampling.

(position) of which is determined by the information bit. At the receiver, we then have to multiply the received signal with a delayed version of itself (see Figure 4). This scheme has a SNR that is worse than that of a coherent receiver (due to the occurrence of noise-noise cross terms), and comparable to a non-coherent receiver. It is not sensitive to distortions by antennas and channels, because both the data pulse and the reference pulse undergo the same distortions. Furthermore, it is less sensitive to interference than non-coherent detection. A practical problem is the implementation of a suitable on-chip delay line. This problem is avoided by the frequency-shifted reference system [33], which uses a frequency-shifted reference signal instead of a time-delayed signal, and thus needs a mixer instead of a delay line at the receiver.

4.4 OFDM

OFDM (orthogonal frequency-division multiplexing) transmits information in parallel on a large number of subcarriers, each of which requires only a relatively small bandwidth. This approach is widely used for Wi-Fi and WiMax systems, and its theory and implementation are now well understood. Figure 5 shows a block diagram. The data stream is first serial-to-parallel converted. It is then modulated onto subcarriers that are separated by a frequency spacing W/N, where W is the total transmission bandwidth, and N is the number of subcarriers. While analog implementations of the modulators/demodulators (Figure 5a) are possible, today's systems perform an inverse fast Fourier transform (IFFT) on the data (Figure 5b) to

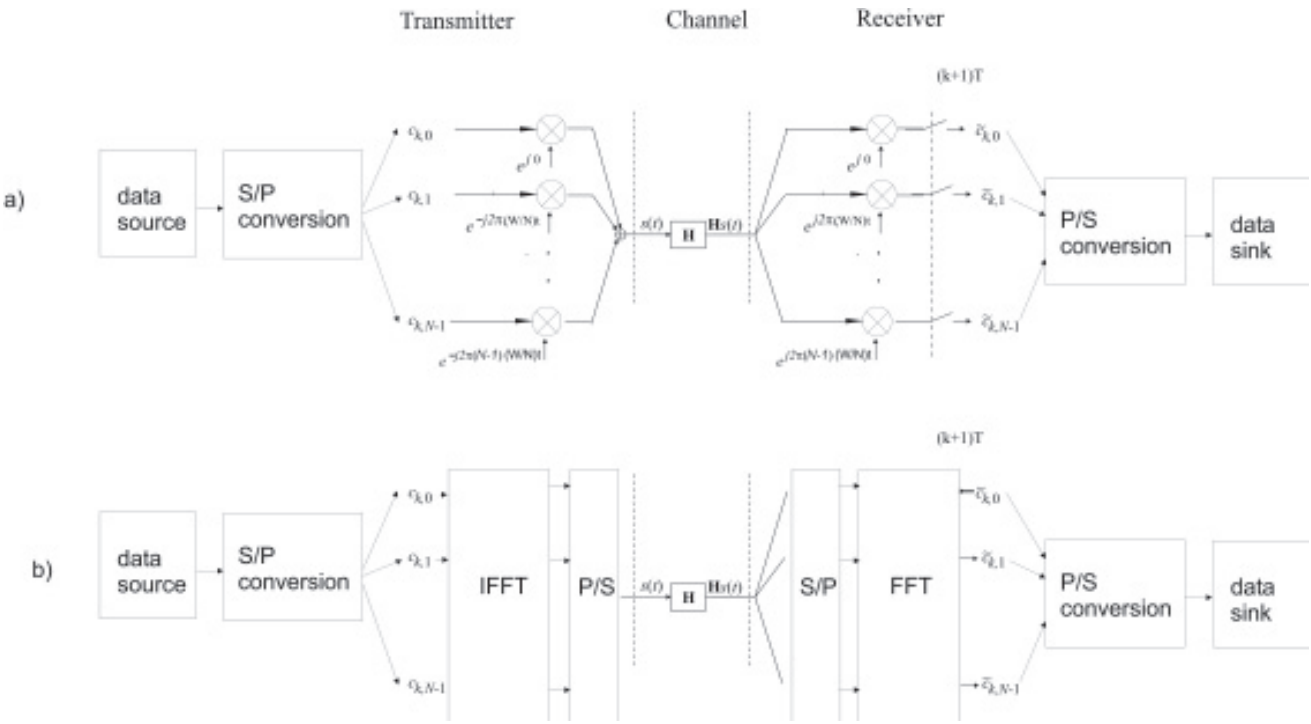

Figure 5. The principle of OFDM: (a) an analog implementation and (b) a digital implementation (from [17], copyright 2005 John Wiley & Sons Limited, reproduced with permission).

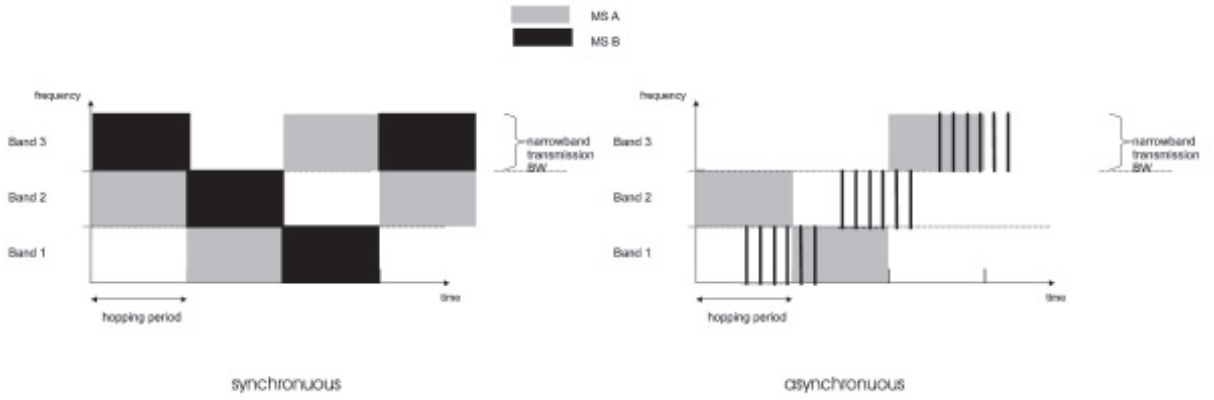

Figure 6. Frequency-hopping multiple access with synchronous and asynchronous users (from [17], copyright 2005 John Wiley & Sons Limited, reproduced with permission).

achieve the same effect. The latter approach does not need multiple local oscillators, and is thus the one in use today. However, it requires an IFFT and analog-to-digital converters operating at high speeds (a clock speed of approximately W).

OFDM is a highly spectrally efficient modulation method, and does not perform any inherent spreading. It must thus be combined with other spreading methods, like low-rate convolutional coding, repetition coding, or frequency hopping. Furthermore, OFDM in its original form transmits each information symbol on one carrier, and thus does not exploit the frequency diversity inherent in a UWB system. This problem is also circumvented by the use of appropriate coding and/or by the use of multi-carrier-CDMA [30].

The impact of channels and antennas on UWB-OFDM systems is similar to the impact on conventional OFDM systems. In either case, the receiver determines the distortion (attenuation and phase shift) on each subcarrier, and compensates for it. The choice of subcarrier spacing depends mostly on the channel characteristics, especially the *maximum excess delay*, and not on the total system bandwidth. Rather, the total number of tones increases approximately linearly with the total bandwidth.

4.5 Frequency Hopping

Frequency hopping (FH) uses different carrier frequencies at different times. In *slow* frequency hopping, one or more symbols are transmitted on a given frequency. In *fast* frequency hopping, the frequency changes several times per symbol. The bandwidth of the resulting signal is determined by the range of the oscillator, not the bandwidth of the original signal that is to be transmitted. If different users use different hopping codes (which define in which sequence the carrier frequencies are used), the multi-user interference can be greatly reduced, because interference occurs only when two devices use the same carrier frequency at the same time.

For more details, we have to distinguish between the case of synchronized and unsynchronized users. In the synchronized case, all users can use the same hopping pattern, but with different offsets (see Figure 6a). In the unsynchronized case, we have no control over the relative timing between the different users. The hopping sequences must thus make sure that there is little multiple-access interference for all possible time shifts between the users; otherwise, catastrophic collisions between users could occur. The situation is analogous to TH-IR, where we need to find time-hopping sequences that avoid catastrophic collisions.

A frequency-hopping transmitter can be implemented as a conventional narrowband modulator, followed by mixing with the output of a frequency-agile oscillator. a receiver can be constructed in a similar way. This receiver can be used as long as the delay spread of the channel is much shorter than the hopping interval. Otherwise, multipath energy is still arriving on one subcarrier while the receiver has already hopped to a different frequency.

Frequency hopping can be used either as a multiple-access scheme of its own, or it can be combined with other schemes, e.g., OFDM. The latter approach simplifies implementation, as the sampling and A/D conversion now has to be done only with a rate corresponding to the width of the instantaneously used (OFDM) bandwidth, instead of the full UWB system bandwidth.

5. Applications and System Standards

5.1 UWB Sensor Networks and the IEEE 802.15.4a Standard

UWB is a technology that is well suited for sensor networks. In such networks, data rates are low (< 1 Mbit/s), but restrictions on size and energy consumption are very stringent. Furthermore, geolocation is an important task, since the location from which the sensing data originate is essential. Low-data-rate systems are also envisaged for

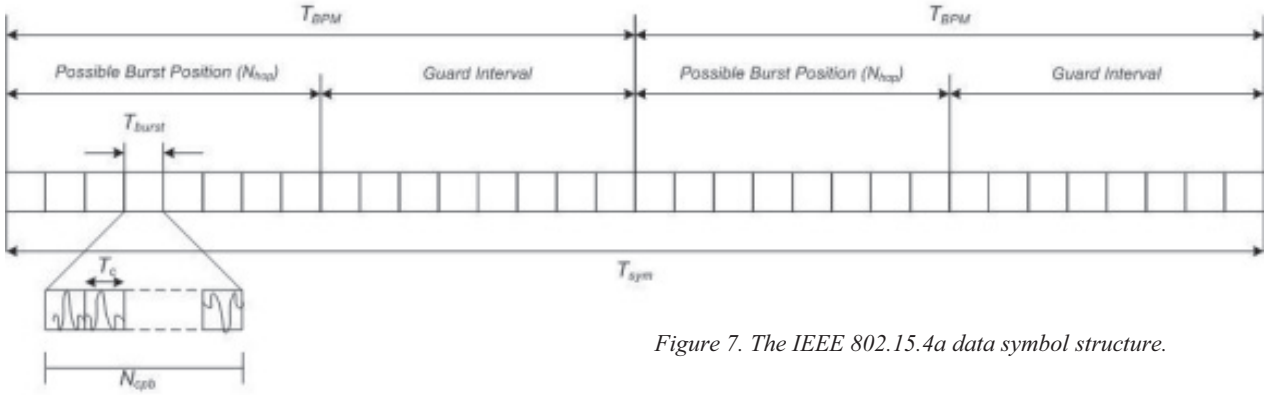

Figure 7. The IEEE 802.15.4a data symbol structure.

emergency communications, e.g., between people within a collapsed building and rescue workers [34].

A standard for such systems was established by the IEEE 802.15.4a group. It is based on TH-IR, and uses a modulation/multiple-access format that supports both coherent and non-coherent receivers within the same network (not all devices in a network have the same application and cost requirements). In particular, a combination of burst-position modulation (BPM) and binary phase-shift keying (BPSK) is used to support both coherent and non-coherent receivers using a common signaling scheme. The combined BPM-BPSK is used to modulate symbols, with each symbol being composed of a burst of UWB pulses. The position of this burst within the first half or second half of a data-symbol period, T_{sym}, indicates a bit of "0" or "1," respectively.

Additionally, the burst polarity ($+1$ or -1) is used to modulate a second information bit. The polarity modulation is used to convey a parity check bit rather than user data, since non-coherent receivers are incapable of recovering the pulse-burst phase. In order to ensure that the signals can still be decoded by non-coherent receivers, a systematic code has to be used (a systematic code is one in which the information bits are transmitted unchanged along with the parity-check bits). The systematic bits are used to determine the PPM position of the burst, and are thus visible to both non-coherent and coherent receivers. The parity bits are modulated onto the burst phase, and are thus visible only to coherent receivers. The structure and timing of a UWB PHY symbol is illustrated in Figure 7.

5.2 High-Data-Rate Communications and the ECMA 268 Standard

Another important application area is data transmission with a very high rate (more than 100 Mbit/s). As discussed in the introduction, the range of such systems is limited to some 10 m. This set of data rates and ranges is used especially for consumer electronics and personal-computing applications, such as transmission of HDTV (high-definition television) streams from a set-top box or a DVD player to the TV, or wireless USB (universal serial bus) connections. A standard for such systems was established in [31], based on a combination of OFDM with frequency hopping over three 500 MHz bands. A further increase in data rate for wireless HDMI is currently being aimed at by UWB systems operating in the 60 GHz band, where higher transmitter power spectral density is allowed.

5.3 Other Applications

Going beyond communications, UWB radars have developed into an important market niche, used mainly for two purposes: (i) high-performance radars that have smaller "dead zones," and (ii) radars for close ranges that can penetrate walls and ground. The second application is useful for surveillance, urban warfare, and landmine detection. Most of the applications in this area are classified, as they serve military or law-enforcement purposes. A commercial application is the vehicular collision-avoidance radar. Such a radar typically operates in the microwave range (24-29 GHz or around 60 GHz). Another promising application is biological imaging, e.g., for cancer detection.

6. Summary and Conclusions

This paper gave an overview of UWB communications. By using a large bandwidth, UWB can either provide a high data rate, or use a large spreading factor to increase range and mitigate interference. In addition, UWB communications are more robust to fading, and enable more precise geolocation, than narrowband systems. A number of methods are available to generate UWB signals: the most important one is time-hopping impulse radio, but OFDM, frequency hopping, and direct-sequence CDMA are also possible options. Major challenges for the development of UWB systems lie in the design of simple and energy-saving transceivers, UWB antenna design, as well as the understanding of UWB channels, which differ fundamentally from narrowband wireless channels.

Like many new technologies, UWB was first overhyped, and then prematurely declared dead when it did not live up to the hype. However, by now it has become widely accepted that UWB communications is a very useful technique for a number of applications that are important but limited in scope. In particular, the following applications are important: (i) short-range communications with extremely high data rates, (ii) medium-range communications with low data rates and extremely low power consumption, and/or (iii) communication combined with precision geolocation. Further developments of the underlying science will open up additional future applications.

7. Acknowledgments

The author would like to thank the many people with whom he has collaborated with regard to and discussed UWB, and who shaped his views on this topic: Prof. Moe Win, Dr. Dajana Cassioli, Prof. Larry Greenstein, Prof. Robert Scholtz, Prof. Robert Qiu, Dr. Saeed Ghassemzadeh, Dr. Jeff Foerster, Dr. Marcus Pendergrass, Prof. Fredrik Tufvesson, Dr. Johan Karedal, Mr. Telmo Santos, Dr. Chia-Chin Chong, Dr. Juergen Kunisch, Mr. Ulrich Schuster, Dr. Jin Zhang, Dr. Philip Orlik, Dr. Zafer Sahinoglu, Dr. Chunjee Duan, Dr. Ubli Mitra, Dr. Francois Chin, Dr. Ismael Lakkis, Dr. Patrick Kinney, Prof. Thomas Kaiser, Dr. Ian Opperman, Prof. Sherman Shen, Dr. Sinan Gezici, Prof. H. Vincent Poor, Prof. Dennis Goeckel, and Prof. Huaping Liu.

8. References

1. M. G. diBenedetto, T. Kaiser, A. F. Molisch, I. Oppermann, C. Politano, and D. Porcino (eds.), *UWB Communications Systems, A Comprehensive Overview*, New York, Hindawi Publishing Corporation, 2005.

2. M. Ghavami, L. B. Michael, and R. Kohno, *Ultra Wideband Signals and Systems in Communication Engineering*, New York, Wiley, 2004.

3. L. Yang and G. B. Giannakis, "Ultra-Wideband Communications – An Idea Whose Time Has Come," *IEEE Signal Processing Magazine*, **21**, 6, November 2004, pp. 26-54.

4. R. C. Qiu, H. Liu, and X. Shen, "Ultra-Wideband for Multiple Access Communications," *IEEE Communications Magazine*, **43**, 2, February 2005, pp. 80-87.

5. R. A. Scholtz, "Multiple Access with Time-Hopping Impulse Modulation," Proceedings of IEEE MILCOM, 1993, pp. 447-450.

6. M. Z. Win and R. A. Scholtz, "Impulse Radio: How it Works," *IEEE Comm. Lett.*, **2**, 2, February 1998, pp. 36-38.

7. M. Z. Win and R. A. Scholtz, "Ultra-Wide Bandwidth Time-Hopping Spread-Spectrum Impulse Radio for Wireless Multiple-Access Communications," *IEEE Trans. Comm.*, **48**, 4, April 2000, pp. 679-691.

8. S. Gezici, Z. Tian, G. B. Giannakis, H. Kobayashi, A. F. Molisch, H. V. Poor, and Z. Sahinoglu, "Localization via Ultra-Wideband Radios: A Look at Positioning Aspects for Future Sensor Networks," *IEEE Signal Processing Magazine*, **22**, 4, July 2005, pp. 70-84.

9. M. A. Win and R. A. Scholtz, "On the Energy Capture of Ultra-Wide Bandwidth Signals in Dense Multipath Environments," *IEEE Comm. Lett.*, **2**, 9, September 1998, pp. 245-247.

10. D. Cassioli, M. Z. Win, and A. F. Molisch, "The Ultra-Wide Bandwidth Indoor Channel: From Statistical Models to Simulations," *IEEE Journal on Selected Areas in Communications*, **20**, 6, August 2002, pp. 1247-1257.

11. Federal Communications Commission, "First Report and Order 02-48," 2002.

12. P. C. Pinto and M. Z. Win, "Spectral Characterization of Wireless Networks," *IEEE Wireless Communications*, **14**, 6, December 2007, pp. 27-31.

13. A. F. Molisch, "Ultrawideband Propagation Channels – Theory, Measurement, and Modeling," *IEEE Transactions on Vehicular Technology*, **54**, 5, September 2005, pp. 1528-1545.

14. A. F. Molisch, "Ultrawideband Propagation Channels and Their Impact on System Design," Proceedings of the IEEE Conference on Microwave, Antennas, Propagation, and EMC Technologies for Wireless Communications (MAPE), 2007.

15. A. F. Molisch, "Ultrawideband Propagation Channels," *Proc. IEEE*, **97**, 2, February 2009, pp. 353-371 .

16. H. Schantz, "A Brief History of UWB Antennas," Proceedings of Ultra Wideband Systems and Technologies, 2003, pp. 209-213.

17. A. F. Molisch, *Wireless Communications*, New York, Wiley, 2005.

18. G. Kadel and R. Lorenz, "Impact of the Radio Channel on the Performance of Digital Mobile Communication Systems," Proceedings of the Sixth IEEE International Symposium on Personal, Indoor and Mobile Radio Communications (PIMRC'95), 1995, pp. 419-423.

19. J.-P. Rossi, "Influence of Measurement Conditions on the Evaluation of Some Radio Channel Parameters," *IEEE Transactions on Vehicular Technology*, **VT-48**, 4, July 1999, pp. 1304-1316.

20. R. C. Qiu and I. Lu, "Multipath Resolving with Frequency Dependence for Broadband Wireless Channel Modeling," *IEEE Transactions on Vehicular Technology*, **48**, 1, January 1999, pp. 273-285.

21. A. F. Molisch, K. Balakrishnan, C. C. Chong, D. Cassioli, S. Emami, A. Fort, J. Karedal, J. Kunisch, H. Schantz, K. Siwiak, and M. Z. Win, "A Comprehensive Standardized Model for Ultrawideband Propagation Channels," *IEEE Transactions on Antennas and Propagation*, **54**, 11, November 2006, pp. 3151-3166.

22. B. Donlan, D. McKinstry, and R. Buehrer, "The UWB Indoor Channel: Large and Small Scale Modeling," *IEEE Transactions on Wireless Communications*, **5**, 10, October 2006, pp. 2863-2873.

23. A. Saleh and R. A. Valenzuela, "A Statistical Model for Indoor Multipath Propagation," *IEEE Journal on Selected Areas in Communications*, **5**, 2, February 1987, pp. 128-137.

24. D. Cassioli, M. Z. Win, and A. F. Molisch, "The Ultra-Wide Bandwidth Indoor Channel: From Statistical Model to Simulations," *IEEE Journal on Selected Areas in Communications*, **20**, 6, August 2002, pp. 1247-1257.

25. J. Kunisch and J. Pamp, "Measurement Results and Modeling Aspects for the UWB Radio Channel," Proceedings of the IEEE UWBST, 2002, pp. 19-23.

26. J. R. Foerster and Q. Li, "UWB Channel Modeling Contribution from Intel," Tech. Rep. P802.15 02/279SG3a, 2002, IEEE P802.15 SG3a contribution.

27. A. F. Molisch, J. R. Foerster, and M. Pendergrass, "Channel Models for Ultrawideband Personal Area Networks," *IEEE Personal Communications Magazine*, **10**, 12, December 2003, pp. 14-21.

28. Y. P. Nakache and A. F. Molisch, "Spectral Shape of UWB Signals: Influence of Modulation Format, Multiple Access Scheme and Pulse Shape," Proceedings VTC 2003 Spring, 2003, pp. 2510-2514.

29. D. Cassioli, M. Z. Win, A. F. Molisch, and F. Vatelaro, "Performance of Selective Rake Reception in a Realistic UWB Channel," Proc. ICC 2002, 2002, pp. 763-767.

30. L. Hanzo, M. Muenster, B. Choi, and T. Keller, *OFDM and MC-CDMA for Broadband Multi-User Communications, WLANs and Broadcasting,* New York, Wiley, 2003.

31. European Computer Manufacturing Association, "UWB: High Rate Ultra Wideband PHY and MAC Standard," Tech. Rep., http://www.ecma-international.org, 2005.

32. M. Z. Win and G. Chrisikos, "Impact of Spreading Bandwidth and Selection Diversity Order on Selective Rake Reception Wideband Wireless Digital Communications," in A. F. Molisch (ed.), *Wideband Wireless Digital Communications*, London, Prentice-Hall, 2001.

33. D. L. Goeckel and Q. Zhang, "Slightly Frequency-Shifted Reference Ultra-Wideband (UWB) Radio," IEEE Transactions on Communications, **55**, 3, March 2007, pp. 508-519.

34. J. Zhang, P. Orlik, Z. Sahinoglu, A. F. Molisch, and P. Kinney, "UWB Systems for Wireless Sensor Networks," *Proceedings of the IEEE*, **97**, 2, February 2009, pp. 313-331.

Radio Science Doctoral Abstracts

Ashik Paul, ***Equatorial Anomaly Gradient Effects on GPS***, Institute of Radio Physics and Electronics, University of Calcutta, Kolkata, India, December 2008; E-mail: ashik_paul@rediffmail.com.
Relevant Commission: G

Abstract

The present thesis is based on studies of the deleterious effects of the sharp gradients of the equatorial ionization anomaly and ionospheric irregularities on satellite based augmentation system (SBAS) and their methods of prediction. Total electron content (TEC), measured at Calcutta over more than one solar cycle from 1977 through 1990, has been compared with values obtained from the International Reference Ionosphere (IRI-95) and the Parameterized Ionospheric Model (PIM1.6). While IRI does not follow the nature of variation of the measured TEC at all, PIM shows a close match with the measured data, particularly during the early morning and late night hours, but exhibits marked differences near the time of diurnal maximum. A method of converting the vertical to slant TEC appropriate for any SBAS operational in this region has been suggested, involving integration of the ionization along the signal propagation path, which is referred to as the path-integrated (PI) slant TEC in the present thesis. An optimum grid size for the Indian SBAS, GPS And Geo-Augmented Navigation (GAGAN), has been calculated to be 1° ´ 1.2°, which is markedly different from the 5° ´ 5° used in the US Wide Area Augmented System (WAAS).

The equatorial ionosphere is characterized by severe plasma depletions with steep gradients on the edges. The steep gradients on the edges have been studied using GPS TEC measured at Pune. The duration of bubbles observed with GPS transmissions has been found to be dependent on the relative velocity between the satellite at the pierce-point altitude and the predominantly eastward drift of the ionospheric irregularities, and the orientation of the satellite trajectory. An asymmetry has been noted between the eastern and the western walls of a drifting plasma bubble. Parameters obtained using different techniques have been examined to find an association with post-sunset equatorial scintillations affecting geostationary L-band satellite links at Calcutta. Among all the different methods, measuring the latitudinal gradient of TEC serves as the best precursor to occurrence of scintillations. However, in locations where installation of a satellite signal receiving system is difficult, latitudinal distribution of topside ionization density from DMSP satellites, available online, could readily provide a simple measure.

Call for Submissions

In order to encourage dialogue with young radio scientists, the *Radio Science Bulletin* publishes the abstracts of relevant doctoral dissertations or theses in the fields of radio science as soon as they are approved by universities or other degree-awarding institutions.

We thus call upon supervisors or research-group leaders to bring this opportunity to the attention of recently qualified doctoral graduates, asking them to e-mail their abstracts to the address given below. The date of publication should be given, with full details of the address of the awarding institution, and also an e-mail address for the author. It would also be helpful to indicate to which URSI Commissions the doctoral work relates most closely.

Peter Watson
University of Bath
E-mail: rsbursi@bath.ac.uk

Radio-Frequency Radiation Safety and Health

James C. Lin

Development of Cancer in Normal Mice Exposed to Mobile-Phone Radiation

The development and promotion of cancer by land-mobile cellular radio-communication radiation of differing frequencies and modulations were the subject of several studies using four different strains of normal mice: CD-1, ODC, CBA/S, and B6C3F1. An article in a previous column [1] described three studies using GSM-900 and genetically prone Em-Pim1 lymphoma mice, which produced varying results. Differences and uncertainties in the animal protocols and exposure systems limit the conclusions that can be drawn from these studies. Note that while results from the present four studies using normal mice add to our basic knowledge of potential interactions, they should not be regarded as confirmation or refutation of studies using Em-Pim1 transgenic mice.

Studies with the first three strains of mice were for exposures of one year or less. Both female and male B6C3F1 mice were the subjects of a two-year, whole-life study.

One of the studies involving exposures of one year or less investigated the potential for mobile-phone fields to promote skin cancer after a single dose of the carcinogen 7,12-dimethylbenz[a]anthracene (DMBA), using the CD-1 mouse model in a medium-term bioassay [2]. Since the combination of DMBA initiation and 12-O-tetradecanoylphorbol-13-acetate (TPA) promotion is routinely used to study carcinogenesis, TPA was used for positive control. In this study, 10-week-old female CD-1 mice were treated with a single application of DMBA on shaved dorsal skin. A week later, mice were divided into four groups: 48 for sham exposure (DMBA-sham), 48 for RF exposure (DMBA-RF), 30 for positive controls (DMBA-TPA), and 30 as cage controls (DMBA-control).

Mice were exposed dorsally to 1439 MHz RF radiation in individual chambers lined with absorbing materials in the near field of a monopole antenna, using time-division multiple-access (TDMA-1500) signals of a personal digital cellular (PDC) phone. The 19-week exposure was carried out for 1.5 h/day, five days/week, at a dorsal skin local peak SAR of 2.0 W/kg, with a whole-body average SAR of 0.084 W/kg. The fact that the ratio of peak to average SAR was 24 is irrelevant and misleading, because of localized exposure in the near field of the antenna with animals being partially restrained. It was not a whole-body exposure scenario.

The results showed that the incidences of skin cancers in DMBA-RF, DMBA-Sham, DMBA-TPA, and DMBA-Control groups were 0/48 (0%), 0/48 (0%), 29/30 (96.6%), and 1/30 (3.3%), respectively. As expected, the incidence in the DMBA-TPA group was nearly 100%: skin-tumor response sensitivity of the CD-1 mouse to the DMBA-TPA combination is well known. These results indicated that near-field, partial-body exposure to TDMA-1500 fields did not indicate a promotional effect on skin tumorigenesis initiated by DMBA.

The co-carcinogenic potential of GSM-900 fields (operating at 902.5 MHz, 0.577 ms pulses, and 217 Hz modulation) and DAMPS on ultraviolet (UV)-induced skin cancer was investigated using female ODC mice [3].

The digital advanced mobile phone system (DAMPS) is a second-generation mobile phone system developed for use in the US market; it has now been superseded by other technologies. It operates in the 800 and 900 MHz frequency bands, with 30 kHz channels. Like GSM, DAMPS is a digital wireless communication system. However, it employs a different, non-compatible version of the TDMA technology. The frequency was 849 MHz for this DAMPS-849 study; the pulse duration was 6.67 ms, and the pulse-repetition frequency was 50 Hz.

Groups of 50 transgenic female 12-15 week-old ODC-K2 mice were exposed for 1.5 h/day, five days per week, during the 52-week study. Identical rectangular waveguide

James C. Lin is with the University of Illinois at Chicago, 851 South Morgan Street (M/C 154), Chicago, Illinois 60607-7053 USA;
Tel: +1 (312) 413-1052 (direct); +1 (312) 996-3423 (main office); Fax: +1 (312) 996-6465;
E-mail: lin@uic.edu.

A version of this contribution appeared as James C. Lin, "Cell-Phone Radiation and Cancer Studies in Normal Mice," *IEEE Antennas and Propagation Magazine*, 51, 2, April 2009, pp. 186-188.

chambers were used for the RF and sham exposures. The mice were kept in small cylindrical acrylic restrainers that allowed the animals to turn around, except for some larger ones toward the end of the experiment. Further, the placement of the restrainers in the transverse orientation of waveguide chambers prevented the mice from aligning their longitudinal axis parallel to the electric field. Each chamber accommodated the exposure of 25 mice at a time (additional animals from the same litters as the study animals were used to make up for the capacity of the chambers). The order of RF and sham exposures was changed weekly.

The whole-body average SAR was reported to be 0.5 W/kg in both the GSM and DAMPS groups. The whole-body average SARs were 4.0 and 1.5 W/kg for a given pulse in the two respective groups. The maximum deviation of the SAR was estimated to be 30% both for the GSM-900 and DAMPS-849 groups.

The UV radiation was administered three times per week at a dose of 240 J/m2 (1.2 times the human minimum erythemal dose) using lamps simulating the solar spectrum, except for the cage-control group. The protocol required UV exposures to precede RF exposures on Mondays and Fridays, and on Wednesdays the animals were exposed to RF first.

Among the mice available for histopathology, eight were cage controls, and 27, 26, and 26 were in the GSM-, DAMPS-, and sham-exposed groups, respectively. Microscopic skin tumors developed in three (11.5%) mice that were subjected to UV exposure and served as sham-exposed. None in the cage-control group developed a macroscopic skin tumor. The exposure results showed that four (15%) and five (19%) of the GSM-900 and DAMPS-849 exposed mice developed macroscopic skin tumors, but neither the GSM nor DAMPS exposures had a statistically significant effect on the development of skin tumors in normal ODC mice. Furthermore, GSM and DAMPS fields did not appear to act as a co-carcinogenic to UV-induced skin tumors.

The capacity of mobile-phone RF radiation to act as a cancer promoter was the subject of an investigation examining the mobile phone's effect on the development of cancers initiated in mice by ionizing radiation [4]. Ionizing radiation was selected as an initiator because it is known to induce leukemia and lymphomas, as well as several other types of cancers, in mice. Young female CBA/S mice (three to five weeks old) were randomized into four groups of 50 mice: cage control, sham, and two groups of RF-exposed animals. Except for the cage-control group, all mice were irradiated by X-rays at the beginning of the study, and then exposed to mobile-phone RF radiation for 1.5 h per day, five days per week for 78 weeks.

The total-body X-ray dose was 4 Gy, delivered as three equal fractions of 1.33 Gy at one-week intervals with linear accelerators. Appropriate steps were taken to ensure uniform irradiation of the whole body. The mobile-phone exposure started on the day of exposure to the ionizing radiation.

The two types of RF exposures were signals from the analog Nordic Mobile Telephony (NMT) system at 902.5 MHz, used mainly in North European countries, and the digital GSM system, operating at 902.4 MHz. The exposures involved three identical rectangular waveguide chambers: the same as those used by this group in another study, mentioned above [3]. The average whole-body SAR was 0.35 and 1.5 W/kg for the GSM-900 and NMT-900 groups, respectively.

The survival rate of mice in the cage-control group was significantly higher, at 96%, compared to 68% in the sham-exposed group; cage controls were not exposed to ionizing radiation. The survival rates of 68%, 66%, and 68% in the GSM, NMT, and sham-exposed groups, respectively, were similar. Moreover, the results showed that the proportion of X-ray irradiated mice with any neoplasm were 94%, 98%, and 98% in the GSM, NMT, and sham-exposed groups, respectively. Exposure to mobile-phone radiation did not significantly increase the incidence of any primary neoplasm in the tissues examined. The overall incidence of primary malignant neoplasm was 50%, 56%, and 40% in the GSM, NMT, and sham-exposed groups, respectively. The corresponding incidences of benign neoplasm were 82%, 76%, and 84%.

While the results of this study do not suggest cancer promotion by RF radiation from GSM-900 or NMT-900 mobile phones, the proportion of X-ray irradiated mice with any neoplasm was as high as 100% in all exposed groups, irrespective of exposure conditions.

It should also be mentioned that a particular limitation or uncertainty surrounding this study was the use of the waveguide-chamber exposure system, which likely produced highly selective absorption among the animals. Further, the dosimetric determinations were estimations of time and spatially averaged absorptions, and they bore little relation to daily exposure or individual SAR, or their distribution inside the animal's body. Some of the animals may have encountered either considerably lower or higher SARs during a given exposure session, which would be washed out in the averaged responses.

The singular, two-year, whole-life study investigated the carcinogenic potential from exposure to GSM and Digital Cellular System (DCS) fields operating at 902 and 1747 MHz, respectively [5]. The study involved a large number (1,170) of female and male B6C3F1 mice. This strain of mice is a first-generation hybrid strain produced by crossing C57BL/6 females with C3H males. The animals were eight to nine weeks of age at the start of RF exposures.

The DCS system is commonly known as DCS 1800, and is a mobile communication system that operates in the 1710 to 1880 MHz region of the frequency spectrum. It uses the spectrum between 1710 MHz and 1785 MHz for

uplink, and 1805 MHz and 1880 MHz for downlink operations, respectively. Standard signaling schemes were used in this study. The study design included groups of 50 B6C3F1 mice of each sex for cage control, sham, GSM-900, and DCS-1800 exposures at whole-body averaged SARs of 0.4, 1.3, and 4.0 W/kg for two hours per day, five days per week for two years.

The sham- and RF-exposed groups were housed in the same room. It should be noted that while 100 mice were designated as cage controls, they were not included in any comparison among various study groups. Instead, the publication included the statement, "comparison to published tumor rates in untreated mice revealed that the observed tumor rates were within the range of historical control data" [5].

The RF exposure was conducted using "Ferris wheel" chambers, developed for the two frequencies of interest. Each chamber supported the simultaneous exposure of up to 65 mice restrained in plastic tubes. The GSM-900 and DCS-1800 exposures were conducted during the same time of the year, under essentially the same technical, laboratory, and environmental conditions.

Corresponding to the whole-body average SARs of 0.4, 1.3, and 4.0 W/kg, the maximum average SAR during an active burst was 3.7, 11.1, and 33.2 W/kg, respectively. The average absorption in the brain of a mouse was 2.5 W/kg for GSM and 5 W/kg for DCS. It should be noted that while the incident field was adjusted to maintain the same exposure level, independent of the animal's mass or age, the average uncertainty for SAR was ±400 and 200% for GSM and DCS, respectively. Moreover, the spatial peak SAR at 4 W/kg might have been as high as 250 W/kg for GSM and 30 W/kg for DCS. Obviously, the SARs varied widely under both GSM and DCS exposures.

For GSM-900 exposures, the results showed that while the number of tumor-bearing B6C3F1 female mice (77%) at all levels was about 18% higher than in males (65%), they were not significantly different from the sham-exposure group in either females or males [5]. Also, the results did not show any significant increase in the incidence of any particular organ-specific tumor type in the GSM-exposed compared to the sham-exposed. Likewise, the incidence of hepatocellular carcinomas was similar in the GSM- and sham-exposed groups. However, there appeared to be a dose-dependent decrease of the incidence of hepatocellular adenomas in males. Further, the decrease of hepatocellular adenomas in males exposed to 4.0 W/kg was significantly different ($P = 0.048$) from that in the sham-exposed males.

In DCS-exposed mice, the incidence of tumor-bearing females was highest (37/50, 74%) in the sham-exposed group, but it was not significantly different from the 31/50 (62%), 35/50 (70%), and 33/50 (66%) for 0.4, 1.3, and 4.0 W/kg groups, respectively. However, there was a distinct dose-dependent decrease in the incidence of tumor-bearing males compared to the sham-exposed group. Specifically, the incidence was 37/50 (74%) in the sham-exposed group and 30/50 (60%; $P = 0.202$), 25/50 (50%; $P = 0.023$), and 24/50 (48%; $P = 0.013$) in the three respective SAR levels.

Thus, while the incidence of hepatocellular carcinomas was similar in DCS and sham-exposed groups, in male C57BL/6 mice there was a dose-dependent decrease. Moreover, the decrease in males exposed to 4.0 W/kg was significantly different ($P = 0.015$) from that in the sham-exposed.

In summary, among the studies of cancers in normal (non-transgenic) mice, only one was a two-year or life-long study, while others varied from 19 to 78 weeks. There were two investigations on the promotional or co-carcinogenic potential for DMBA- and UV-induced skin cancers in CD-1 mice for 19-week exposures to TDMA fields, and ODC mice for 52-week exposures to GSM and DAMPS modulations, respectively. In both cases, the animals were partially restrained. These experiments did not indicate a promotional or co-carcinogenic effect on skin tumorigenesis.

The two-year study on the carcinogenic potential in female and male B6C3F1 mice is especially worthy of note in several regards. While exposure of male and female B6C3F1 mice to wireless GSM-900 and DCS-1800 fields did not show any overall increase in the incidence of tumors, there was a dose-dependent decrease in the number of tumor-bearing males, and more so for incidence of hepatocellular carcinomas. The SARs in restrained mice varied widely (by as much as 85-fold) for both GSM and DCS exposure in "Ferris wheel" chambers, although the incident field was adjusted to maintain the same exposure level, independent of the animal's mass or age.

References

1. J. C. Lin, "Tumor Incidence Studies in Lymphoma-Prone Mice Exposed to GSM Mobile-phone Radiation," *Radio Science Bulletin*, **No. 324**, March 2008, pp. 41-44.

2. K. Imaida, K. Kuzutani, J. Wang, O. Fujiwara, T. Ogiso, K. Kato, and T. Shirai, "Lack of Promotion of 7,12-Dimethylbenz[a]anthracene-Initiated Mouse Skin Carcinogenesis by 1.5 GHz Electromagnetic Near Fields," *Carcinogenesis*, **22**, 11, 2001, pp. 1837-1841.

3. P. Heikkinen, V. M. Kosma, L. Alhonen, H. Huuskonen, H. Komulainen, T. Kumlin, J. T. Laitinen, S. Lang, L. Puranen, and J. Juutilainen, "Effects of Mobile Phone Radiation on UV-Induced Skin Tumourigenesis in Ornithine Decarboxylase Transgenic and Non-Transgenic Mice, *Int. J. Radiat. Biol.*, **79**, 4, 2003, pp. 221-233.

4. P. Heikkinen, V-M. Kosma, T. Hongisto, H. Huuskonen, P. Hyysalo, H. Komulainen, T. Kumlin, T. Lahtinen, S. Lang, L. Puranen, and J. Juutilainen, "Effects of Mobile Phone Radiation on X-Ray-Induced Tumorigenesis in Mice," *Radiat. Res*., **156**, 2001, pp. 775-785.

5. **T. Tillmann, H. Ernst, S. Ebert, N. Kuster, W. Behnke, S. Rittinghausen, and C. Dasenbrock, "Carcinogenicity Study of GSM and DCS Wireless Communication Signals in B6C3F1 Mice,** *Bioelectromagnetics*, **28**, 2007, pp. 173-187.

Conferences

URSI CONFERENCE CALENDAR

URSI cannot be held responsible for any errors contained in this list of meetings.

July 2009

EMC'09 - 2009 International Symposium on Electromagnetic Compatibility, Kyoto
Kyoto, Japan, 20-24 July 2009
Contact: Prof. R. Koga, Dept. of Communication Network Engineering, Okayama University, Tsushima, Okayama, 700-8530, Japan, Fax +81 86-251-8136, E-mail: emc09@is.takushoku-u.ac.jp, Web: http://www.ieice.org/emc09/contacts.html

August 2009

14th International EISCAT Workshop
Tromsø, Norway, 3 - 7 August 2009
cf. Announcement in the Radio Science Bulletin of March 2009, p. 65.
Contact : Web : http://uit.no/fysikk/eiscat2009ws/

September 2009

Metamaterials 2009
London, UK, 1-4 September 2009
Contact: Dr. Richard W. Ziolkowski, E-mail: ziolkowski@ece.arizona.edu, Web: http://congress2009.metamorphose-vi.org/

ICEAA'09 - International Conference on Electromagnetics in Advanced Applications
Turin, Italy, 14-18 September 2009
Contact: ICEAA 07, Politecnico di Torino , Corso Duca degli Abruzzi 24 , 10129 Torino, Italy, Fax: +39-011-564-5199, e-mail: gspinasanta@corep.it, Web: http://www.iceaa.net/

October 2009

International Conference on Radar
Bordeaux, France, 12-16 October 2009
Contact: SEE / CONGRESS DEPARTMENT, Béatrice Valdayron - Valérie Alidor - Caroline Zago - Morgane Melou, Fax: + 33 (0)1 56 90 37 08, E-mail : radar2009@see.asso.fr , Web: http://www.radar2009.org

February 2010

META '10 - Second International Conference on Metamaterials, Photonic Crystals and Plasmonics
Cairo, Egypt, 22-25 February 2010
cf. Announcement in the Radio Science Bulletin of March 2009, p. 65.
Contact: Dr. Said Zouhdi, Laboratoire de Génie Electrique de paris, LGEP-Supélec, Plateau de Moulon, 91192 Gif-sur-Yvette Cedex, France, Fax+33 1 69 418318, E-mail: said.zouhdi@supelec.fr, Web: http://meta10.lgep.supelec.fr

March 2010

8th International Nonlinear Waves Workshop
La Jolla, CA, USA, 1-5 March 2010
Contact: William E. Amatucci, Plasma Physics Division, Code 6755, Naval Research Laboratory, Washington, DC 20375, USA, Fax : 202-767-3553, E-mail : bill.amatucci@nrl.navy.mil

April 2010

AP-EMC 2010 - Asia-Pacific EMC Symposium
Beijing, China, 12-16 April 2010
Contact: Web: http://www.apemc2010.org

June 2010

CROWNCOM - 5th Int. Conference on Cognitive Radio Oriented Wireless Networks and Communications
Cannes, France, 16-18 June 2010
Contact : Jacques Palicot, SUPELEC, Avenue de la Bulaie, 53576 Cesson-Sévigné, France, Fax +33 299-844599, E-mail: jacques.palicot at supelec.fr

July 2010

STP-12 SCOSTEP symposium
Berlin, Germany, 10-16 July 2010
Web: http://www.iap-kborn.de/SCOSTEP2010/ - SCOSTEP= Scientific Committee on Solar-Terrestrial Physics

COSPAR 2010 - 38th Scientific Assembly of the Committee on Space Research (COSPAR) and Associated Events
Bremen, Germany, 18 - 25 July 2010
cf. Announcement in the Radio Science Bulletin of December 2008, p. 73.
Contact: COSPAR Secretariat, c/o CNES, 2 place Maurice Quentin, 75039 Paris Cedex 01, France, Fax: +33 1 44 76 74 37, E-mail: cospar@cosparhq.cnes.fr, Web: http://www.cospar2010.org/ or http://www.cospar-assembly.org

August 2010

EMTS 2010 - International Symposium on Electromagnetic Theory (Commission B Open Symposium)
Berlin, Germany, 16-19 August 2010
Contact: EMTS 2010, Prof. Karl J. Langenberg, Universität Kassel, D-34109 Kassel, Germany, E-mail: info@emts2010.de , Web: http://www.emts2010.de

3rd International Communications in Underground and Confined Areas
Val d'Or, Québec, Canada, 23-25 August 2010
Contact: Paule Authier, Secrétaire, LRTCS-UQAT, Laboratoire de recherche Télébec en communications souterraines de l'UQAT, 450, 3e Avenue, local 103, Val-d'Or,Québec J9P 1S2, Fax: (1)(819) 874-7166, E-mail: lrcs @uqat.ca, Web: http://www.icwcuca.ca/welcome.asp

September 2010

AP-RASC - 2010 Asia-Pacific Radio Science Conference
Toyama, Japan, 22-25 September 2010
Contact: Prof. K. Kobayashi, Vice President for International Affairs, Chuo University, 1-13-27 Kasuga, Bunkyo-ku, Tokyo 112-8551, JAPAN, Fax: +81-3-3817-1847, E-mail: kazuya@tamacc.chuo-u.ac.jp

An up-to-date version of this Conference Calendar, with links to various conference web sites can be found at www.ursi.org/Calendar of supported meetings

News from the URSI Community

NEWS FROM A MEMBER COMMITTEE

FRANCE
Médaille du CNFRS

La Médaille du Comité National Français de Radioélectricité Scientifique (CNFRS) section française de l'Union Radio Scientifique Internationale (URSI) a été décernée le 24 mars 2009 à Daniel Maystre.

URSI-France souhaite ainsi souligner l'importance des contributions de Daniel Maystre au développement des connaissances en électromagnétisme et en optique et comme animateur des communautés scientifiques de ces domaines. Ainsi, ces travaux sur les réseaux de diffraction et la diffraction inverse dans le domaine de l'optique, l'ont conduit à élaborer une théorie rigoureuse de la diffraction par les surfaces aléatoires. Dernièrement ceux-ci ont porté sur les métamatériaux. Par ailleurs, il crée en 2002 le GDR Ondes, lieu d'animation de la communauté scientifique investie dans le domaine des ondes électromagnétiques, optiques et acoustiques.

La Médaille du CNFRS/URSI est « destinée à honorer des personnes qui ont œuvré pour le renom de la Science en Radioélectricité et/ou participé d'une manière très significative à la vie et au renom du CNFRS/URSI ».

Né en 1945, D. Maystre a obtenu une agrégation de Physique en 1968, à l'issue de quatre années d'études à l'ENS de St Cloud. Entré au CNRS, il soutient en 1974 une thèse d'Etat sur la théorie des réseaux de diffraction, qui est traduite en anglais par la NASA l'année suivante. Il dirige de 1988 à 2000 le Laboratoire d'Optique Electromagnétique de l'Université d'Aix-Marseille III puis, à l'issue d'une mission que lui confient le CNRS et l'Enseignement Supérieur, il fait créer en janvier 2000 l'Institut Fresnel, Unité Mixte de Recherche 6133. Le CNRS crée aussi en 2002 sur sa demande le GDR Ondes dont il prend la direction pendant quatre années.

Dans un premier temps, D. Maystre s'est quasi-exclusivement consacré à l'étude théorique et numérique des réseaux de diffraction. La découverte d'une équation intégrale originale lui a permis d'élaborer le premier code numérique capable de calculer précisément les propriétés des réseaux dans le visible, l'infrarouge et l'ultraviolet. Perfectionné au cours du temps, ce code est utilisé aujourd'hui par une vingtaine de centres industriels et de laboratoires universitaires dans le monde. Il a permis au début des années 70 d'explorer les propriétés des premiers réseaux holographiques et d'optimiser les propriétés des premiers réseaux embarqués sur satellite dans le cadre de la naissante Optique spatiale.

Daniel Maystre a développé la première théorie phénoménologique quantitative des "anomalies de Wood" des réseaux de diffraction, basée sur les propriétés des plasmons de surface. Il a ainsi découvert puis vérifié expérimentalement le phénomène d'absorption totale d'une onde incidente par un réseau métallique. Le groupe de D. Maystre a par la suite modélisé les cristaux photoniques et les fibres optiques à cristaux photoniques. Il a été parmi les premiers à introduire la diffraction inverse dans le domaine de l'optique et de l'électromagnétisme et à élaborer une théorie rigoureuse de la diffraction par des surfaces rugueuses aléatoires.

Enfin, plus récemment, D. Maystre s'est intéressé aux métamatériaux. Il a pu démontrer mathématiquement qu'un matériau main gauche homogène de perméabilité et permittivité simultanément négatives ne pouvait exister mais que néanmoins, la notion de « superlentille » n'était pas une vue de l'esprit.

D. Maystre a reçu en 1975 le prix Fabry de Gramont attribué par le Comité Français d'Optique. Il a obtenu le Prix Scientifique Philip Morris en 1998. En 1980 – 81, il a effectué un séjour d'une année au National Bureau of Standards (Washington DC) financé par la "National Science Foundation". Il a dirigé totalement ou en grande partie une vingtaine de thèses. Il est signataire de 20 ouvrages ou chapitres d'ouvrage, plus de 150 articles dans des revues internationales avec comité de lecture, 60 actes référencés de conférences, 63 conférences invitées, quatre brevets. Il a été responsable ou co-responsable d'une trentaine de contrats de collaboration avec des industriels et grands organismes de recherche. Il est « Fellow » de l'Electromagnetics Academy (Cambridge, USA).

D. Maystre est aujourd'hui, au sein de l'Institut Fresnel, Directeur de Recherche en classe exceptionnelle au CNRS.

BOOK PUBLISHED BY URSI RADIOSCIENTISTS

Advances in Electromagnetic Fields in Living Systems: Volume 5, Health Effects of Cell Phone Radiation

by James C. Lin (Ed.), Springer Publishing, 2009, 279 pp., hardcover, ISBN: 978-0-387-92733-6.

About this Book

The popularity and rapid deployment of wireless communication technology has led to increasing numbers of new devices and systems that emit RF electromagnetic energy. It has resulted in large numbers of individuals at the workplace or in the general public being exposed to RF fields. At the current rate of growth, more of the world's population will have access to mobile phone services than to electricity. In most cases, the RF sources are in close proximity to the human body. The increased exposures at the workplace or in daily life have prompted the need for further research to evaluate RF safety and health implications.

However, exposure to RF electromagnetic fields is not limited to mobile or wireless communication: widespread applications of RF and microwave energy are found in RF article identification and surveillance, on-body sensing and interrogation, novel active and passive security and detection technology, and proposed digital living network applications. Given the technological, regulatory, and marketing challenges, the timing of the introduction or deployment of many new applications is somewhat uncertain. It should be noted that the experience of the cellular mobile telephone industry indicates that once new technology is deployed, the adoption rate can easily explode.

There is a real need for reliable scientific answers on health effects associated with exposures resulting from widespread use of RF electromagnetic fields in new and existing technology and devices. The current state of scientific knowledge is presented in seven chapters by scientists who have made major contributions to this area of research.

This book is written for scientists and researchers in biophysics, bioengineering, biology, medicine, radio sciences, physics, and electrical and computer engineering. The seven chapters in this book include:

- Cellular Biology Aspects
- Carcinogenic Potential
- Epidemiological Studies
- Cognitive Effects
- Hypersensitivity
- Occupational Exposure
- Dosimetry and Induced Temperature

About the Editor

James C. Lin, PhD, is Professor of electrical engineering, bioengineering, physiology, and biophysics at the University of Illinois, Chicago, and was Head of the Bioengineering Department. He is a Fellow of the AAAS, AIMBE and the IEEE, and a recipient of the d'Arsonval Medal from the Bioelectromagnetics Society. Dr. Lin is a member of the International Commission on Non-Ionizing Radiation (ICNIRP). He served as Chair of URSI Commission K on Electromagnetics in Biology and Medicine, IEEE Committee on Man and Radiation, and Vice President of the National Council on Radiation Protection and Measurements (NCRP).

Wave Refraction in Linear Media with Time Dispersion

by Vladimir V. Kopeikin, Moscow, Nauka, 2009, 128 pp., hardcover, ISBN 978-5-02-036962-7.

About this Book

The monograph proposes a new method for deriving spatial-temporal geometrical-optic equations, based on more general equations of wave-energy transfer in the space than the equations used in a standard method. A new approach makes it possible to pass from a locally plane homogeneous monochromatic field model – which is an exact solution to the wave equation for a homogeneous medium and forms the basis for the standard version of geometric optics – to a smoothly inhomogeneous model in the form of the Airy function, which is an exact solution of the wave equation for the problem of refraction in a linear layer. The obtained approximation describes the effect of dispersion refraction and corrects the description of usual refraction for unmodulated monochromatic waves in linear media with time dispersion.

This monograph can be used by specialists in the field of wave processes, by radiophysics studying radio propagation in the ionosphere, and by students and post-graduates of the corresponding specialties.

Table of Contents

[The above items were taken from material supplied by the publishers.]

Information for authors

Content

The *Radio Science Bulletin* is published four times per year by the Radio Science Press on behalf of URSI, the International Union of Radio Science. The content of the *Bulletin* falls into three categories: peer-reviewed scientific papers, correspondence items (short technical notes, letters to the editor, reports on meetings, and reviews), and general and administrative information issued by the URSI Secretariat. Scientific papers may be invited (such as papers in the *Reviews of Radio Science* series, from the Commissions of URSI) or contributed. Papers may include original contributions, but should preferably also be of a sufficiently tutorial or review nature to be of interest to a wide range of radio scientists. The *Radio Science Bulletin* is indexed and abstracted by INSPEC.

Scientific papers are subjected to peer review. The content should be original and should not duplicate information or material that has been previously published (if use is made of previously published material, this must be identified to the Editor at the time of submission). Submission of a manuscript constitutes an implicit statement by the author(s) that it has not been submitted, accepted for publication, published, or copyrighted elsewhere, unless stated differently by the author(s) at time of submission. Accepted material will not be returned unless requested by the author(s) at time of submission.

Submissions

Material submitted for publication in the scientific section of the *Bulletin* should be addressed to the Editor, whereas administrative material is handled directly with the Secretariat. Submission in electronic format according to the instructions below is preferred. There are typically no page charges for contributions following the guidelines. No free reprints are provided.

Style and Format

There are no set limits on the length of papers, but they typically range from three to 15 published pages including figures. The official languages of URSI are French and English: contributions in either language are acceptable. No specific style for the manuscript is required as the final layout of the material is done by the URSI Secretariat. Manuscripts should generally be prepared in one column for printing on one side of the paper, with as little use of automatic formatting features of word processors as possible. A complete style guide for the *Reviews of Radio Science* can be downloaded from http://www.ips.gov.au/IPSHosted/NCRS/reviews/. The style instructions in this can be followed for all other *Bulletin* contributions, as well. The name, affiliation, address, telephone and fax numbers, and e-mail address for all authors must be included with all submissions.

All papers accepted for publication are subject to editing to provide uniformity of style and clarity of language. The publication schedule does not usually permit providing galleys to the author.

Figure captions should be on a separate page in proper style; see the above guide or any issue for examples. All lettering on figures must be of sufficient size to be at least 9 pt in size after reduction to column width. Each illustration should be identified on the back or at the bottom of the sheet with the figure number and name of author(s). If possible, the figures should also be provided in electronic format. TIF is preferred, although other formats are possible as well: please contact the Editor. Electronic versions of figures *must* be of sufficient resolution to permit good quality in print. As a rough guideline, when sized to column width, line art should have a minimum resolution of 300 dpi; color photographs should have a minimum resolution of 150 dpi with a color depth of 24 bits. 72 dpi images intended for the Web are generally *not* acceptable. Contact the Editor for further information.

Electronic Submission

A version of Microsoft *Word* is the preferred format for submissions. Submissions in versions of T_EX can be accepted in some circumstances: please contact the Editor before submitting. *A paper copy of all electronic submissions must be mailed to the Editor, including originals of all figures.* Please do *not* include figures in the same file as the text of a contribution. Electronic files can be send to the Editor in three ways: (1) By sending a floppy diskette or CD-R; (2) By attachment to an e-mail message to the Editor (the maximum size for attachments *after* MIME encoding is about 7 MB); (3) By e-mailing the Editor instructions for downloading the material from an ftp site.

Review Process

The review process usually requires about three months. Authors may be asked to modify the manuscript if it is not accepted in its original form. The elapsed time between receipt of a manuscript and publication is usually less than twelve months.

Copyright

Submission of a contribution to the *Radio Science Bulletin* will be interpreted as assignment and release of copyright and any and all other rights to the Radio Science Press, acting as agent and trustee for URSI. Submission for publication implicitly indicates the author(s) agreement with such assignment, and certification that publication will not violate any other copyrights or other rights associated with the submitted material.

APPLICATION FOR AN URSI RADIOSCIENTIST

I have not attended the last URSI General Assembly, and I wish to remain/become an URSI Radioscientist in the 2009-2011 triennium. Subscription to *The Radio Science Bulletin* is included in the fee.

(please type or print in BLOCK LETTERS)

Name : Prof./Dr./Mr./Mrs./Ms._____

Family Name First Name Middle Initials

Present job title: _____

Years of professional experience:_____

Professional affiliation:_____

I request that all information be sent to my ☐ home ☐ business address, i.e.:

Company name: _____

Department: _____

Street address: _____

City and postal/zip code: _____

Province/State: _____ Country:_____

Phone: _____ext. _____ Fax: _____

E-mail: _____

Areas of interest (Please tick)

☐ A Electromagnetic Metrology
☐ B Fields and Waves
☐ C Radio-Communication Systems & Signal Processing
☐ D Electronics and Photonics
☐ E Electromagnetic Environment & Interference
☐ F Wave Propagation & Remote Sensing
☐ G Ionospheric Radio and Propagation
☐ H Waves in Plasmas
☐ J Radio Astronomy
☐ K Electromagnetics in Biology & Medicine

I prefer (Please tick)

☐ An electronic version of the RSB downloadable from the URSI web site
(The URSI Board of Officers will consider waiving the fee if a case is made to them in writing.) 40 Euro

☐ A hard copy of the RSB sent to the above address 100 Euro

Method of payment : VISA / MASTERCARD (we do not accept cheques)

Credit card No ☐☐☐☐ ☐☐☐☐ ☐☐☐☐ ☐☐☐☐ Exp. date _____

CVC Code: _____Date :_____Signed _____

Please return this signed form to :

The URSI Secretariat
c/o Ghent University / INTEC
Sint-Pietersnieuwstraat 41
B-9000 GHENT, BELGIUM
fax (32) 9-264.42.88